Searches for SUSY and HCal performance studies with CMS Run 2 data

By

Tribeni Mishra

Enrollment No : PHYS11201704026

National Institute of Science Education and Research, Bhubaneswar

A thesis submitted to the

Board of Studies in Physical Sciences

In partial fulfillment of requirements

for the Degree of

DOCTOR OF PHILOSOPHY

of

HOMI BHABHA NATIONAL INSTITUTE

October, 2023

Homi Bhaba National Institute

Recommendations of the Viva Voce Committee

As members of the Viva Voce Committee, we certify that we have read the dissertation prepared by **Tribeni Mishra** entitled **Searches for SUSY and HCal performance studies with CMS Run 2 data** and recommend that it may be accepted as fulfilling the thesis requirement for the award of Degree of Doctor of Philosophy.

Prof. Bedangadas Mohanty	22/03/2024
Prof. Sanjay Kumar Swain	22/03/2024
Prof. Basanta Kumar Nandi	22/03/2024
Prof. Prolay Kumar Mal	March 22, 2024
Prof. Subhasish Basak	22/3/24
Prof. Seema Sharma	25-03-2024

Final approval and acceptance of this thesis is contingent upon the candidate's submission of the final copies of the thesis to HBNI.
I/We hereby certify that I/we have read this thesis prepared under my/our direction and recommend that it may be accepted as fulfilling the thesis requirement.

Date : 22nd March 2024

Place : NISER Bhubaneswar

Signature

Guide : Prof. Sanjay Kumar Swain

STATEMENT BY AUTHOR

This dissertation has been submitted in partial fulfillment of requirements for an advanced degree at Homi Bhabha National Institute (HBNI) and is deposited in the Library to be made available to borrowers under rules of the HBNI.

Brief quotations from this dissertation are allowable without special permission, provided that accurate acknowledgement of source is made. Requests for permission for extended quotation from or reproduction of this manuscript in whole or in part may be granted by the Competent Authority of HBNI when in his or her judgment the proposed use of the material is in the interests of scholarship. In all other instances, however, permission must be obtained from the author.

Tribeni Mishra

Tribeni Mishra

DECLARATION

I hereby declare that I am the sole author of this thesis in partial fulfillment of the requirements for a postgraduate degree from National Institute of Science Education and Research (NISER). I authorize NISER to lend this thesis to other institutions or individuals for the purpose of scholarly research.

Tribeni Mishra

Tribeni Mishra

List of Publications arising from the thesis

Journal

1. CMS Collaboration, "Search for supersymmetry in proton-proton collisions at 13 TeV in final states with jets and missing transverse momentum",
   doi: 10.1007/JHEP10(2019)244, **arXiv:** 1908.04722

2. CMS Collaboration, "Performance of the local reconstruction algorithms for the CMS hadron calorimeter with Run 2 data",
   doi: 10.1088/1748-0221/18/11/P11017, **arXiv:** 2306.10355

Chapters in books and lectures notes

1. Proceedings of the XXIV DAE-BRNS High Energy Physics Symposium, Jatni, India "Search for Supersymmetry with Jets and Missing Transverse Momentum Final States",
   doi: 10.1007/978-981-19-2354-8_51

2. Proceedings of Science, "SUSY searches in hadronic final states at CMS",
   doi: 10.22323/1.422.0268

3. Proceedings of Science, "Performance of the CMS HCAL local reconstruction algorithms in Run2",
   doi: 10.22323/1.449.0582

4. Proceedings of Science, "SUSY searches in photonic final states with CMS",
   doi: 10.22323/1.449.0454

Conferences

1. XXIV DAE-BRNS High Energy Physics Symposium 2020, NISER, Jatni,
   Talk title: "Search for Supersymmetry with Jets and Missing Transverse Momentum Final States"

2. NUCLEUS – 2021, Petersburg, Russia, **Talk title:** "CMS SUSY and Exotica results"

3. LHCP 2022, **Poster title:** "SUSY searches in hadronic final states at CMS"

4. XXV DAE-BRNS High Energy Physics Symposium 2022, IISER Mohali,
   Talk title: "Search for SUSY in events with a photon, a lepton, and missing transverse energy using full Run2 dataset at 13 TeV"

5. ICNFP 2022, Kolymbari, Greece, **Talk title:** "SUSY (CMS)"

6. EPS-HEP Conference 2023, Hamburg, Germany,
   Talk title: "SUSY searches in photonic final states with CMS"

7. EPS-HEP Conference 2023, Hamburg, Germany, **Poster title:** "Performance of the CMS HCAL local reconstruction algorithms with Run 2 data"

Tribeni Mishra
Tribeni Mishra

DEDICATIONS

I dedicate this thesis to my beloved parents and sisters, whose unwavering support and endless encouragement have been my driving force throughout this academic endeavor. Your belief in my abilities, your sacrifices, and your unconditional love has shaped my journey and made this accomplishment possible. This dedication is a small token of my immense gratitude for your constant presence, guidance, and unwavering faith in my potential. With heartfelt appreciation, I honor you in this thesis, acknowledging the immeasurable impact you have had on my academic growth.

Tribeni Mishra

TRIBENI MISHRA

ACKNOWLEDGEMENTS

With profound gratitude and heartfelt appreciation, I extend my sincere acknowledgments to those who have made this thesis possible. First and foremost, I am deeply thankful to my esteemed supervisor, Prof. Sanjay Kumar Swain, whose guidance and wisdom have been invaluable. His constant support and encouragement propelled me through the challenges of this research journey, and I am sincerely grateful for that. His encouraging words during the toughest moments of this journey have been like a guiding light.

I wish to extend my heartfelt gratitude to the esteemed members of my doctoral committee: Prof. Bedangadas Mohanty, Prof. Prolay Kumar Mal, Prof. Seema Sharma, and Prof. Subhasis Basak, for their invaluable guidance and rigorous evaluation, which has been instrumental in shaping this work. I am profoundly appreciative of their constructive feedback. Their valuable input has played a pivotal role in refining and enhancing the quality of my research. My heartfelt thanks go to the CMS collaboration and the collaborative members with whom I had the privilege to work, including Prof. William Ford, Prof. Andrew James Whitebeck, Prof. Kenichi Hatakeyama, Prof. Jaehyeok Yoo, Dr. Luca Schodellaro, Dr. Kevin Pedro, and Dr. Hui Wang. Their guidance and expertise were invaluable, contributing significantly to the depth of my work.

I extend my gratitude to my supportive and inspiring labmates, including Aloke, Prafulla, Chandi, Lipsa, Priyanka, Koushik, Kuldeep, Amit, Sneh Shuchi, Rahul, and others, whose camaraderie and collaborative spirit contributed immensely to the creation of a stimulating academic environment, making this journey truly enjoyable. In addition, my deepest gratitude goes to my family members, whose unwavering support and understanding sustained me during this challenging endeavor. Their love and encouragement were my driving force, and I am truly thankful for their presence in my life. Lastly, I acknowledge my dear friend Supratikshya, whose unwavering mental support and encouragement were a constant source of strength. Her friendship provided solace during the toughest moments of this journey, and for that, I am profoundly grateful.

Each of you has played a significant role in this accomplishment, and your contributions are deeply appreciated. Thank you for being a part of this important chapter in my academic and personal growth.

Tribeni Mishra

TRIBENI MISHRA

ABSTRACT

The standard model (SM) has successfully explained atomic and subatomic phenomena, encompassing fermions (leptons and quarks) and their interactions through electromagnetic, weak, and strong forces. However, it lacks an explanation for the three generations of quarks and leptons, their varying masses, the nature of dark matter, and the fine-tuning of the mass of the Higgs boson. Supersymmetry (SUSY) addresses these issues by introducing superpartners for SM particles. These include scalar squarks, sleptons, gluinos, higgsinos, neutralinos, and charginos. A search for the production of gluinos and squarks is performed, using proton-proton collision data collected by the compact muon solenoid (CMS) detector during Run 2 (2015-2018). It involves multiple jets and large missing transverse momentum in the final state. No significant excess in the event yield is observed relative to the expected background contributions from SM processes.

Assuming the lightest supersymmetric particle to be a neutralino, the study establishes exclusion limits for pair-produced gluino models in the range of 2000-2300 GeV, and for pair-produced squarks in the range of 1190-1630 GeV.

Additionally, a search is ongoing to explore the signature of the SUSY signal within the framework of general gauge mediation, where proton-proton collisions produced a neutralino-chargino pair. This results in a final state characterized by a photon, a lepton (e or μ), and substantial missing transverse momentum.

The CMS detector features a superconducting solenoid generating a 3.8 T magnetic field and includes a silicon tracker, electromagnetic calorimeter (ECAL), hadron calorimeter (HCAL), and gas-ionization detectors for muon detection. Particle momenta and energies are measured using these subdetectors. During Run 2, algorithms (M2, M3, and MAHI) were developed to reconstruct energy in the CMS HCAL, considering the overlapping signals from adjacent bunch crossings. The performance of these algorithms is compared. The consistency between online and offline reconstructions is examined, focusing on the M2+M3 and MAHI algorithms for HCAL reconstruction. The HCAL pulse shape fluctuations (pedestal) are also studied for the hadronic barrel and hadronic endcap detectors.

Tribeni Mishra

TRIBENI MISHRA

Contents

References 153

Summary

This thesis presents three comprehensive analyses using proton-proton collision data at 13 TeV energy, comprising 137 fb^{-1} integrated luminosity collected by the CMS experiment from 2016 to 2018.

Two studies focus on exploring Supersymmetry (SUSY) signatures. The first analysis delves into the production of colored SUSY particles, like gluinos and squarks, decaying into jets, and significant missing transverse momentum (p_T^{miss}). Despite extensive efforts, no conclusive evidence supporting SUSY production was found. Upper limits on the production cross-section were established, contributing to ongoing CMS efforts to address SM uncertainties. Gluinos with masses between 2000 to 2310 GeV were excluded at a 95% confidence level, extending previous mass limits. Similar investigations on squarks revealed exclusion limits up to 1190 GeV for top squarks and 1630 GeV for light-flavored squarks. These findings mark significant progress in our understanding of supersymmetric particles. The subsequent analysis explores SUSY models with general gauge mediation (GGM), focusing on events with a photon, at least one lepton, and substantial p_T^{miss}. This ongoing study aims to improve the agreement between observed data and predicted backgrounds, a critical step before proceeding to the signal region where significant numbers of supersymmetric signal events are anticipated. The analysis aims to either detect SUSY signatures or further constrain SUSY particle masses.

Additionally, the thesis discusses the performance of various local reconstruction algorithms employed in the CMS Hadron Calorimeter (HCAL) during Run 2. The challenges such as out-of-time pileup (OOTPU) were addressed, and a pulse-shape fitting algorithm, "Minimization at HCAL, Iteratively", emerged as the preferred method. This method suppresses OOTPU, provides excellent energy resolution, and operates swiftly in High-Level

Triggers (HLT).

In summary, while the analyses did not yield definitive evidence for SUSY production, the established upper limits on production cross-sections and the advancements in experimental techniques, especially in dealing with challenges like OOTPU, mark significant progress. These findings emphasize the importance of continuous efforts and advancements in the field, especially in the context of upcoming phases such as Run 3 and the High-Luminosity LHC, which hold promising opportunities for further exploration of physics beyond the SM.

List of Figures

List of Tables

Chapter 1

SM of particle physics and beyond

Understanding the basic nature of the universe has been a fundamental human quest since the beginning of human awareness. The foundation of particle physics lies in the Standard Model (SM) [17, 18, 19, 20], representing our current knowledge about fundamental particles and their interactions. This comprehensive framework unites the theories of strong interaction [21] with the unified theory of electromagnetic and weak interactions [22], encompassing nearly all fundamental forces, except gravity. Section 1.1 provides a concise overview of the SM, delving into its particle constituents, their interactions, and the intricate mathematical framework underpinning the model.

Many experiments, including the Large Hadron Collider (LHC) [23, 24], have confirmed the predictions of SM through careful measurements. Despite its remarkable success, the SM fails to address several pivotal questions. Certain queries arise from theoretical foundations, whereas others emerge from experimental observations in astronomy and high-energy particle physics, appearing to challenge the predictions made by the SM. Section 1.2 briefly outlines these unresolved questions, serving as the driving force behind the analyses presented in this thesis and the thesis itself.

Supersymmetry [3, 25, 26, 27], commonly referred to as SUSY, emerges as a compelling extension to the SM, offering potential solutions to the shortcomings. Section 1.3 provides a comprehensive overview of SUSY, coupled with a concise theoretical discourse pertinent to each of the SUSY searches detailed in this thesis. Further intricacies of the theoretical foundations underlying the SUSY analyses presented herein can be found in the respective Chapters outlining these analyses (Chapters 3 and 4).

1.1 SM of particle physics

The Standard Model [17] of particle physics stands as one of the most successful scientific theories in history. It serves as a mathematical framework that encompasses all known fundamental particles and elucidates their interactions. According to the SM, the universe's entire material composition is constituted of various elementary particles, categorized as fermions (particles with half-integral spin) and bosons (particles with integral spin). Over the years, diverse experiments conducted worldwide have confirmed the existence of these particles. Notably, the Higgs boson, the final missing component of the SM, was observed in 2012 [28][29] by the CMS and ATLAS experiments at the LHC, nearly six decades after its theoretical prediction.

1.1.1 Particle spectrum and interactions of the SM

Particles in the SM are categorized based on their spin properties. Fermions, the building blocks of matter, have a spin of 1/2, whereas bosons, responsible for fundamental forces [30], have a spin of 1. These particles are also characterized by their masses and various quantum numbers, including electric charge, color charge, and hypercharge, as well as lepton and baryon numbers.

Every particle in the SM has a corresponding antiparticle, sharing the same mass and spin but possessing opposite electric charge, lepton number, and baryon number. Fermions in the SM are divided into two groups: quarks and leptons. Both quarks and leptons are organized into three generations, each generation containing particles of increasing mass.

Leptons consist of six spin 1/2 fermions that are capable of undergoing weak interactions and have corresponding antimatter partners. The first three leptons are the electron (e), muon (μ), and tau (τ), each carrying the same electromagnetic charge as the electron but differing in mass. Each lepton has an associated neutrino, an electrically neutral particle that

only interacts via the weak force and is notoriously difficult to detect due to its minimal interaction with matter. Neutrinos are the lightest fermions in the SM and their masses, although small, have yet to be precisely measured. These elusive particles are still under intense scientific scrutiny.

In each lepton generation, there are a pair of charged particles and their corresponding neutrinos. The first generation comprises the electron and its neutrino (ν_e), the second generation has the muon and its neutrino (ν_μ), and the third generation contains the tau and its neutrino (ν_τ). Experimental evidence has confirmed that the difference in lepton and anti-lepton numbers in a fundamental interaction remains constant across all three generations, leading to the concept of three conserved lepton numbers (L_e, L_μ, and L_τ).

In most particle interactions, lepton numbers are conserved, but in the case of neutrino oscillations, they are violated due to the mixing of flavor eigenstates to form mass states. Neutrino oscillations have been observed in numerous experiments [31][32][33], indicating that neutrinos possess extremely small but non-zero masses.

Quarks are a group of six spin-1/2 fermionic particles, each with a corresponding anti-particle, and are organized similarly to leptons. Each generation of quarks comprises a pair of particles carrying electric charges of $+\frac{2}{3}$ and $-\frac{1}{3}$ respectively. The up (u) and down (d) quarks belong to the first generation, while the charm (c) and strange (s) quarks are part of the second generation. The third generation includes the top (t) and bottom (b) quarks, with the top quark being the most massive particle in the SM, with a mass of approximately 172.8 GeV.

In addition to the strong force, quarks also experience the electroweak (EW) force. They possess a color charge, coming in six distinct values (red, green, blue, and their corresponding anti-colors), which is a fundamental aspect of the strong force. Quarks cannot exist in isolation due to the nature of the strong force; instead, they combine to form composite particles known as hadrons. Examples of hadrons include protons and neutrons. However,

the top quark is an exception as it decays rapidly before composite states can form.

The up and down quarks specifically bind together to create protons and neutrons, which, in turn, form the nuclei of atoms. These nuclei then combine with electrons to form the atoms and molecules that constitute ordinary matter, making quarks from the first-generation integral components of what is often referred to as "everyday matter".

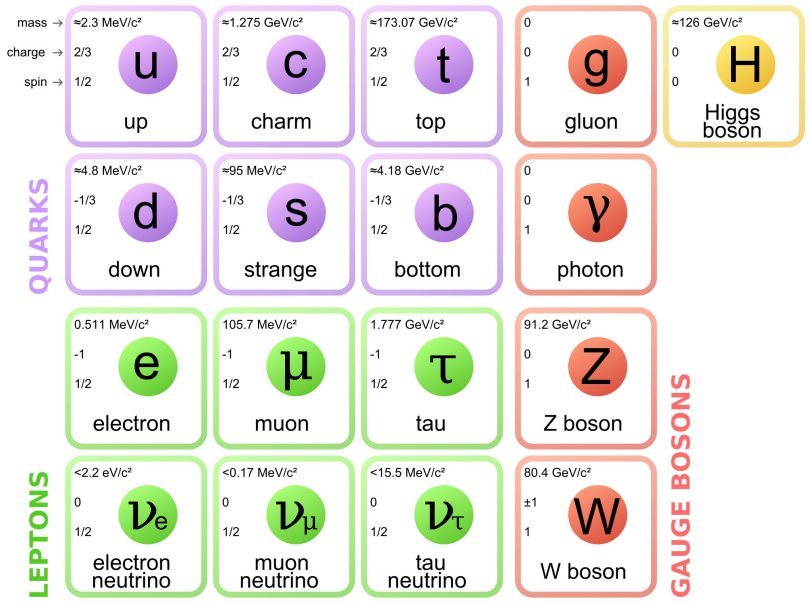

Figure 1.1: Elements of the SM: The diagram displays twelve fermions (quarks and leptons) with a spin of $\frac{1}{2}$ and bosons including gluons, W/Z bosons, and a photon with a spin of 1 and the Higgs boson with a spin of zero. The SM does not incorporate gravitational interactions and the associated force carrier, the graviton [1].

Below an energy scale of approximately 246 GeV, known as the electroweak scale, the interactions within the SM can be categorized into electromagnetic, weak, and strong interactions. These interactions are mediated by gauge bosons, which are particles with integer spin following the principles of Bose-Einstein statistics.

Electromagnetic interactions are facilitated by the photon (γ), a massless [34] particle that consequently possesses an extensive interaction range. These interactions are governed by the $\mathrm{U}(1)_\mathrm{Y}$ symmetry [35, 36, 37, 38] of Quantum Electrodynamics (QED). The associ-

ated conserved charge for this gauge symmetry is the electric charge. Notably, the neutral photon does not exhibit self-interactions but does interact with quarks and charged leptons through the electromagnetic force.

Weak interactions are mediated by the massive Z and $W^{\pm}$ bosons. The symmetry group $\mathrm{SU(2)_L}$ [39, 40] operates specifically on left-handed particles, transforming isospin states and forming weak isospin doublets for up-type quarks (u, c, t) and down-type quarks (d, s, b). Because of its coupling to left-handed particles only, weak interactions violate both parity and charge-parity. The $W^{\pm}$ and Z bosons interact with both quarks and leptons through the weak nuclear force.

Strong interactions [21] are facilitated by eight massless gluons (g), described by Quantum Chromodynamics (QCD). These gluons are the gauge bosons of the $\mathrm{SU(3)_C}$ symmetry group, featuring conserved color charge. Gluons interact with quarks through the strong nuclear force. A noteworthy characteristic of gluons is their self-interaction, leading to fascinating phenomenological consequences. Specifically, the coupling constant increases at low energies, approaching one. Consequently, quarks and gluons are confined; quarks form bound states through strong interactions and have not been observed in a free state. At high energies, quarks become asymptotically free due to the decrease in the coupling constant, allowing perturbation theory to predict QCD interactions.

General relativity predicts the existence of a spin-2 particle called the graviton, $\widetilde{\mathrm{G}}$, which mediates gravitational interactions. Despite its theoretical prediction, the graviton has not been discovered and is not part of the SM. The SM does not incorporate gravity, and theories that attempt to include gravity, like Gauge-Mediated SUSY Breaking, are explored in Section 1.3.3.

The Higgs (H) boson, the most recent addition to the SM, is a scalar particle with spin-zero. It was theorized by Peter Higgs in 1964 and was observed at the LHC in 2012. Through a mechanism called spontaneous symmetry breaking (SSB), the Higgs boson im-

parts mass to the weak bosons ($W^{\pm}$ and Z), quarks, and leptons. This mechanism is further discussed in Section 1.1.2 and is based on Reference [41]. Figure 1.1 summarizes all SM particles, including their charge, spin, and mass.

1.1.2 Mathematical structure of the SM

The SM is a Quantum Field Theory (QFT) [42], a branch of theoretical physics that integrates quantum mechanics [42] and special relativity. Within QFT, the fundamental components are quantum fields that fill the entirety of space, and particles emerge as quantized manifestations of these fields. Different types of particles, possessing spins of 0, 1/2, and 1, are described using distinct fields. For instance, the Higgs boson is linked to a complex scalar field denoted as ϕ, having a spin of 0. Spinors, represented as ψ, are utilized to depict fermion fields with a spin of 1/2, while vector fields denoted as A are employed for particles with a spin of 1. The vector fields include eight gluon fields (g) affiliated with the $\mathrm{SU(3)_C}$ group, two charged fields ($W^{1,2}$), and one neutral field (W^3) associated with the $\mathrm{SU(2)_I}$ group [39, 40]. Moreover, a hypercharge boson field (B) associated with the $\mathrm{U(1)_Y}$ group is present, conserving properties such as color charge (C), weak isospin (I), and hypercharge (Y). During electroweak symmetry breaking, these fields interact, leading to the formation of $W^{\pm}$, Z boson, and photon (γ) through the mixing of $W^a = (W^1, W^2, W^3)$ and B bosons.

The mathematical representation of the SM is formulated through the Lagrangian approach [42] applied to particle fields. The Lagrangian dictates the dynamics of the theory, relying on symmetries—specific transformations preserving the invariance of the system. In the SM, the Lagrangian remains unchanged under local symmetries associated with the $SU(3)_C \times SU(2)_I \times U(1)_Y$ group. $SU(2)_I$ is often denoted as $SU(2)_L$ because of the chirality of the weak interaction.

QED is a local gauge theory utilized to describe electromagnetic interactions, depict-

ing the exchange of photons between electrically charged particles. In particle physics, a fermion with mass M is represented by a four-component spinor denoted as ψ in the fermion field. This description is expressed through the Lagrangian equation governing the Dirac equation:

$$\mathcal{L} = \bar{\psi}(i\gamma^\mu \partial_\mu - M)\psi \tag{1.1}$$

Here, γ^μ represents a set of matrices, and $\bar{\psi}$ is defined as $\bar{\psi} \equiv \psi^\dagger \gamma^0$. When undergoing a local $U(1)$ transformation, involving a phase change by an angle $a(x)$, $\psi(x)$ transforms as follows:

$$\psi(x) \to \psi'(x) = e^{iqa(x)}\psi(x) \tag{1.2}$$

Under this transformation, the Dirac Lagrangian is modified:

$$\mathcal{L} = \bar{\psi}(i\gamma^\mu \partial_\mu - M)\psi - \bar{\psi}\gamma^\mu \partial_\mu q a(x)\psi \tag{1.3}$$

To maintain invariance, the derivative is replaced by the covariant derivative D_μ:

$$D_\mu = \partial_\mu - iqA_\mu, \tag{1.4}$$

Here, A_μ is a vector field modified under local U(1) transformation as follows:

$$A_\mu \to A'_\mu = A_\mu + \partial_\mu a \tag{1.5}$$

This modification results in a modified Lagrangian:

$$\mathcal{L}_{\text{mod}} = \bar{\psi}(i\gamma^\mu D_\mu - M)\psi = \bar{\psi}(i\gamma^\mu \partial_\mu - M)\psi + q\bar{\psi}\gamma^\mu \psi A_\mu \tag{1.6}$$

the first term still represents the freely moving fermion according to the Dirac equation, while the second term accounts for the fermion's interaction with a gauge field A_μ. In QED, this field corresponds to the photon and mediates interactions between charged particles, exerting a force proportional to the electromagnetic charge.

In the realm of gauge theories, the Electroweak (EW) model [22] combines electromagnetic and weak forces, preserving the local $SU(2)_L \times U(1)_Y$ group symmetry. This model replaces the single gauge field A_μ with three $SU(2)$ gauge fields $\mathrm{W}_\mu^{1,2,3}$ and a $U(1)$ gauge field B_μ. The covariant derivative takes the form:

$$D_\mu = \partial_\mu - ig\frac{\tau_a}{2}W_\mu^a - ig'\frac{Y}{2}B_\mu, \quad a = 1,2,3 \tag{1.7}$$

Here, g and g' represent the coupling constants for the $SU(2)_L$ and $U(1)_Y$ groups, respectively. Here, τ_a and Y serve as group generators for $SU(2)_L$ and $U(1)_Y$, analogous to the concept of electric charge in the context of QED. The electroweak Lagrangian can be expressed as:

$$\mathcal{L}_{EW} = i\bar{\psi}\gamma^\mu D_\mu \psi - \frac{1}{4}W_{\mu\nu}^a W_a^{\mu\nu} - \frac{1}{4}B_{\mu\nu}B^{\mu\nu} \tag{1.8}$$

The four electroweak fields combine as follows:

$$W_\mu^\pm = \frac{1}{\sqrt{2}}(W_\mu^1 \mp iW_\mu^2)Z_\mu = \frac{gW_\mu^3 - g'B_\mu}{\sqrt{g^2+g'^2}}A_\mu = \frac{gW_\mu^3 + g'B_\mu}{\sqrt{g^2+g'^2}} \tag{1.9}$$

resulting in the W ±, Z, and γ bosons. The transition from the weak basis to the mass basis is governed by the weak mixing angle θ_W:

$$\cos\theta_W = \frac{g}{\sqrt{g^2+g'^2}}, \quad \tan\theta_W = \frac{g'}{g} \tag{1.10}$$

The production of the Z and γ bosons can be represented as:

$$\begin{pmatrix} Z_\mu \\ A_\mu \end{pmatrix} = \begin{pmatrix} \cos\theta_W & -\sin\theta_W \\ \sin\theta_W & \cos\theta_W \end{pmatrix} \begin{pmatrix} W_\mu^3 \\ B_\mu \end{pmatrix} \tag{1.11}$$

The electroweak theory displays chirality, indicating different interactions for left- and right-handed particles. This chiral asymmetry leads to parity violation in weak interactions [43], a phenomenon confirmed by experiments since 1956. Specifically, in the charged electroweak sector, the W boson avoids interactions with right-handed fermions, while the Z boson interacts with both chiralities with varying intensities.

QCD describes the strong interaction among color-charged particles (quarks and gluons) via the exchange of gluons, which carry a color charge. The QCD Lagrangian, resembling that of QED, is given with the covariant derivative as:

$$D_{\mu}^{QCD} = \partial_{\mu} - ig_s \frac{\lambda_a}{2} G_{\mu}^{a}, \quad a = 1...8 \tag{1.12}$$

Here, g_s represents the strong coupling constant, and λ_a represents the 8 generators of Gell-Mann matrices. The Lagrangian for the QCD interaction can be articulated as follows:

$$\mathcal{L}_{QCD} = \bar{\psi}(i\gamma^{\mu} D_{\mu} - m\delta_{ij})\psi - \frac{1}{4} G_{\mu\nu}^{a} G_{a}^{\mu\nu} \tag{1.13}$$

where m denotes the mass of the quark corresponding to the field ψ.

The aforementioned model describes the kinetic properties and interactions of fundamental fields. However, a significant issue with the EWK Lagrangian is the absence of mass terms for gauge bosons. While this is not problematic for massless photons, it poses a challenge for Z and W bosons, which have masses of 91.2 and 80.3 GeV, [44][45] respectively. Introducing mass terms for these heavy bosons and other massive particles observed in experiments would violate gauge invariances in the Lagrangian. To address this, an additional complex scalar field doublet ϕ (the Higgs field) [18, 46] is introduced, responsible for generating observed particle masses. Defining the Higgs potential as:

$$V(\phi) = \mu^2 \phi^{\dagger}\phi + \lambda(\phi^{\dagger}\phi)^2 \tag{1.14}$$

and the Lagrangian is given by:

$$\mathcal{L}_{Higgs} = (D^{\mu}\phi)^{\dagger}(D_{\mu}\phi) - V(\phi) \tag{1.15}$$

where μ and λ represent the mass and field self-interaction parameters, respectively. The first term in this Lagrangian accounts for the kinetic and interaction terms between the scalar field and the gauge fields. The potential of the Higgs field is $V(\phi)$, depicted in Figure 1.2.

Importantly, the Higgs potential has the vacuum expectation value at $v = \sqrt{\frac{-\mu^2}{\lambda}}$, not at $\phi = 0$. The shape of the potential leads to infinitely degenerate states with minimal energy. The selection of any of these states results in the spontaneous breaking of the EW symmetry. One can make a random choice:

$$\phi_0 = \frac{1}{\sqrt{2}} \begin{pmatrix} 0 \\ v \end{pmatrix} \tag{1.16}$$

Following this choice, the Higgs doublet resulting from expanding the potential around the ground state:

$$\phi(x) = \frac{1}{\sqrt{2}} \begin{pmatrix} 0 \\ v + h(x) \end{pmatrix} \tag{1.17}$$

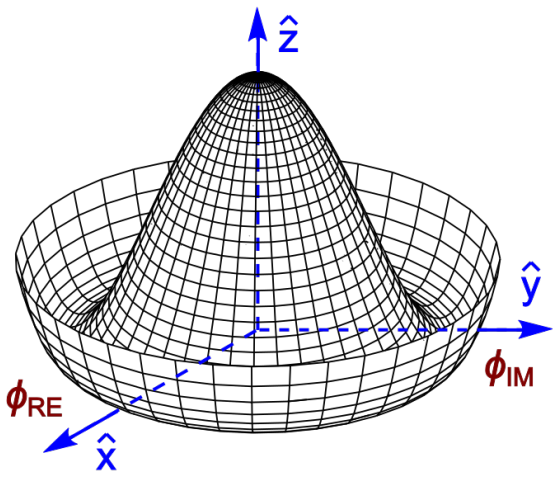

Figure 1.2: Illustration of the Higgs potential in the SM [2].

In order to confer mass upon gauge bosons, a degree of freedom corresponding to the longitudinal polarization of the gauge boson must be absorbed by the gauge field. The complex scalar Higgs field provides this additional degree of freedom. Upon rearranging these degrees of freedom, massive bosons and the Higgs boson which is a real scalar with one degree of freedom emerge. Now, the kinetic term in the Higgs Lagrangian includes

mass terms for the gauge bosons, and the potential term describing the self-interaction of the Higgs boson as follows:

$$(D_\mu\phi)^\dagger(D_\mu\phi) = \frac{1}{2}(\partial_\mu h)(\partial_\mu h) + \frac{g^2}{4}(v+h)^2 W_\mu^+ W_\mu^- + \frac{1}{8}(g^2+g'^2)(v+h)^2 Z_\mu Z_\mu \quad (1.18)$$

$$V(\phi) = \frac{\mu^2}{2}(v+h)^2 + \frac{\lambda}{4}(v+h)^4 \quad (1.19)$$

The masses of the W and Z bosons, as well as their interactions with the Higgs boson, are directly determined from the second and third terms of Equation 1.18. Conversely, as the photon lacks interaction with the Higgs boson, it has zero mass. The gauge boson and Higgs bosons have the following masses:

$$M_W = \frac{1}{2}gv, \quad M_Z = \frac{1}{2}(g^2+g'^2)v, \quad M_A = 0, \quad M_H = \sqrt{2\lambda v^2} \quad (1.20)$$

Furthermore, the Higgs field provides a method within the SM Lagrangian to generate masses for fermion while preserving gauge invariance. Explicitly incorporating fermion masses is prohibited within the $SU(2)_L \times U(1)_Y$ symmetry due to the implication of mixing between the left- and right-handed components of fermions. Nevertheless, the Higgs doublet enables for the representation of fermion masses through a Yukawa Lagrangian:

$$\mathcal{L}_Y = -y_d \overline{Q}_L \phi d_R - y_u \overline{Q}_L \tilde{\phi} u_R - y_l \overline{L}_L \phi l_R + \text{h.c.} \quad (1.21)$$

In this context, $\overline{Q}_L = (\overline{u}_L, \overline{d}_L)$ and $\overline{L}_L = (\overline{\nu}_L, \overline{l}_L)$ represent left-handed doublets for quarks and leptons within a single family. Correspondingly, u_R, d_R, and l_R denote the respective right-handed fermion singlets. The fermion masses are defined as:

$$m_f = \frac{y_f v}{\sqrt{2}} \quad (1.22)$$

It is crucial to note that in the SM, the Yukawa couplings y_f are independent variables, leading to an inability to predict fermion masses theoretically. These masses must be determined experimentally. The substantial differences in fermion masses among different generations remain a puzzle in particle physics within the SM framework. The subsequent Section offers insights into natural phenomena that the SM has yet to comprehensively explain.

In summary, the SM preserves local symmetry under $SU(3)_C \times SU(2)_L \times U(1)_Y$. The local symmetries, $SU(2)_L \times U(1)_Y$ for electroweak interactions and $SU(3)_C$ for strong interactions, lead to the conservation of specific quantities according to Noether's theorem [47][48]. Hence, the local symmetry in the SM implies the conservation of weak hypercharge, isospin, and color charge.

Since the Lagrangian itself is not directly observable and cannot be measured in experiments, predictions are made for event rates and cross sections (σ), which quantify the likelihood of specific processes occurring. The SM can offer precise predictions for cross-sections across a variety of processes.

Nonetheless, the theory does possess notable limitations, which will be explored in the subsequent Section.

1.2 Shortcomings of the SM

The SM, introduced briefly in the preceding Sections, has exhibited remarkable success in explaining particle interactions across diverse energy scales. Its predictions have consistently aligned with experimental findings in particle physics, demonstrating remarkable precision. Nevertheless, there remain unanswered questions that necessitate the expansion of the SM to encompass physics at higher energy levels. Several of the most pressing unresolved inquiries are outlined below.

1.2.1 Hierarchy problem

In the realm of fundamental mass scales in Nature, there exist only two known entities: the Planck scale $M_P = 2.4 \times 10^{18}$ GeV, and the Higgs or electroweak scale $M_{EW} = 10^2$ GeV. These scales differ by approximately 16 orders of magnitude on a hypothetical mass hierarchy. This intriguing observation is commonly referred to as the "hierarchy problem". To investigate this issue, one must first question whether there is a specific reason for the Higgs mass to be near the Planck mass, or indeed, larger than its known value.

Remarkably, in the SM, there exists a rationale for such an expectation. The Higgs boson mass m_h undergoes loop corrections from any particle interacting with the Higgs field. Consider Fig. 1.5, where f represents any fermionic field with a Yukawa interaction with the Higgs field, H. In the SM, all fermionic fields contribute to the Lagrangian via a term of the form $\lambda_f H \bar{f} f$ [3], leading to a correction to the Higgs mass, m_H, given by:

$$m_H^2 \approx m_{H,\text{tree}}^2 - \frac{\mid \lambda_f \mid^2}{8\pi^2}\Lambda_{UV}^2 \tag{1.23}$$

Here, $m_{H,\text{tree}}$ represents the bare Higgs boson mass, m_f is the fermion mass, λ_f signifies the coupling of the Higgs to an SM fermion, and Λ_{UV} stands for an ultraviolet cutoff, set at an energy scale where the SM is surpassed by a more fundamental theory.

A reasonable choice for the cutoff scale would be the Planck scale [49, 50, 51, 52], where gravitational effects reach magnitudes similar to those governed within the SM. However, for $\Lambda_{UV} \sim M_P$, the Higgs boson mass correction becomes on the order of $\Lambda_{UV}^2 \sim 10^{38}$ GeV. Consequently, to achieve the observed Higgs boson mass of $m_H = 125$ GeV, an astonishing fine-tuning [3] of over 30 orders of magnitude is required. Since there is no inherent explanation for this cancellation within the SM, the hierarchy problem strongly suggests the need for a new theory. SUSY addresses the hierarchy problem by introducing new particles that contribute with equal size but opposite signs, effectively canceling the dependence on Λ_{UV}^2.

It's noteworthy that while mass correction terms exist for all particles in the SM with nonzero mass, the correction terms for gauge bosons and fermions grow logarithmically in the cutoff scale Λ_{UV}, as opposed to quadratically, as observed in the case of the Higgs field. In this context, fine-tuning appears to be primarily an issue for the Higgs self-interaction. However, since other particles derive their masses from the Higgs vacuum expectation value, all fields in the SM are influenced by this concern.

1.2.2 Running of the gauge couplings

It is widely acknowledged that the SM does not provide a complete description of nature, as it notably lacks an explanation for gravity. Instead, it is considered an effective low-energy approximation of a unified field, revealing its fully gauged structure at higher energies. *Gauge coupling unification* [53] proposes the idea that fundamental forces could possess comparable strengths, suggesting a convergence of their respective coupling constants - g for the weak force, g' for electromagnetism, and g_s for the strong force - at high energy scales. These coupling constants, denoted as g', g, and g_s, are associated with the fine-structure constants α_1, α_2, and α_3, respectively. The renormalization group equations (RGEs) govern the evolution of these coupling constants concerning the energy scale, represented as:

$$\alpha_i^{-1}(Q) = \alpha_i^{-1}(m_Z) + \frac{b_i}{2\pi} \log \frac{Q}{m_Z}$$

Here, $\alpha_i^{-1}(m_Z)$ denotes the coupling constant evaluated at the electroweak scale, and b_i signifies the beta function coefficients. These coefficients, unique to each coupling, are contingent upon the particle content of the theory and dictate how the coupling constants fluctuate with varying energy scales. However, solving these equations within the framework of the SM for the three coupling constants does not reveal a convergence point, as illustrated in Figure 1.3.

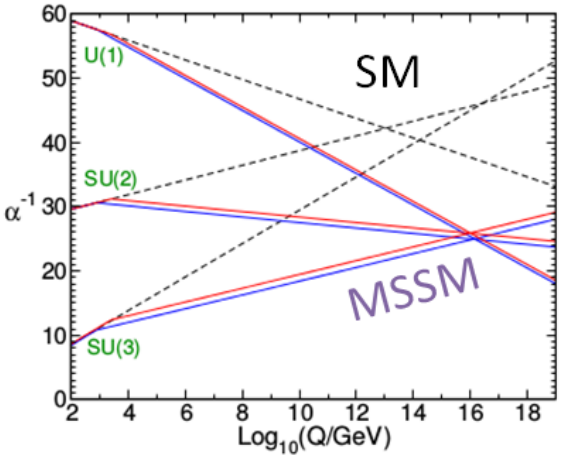

Figure 1.3: Evolution of the inverse gauge couplings α_a^{-1}(Q) a = 1, 2, 3 as a function of the energy scale Q in the SM (dashed lines) and the MSSM (solid lines) [3].

Achieving grand unification becomes feasible by incorporating a Beyond SM (BSM) theory, like SUSY. In Supersymmetric frameworks, the presence of Supersymmetric particles alters the evolution of gauge couplings, leading to an approximate convergence around a scale $M_U \sim 1.5 \times 10^{16}$ GeV in the Minimal Supersymmetric SM.

1.2.3 Neutrino masses

For a long time, neutrinos were believed to have no mass, a prediction of the SM. However, the discovery of neutrino oscillations, where one neutrino flavor transforms into another during flight, implies the existence of a nonzero mixing matrix between neutrino flavors and mass states. In essence, neutrinos possess minuscule, albeit nonzero, masses. Only upper bounds have been established for their mass values. The SM lacks a mechanism to account for neutrino masses, and the significant disparity between neutrino masses and those of other SM particles remains unexplained.

1.2.4 Particle nature of Dark Matter (DM)

There are numerous astronomical observations indicating that the visible matter in the universe is insufficient, implying the presence of 'invisible matter' weakly interacting with particles in the SM. This elusive form of matter is known as Dark Matter (DM). Initially, evidence for DM emerged from measuring the rotational speeds of galaxies [54], which contradicted the gravitational influence of visible matter in their outer radius. The DM hypothesis gained support from gravitational lensing experiments [55][56] and analyses of the Cosmic Microwave Background (CMB) by the Planck Collaboration [57], revealing a 27% DM composition in the universe. It is reasonable to assume that, akin to ordinary matter and radiation, DM should be describable by a quantum field theory. If so, its excitations should manifest as particles. However, the SM lacks suitable candidates for DM particles. The DM candidate must be heavier than weakly interacting SM particles (like neutrinos) to be non-relativistic and form large-scale structures seen in galaxies. Such a particle would also need to interact through gravity and possibly weak forces. Being 'dark', this field must not couple with photons to remain unseen and should not couple with strong forces. Theories beyond the SM often propose Weakly Interacting Massive Particles (WIMPs) [58, 59] to explain these observations.

1.2.5 Gravity

One of the most glaring limitations of the SM is its exclusion of gravitational interaction, one of the four fundamental forces. The modern theory of gravity, General relativity, operates within the framework of classical physics and appears fundamentally incompatible with the quantum mechanical SM.

1.2.6 Matter-antimatter asymmetry

The observable universe presents a curious imbalance: there is a surplus of matter and a glaring scarcity of antimatter [60]. This phenomenon remains enigmatic, and the SM fails to provide a satisfactory explanation. As per the Big Bang hypothesis, the universe should have produced equal amounts of matter and antimatter, yet the predominant composition of the present universe is matter. The Sakharov conditions [61] require a process that disrupts the equilibrium by generating differing quantities of matter and antimatter, violating symmetries of baryon number (B), charge (C) [43], and charge parity (CP) [62, 63]. This is necessary to account for the observed imbalance in the universe. Although the SM allows for limited CP violation through quark mixing, it falls short in explaining the observed matter-antimatter asymmetry. Moreover, experimental evidence indicates that baryon number is conserved in fundamental particle interactions. To unravel the mystery of the universe's matter-antimatter asymmetry, novel sources of baryon number violation and CP violation are essential. The presence of sterile neutrinos stands as a potential solution to this puzzle [64].

Many of the challenges mentioned above find potential solutions through the introduction of Beyond SM (BSM) theories. One such model, known as SUSY, will be explored in the following Chapter 2.

1.3 Beyond the SM: Supersymmetry (SUSY)

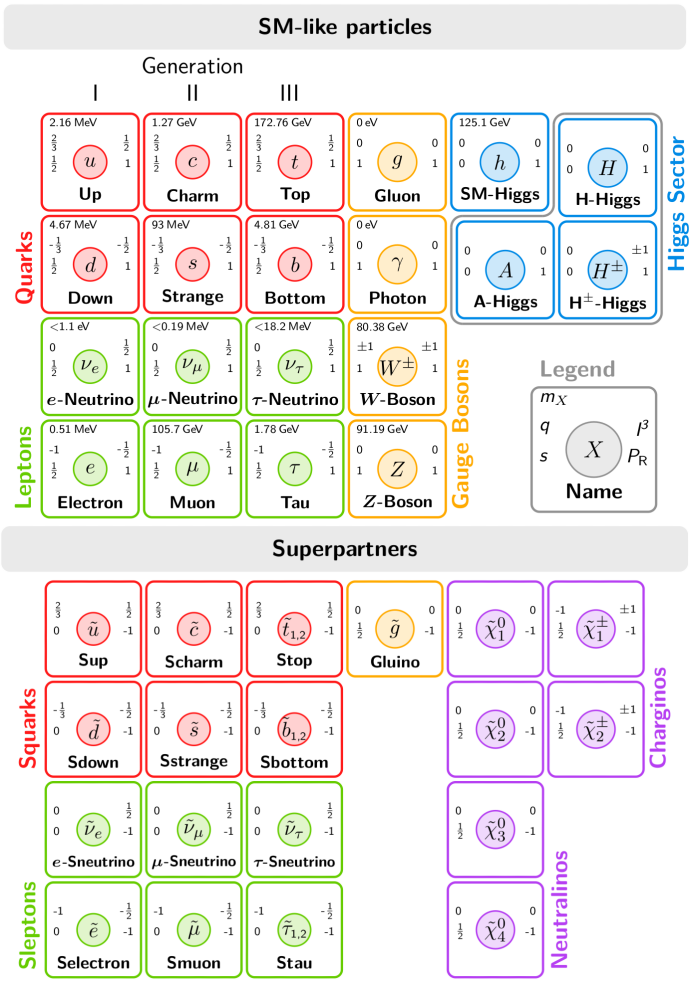

Figure 1.4: Particle content of the MSSM in their mass eigenstates. The MSSM predicts an expanded Higgs sector featuring extra neutral and charged Higgs bosons [4]

SUSY stands out as one of the most compelling extensions to the SM. This extension introduces a novel symmetry wherein a generator, denoted as Q, converts bosons possessing integer spin into fermions with half-integer spin and vice versa [3]:

$$Q|\text{Fermion}\rangle = |\text{Boson}\rangle, \quad Q|\text{Boson}\rangle = |\text{Fermion}\rangle \tag{1.24}$$

This additional symmetry anticipates the presence of fermionic and bosonic partners for each SM particle. These partners have different spins but retain the same charges.

1.3.1 Motivation for SUSY

There are several reasons supporting the concept of SUSY, which are outlined below.

Solution to the hierarchy problem

If SUSY is indeed a fundamental aspect of nature, it requires the addition of new fields and interactions alongside the Higgs field. Specifically, for every fermionic interaction of the form $\lambda_f H \bar{f} f$, a corresponding complex scalar superpartner $\tilde{S}$ contributes an interaction of the form $\lambda_{\tilde{S}} |H|^2 |\tilde{S}|^2$.

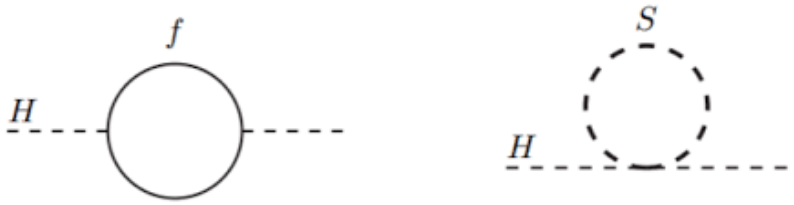

Figure 1.5: Quantum corrections originating from a Dirac fermion f and a scalar S have been studied, influencing the Higgs squared mass parameter m_H^2 [3].

When considering quantum corrections depicted in Figure 1.5, incorporating contributions from both scalar degrees of freedom, the correction to the Higgs mass can be expressed as follows:

$$m_H^2 \approx m_{H,tree}^2 - \frac{|\lambda_f|^2}{8\pi^2}\Lambda_{UV}^2 + \frac{\lambda_{\tilde{S}}}{16\pi^2}\Lambda_{UV}^2 \tag{1.25}$$

It is crucial to note that due to the identical masses of particles and their superpartners, $\lambda_{\tilde{S}} = |\lambda_f|^2$. Consequently, the terms quadratic in λ_{UV} precisely cancel out, providing an elegant solution to the hierarchy problem, as illustrated in Figure 1.5.

Gauge coupling unification

The behavior of gauge couplings is influenced by energy levels. Using the renormalization group equations, these alterations can be projected from the electroweak scale to higher energies. In the SM, couplings fail to unify at high energies. However, in the Minimal Supersymmetric SM (MSSM) [65], gauge couplings do converge at elevated energies, suggesting the possibility of a Grand Unified Theory. Figure 1.3 illustrates the comparison of the energy-dependent running gauge couplings in both the SM and the MSSM.

Dark matter candidate

The presence of Dark Matter (DM), constituting about a quarter of the universe's energy density, is not explained by the SM of particle physics. Interestingly, stable Weakly-Interacting Massive Particle (WIMP), influenced by new physics at the TeV scale, could potentially explain DM. If it remains stable, the Lightest Supersymmetric Particle (LSP) emerges as a viable candidate for DM [66].

1.3.2 Minimal supersymmetric SM (MSSM)

The Minimal Supersymmetric SM (MSSM) stands as the most straightforward extension to the SM, introducing the minimal set of new particles and interactions consistent with SUSY alongside the existing SM constituents. Within the MSSM framework, superpartners are introduced for SM fermions and bosons, organized into irreducible representations of Lie algebras known as "supermultiplets". Each supermultiplet encompasses an SM particle and its corresponding superpartner. Vector supermultiplets depict spin-1 SM vector bosons and their superpartners as spin-1/2 fermions referred to as gauginos. Chiral supermultiplets, on the other hand, represent SM spin-1/2 fermions and their superpartners as spin-0 scalars. The symbols for SUSY particles typically mirror those of the corresponding SM particles, but with a tilde above. The scalar partners of fermions are prefixed with "s-"

and are termed “sfermions” (for instance, the superpartner of the electron is the selectron), while the fermionic partners of gauge bosons are suffixed with “-ino” and are denoted as “gauginos” (for example, the superpartner of the photon is the photino). Figure 1.4 provides a summary of the MSSM particle content.

R-Parity

The Minimal Supersymmetric SM (MSSM) adheres to conserving a multiplicative R-parity [67], defined as:

$$P_R = (-1)^{3(B-L)+2s} \tag{1.26}$$

where L denotes the lepton number, B represents the baryon number, and s signifies the spin of the particle. Under this rule, all particles in the SM possess P_R = +1, whereas MSSM particles such as squarks, sleptons, gauginos, and higgsinos possess $P_R = -1$. This conservation principle finds strong phenomenological support, preventing proton decay, an event not observed in experiments. R-parity conservation yields significant implications: firstly, the LSP remains stable due to R-parity conservation, offering a potential candidate for Dark Matter (DM) if weakly coupled to SM particles. Secondly, it ensures that sparticles produced at colliders always occur in pairs. The SUSY searches detailed in Chapters 3 and 4 of this thesis assume R-parity conserving SUSY models, making this assumption integral to subsequent discussions. R-parity violation (RPV) [3] would imply the violation of lepton and/or baryon number conservation. In such scenarios, even the LSP, such as the neutralino, can decay, provided the corresponding coupling is sufficiently small, allowing it to remain a viable DM candidate.

Particle spectrum of the MSSM

In the Minimal Supersymmetric SM (MSSM), the presence of two Higgs doublets introduces 8 degrees of freedom and their corresponding superpartners. Five Higgs bosons arise

after electroweak symmetry breaking: two neutral scalars h and H^0 (where the lighter field h corresponds to the SM Higgs), and one neutral pseudoscalar A^0, two charged scalars H^+ and H^-. The supersymmetric counterparts of the Higgs doublets are referred to as "higgsinos".

Within the electroweak sector governed by $SU(2)_L \times U(1)_Y$ gauge symmetry, spin-1 gauge bosons $W^\pm$, Z, and γ coexist with three "winos" $\widetilde{W}$ (partners of $SU(2)_L$ gauge bosons) and a "bino" $\widetilde{B}$ (a $U(1)_Y$ gaugino). Due to electroweak symmetry breaking, higgsinos and electroweak gauginos undergo mixing. Consequently, winos and binos, not being mass eigenstates due to broken $SU(2)_L \times U(1)_Y$ symmetry, mix with fields possessing the same charge but different $SU(2)_L \times U(1)_Y$ quantum numbers. Neutral higgsinos ($\widetilde{H}_u^0$ and $\widetilde{H}_d^0$) and neutral gauginos ($\widetilde{B}$ and $\widetilde{W}^0$) combine to form mass eigenstates known as neutralinos, denoted as $\tilde{\chi}_i^0$, where i = 1, 2, 3, 4. The masses of these neutralinos are primarily determined by mass parameters of the bino, wino, and higgsino. Charged winos ($\widetilde{W}^+$ and $\widetilde{W}^-$) and charged higgsinos ($\widetilde{H}_u^+$ and $\widetilde{H}_d^-$) undergo mixing, resulting in chargino mass eigenstates denoted as $\tilde{\chi}_i^\pm$, where $i = 1, 2$, and they carry electric charges of ± 1. Following convention, these mass eigenstates are labeled in ascending mass order, such that $m_{\tilde{\chi}_1^\pm} < m_{\tilde{\chi}_2^\pm}$ for charginos and $m_{\tilde{\chi}_1^0} < .... < m_{\tilde{\chi}_4^0}$ for neutralinos.

The lightest neutralino, denoted as $\tilde{\chi}_1^0$, usually considered as the LSP, serves as a potential Dark Matter candidate unless a lighter gravitino ($\widetilde{G}$) is present, or if R-parity is not conserved, given its unique capability among MSSM particles to fulfill this role.

Squarks ($\tilde{q}$) are the scalar counterparts of quarks, with one variant corresponding to each SM quark. Specifically, the superpartners of the top and bottom quarks are distinct from the lighter squarks and are denoted as stop and sbottom, respectively. These particles undergo decays leading to quarks and neutralinos or charginos, which subsequently undergo further decays. Gluinos ($\tilde{g}$) are Majorana fermionic partners of gluons, signifying that they are their own antiparticles. Due to their strong interaction, squarks and gluinos can be significantly produced in hadron colliders like the LHC.

Gluino decay proceeds exclusively through a squark, either on-shell or virtual, in two-body decays. Specifically, gluinos decay into quark-squark pairs, a dominant process given the robust gluino-quark-squark coupling with QCD strength. Notably, if the top and bottom squarks are lighter than other squarks, gluino decays into top-stop or bottom-sbottom pairs become the dominant two-body decay modes. However, if all squarks are heavier than gluinos, gluino decays occur exclusively through off-shell squarks, leading to three-body decays involving neutralinos and charginos.

Sleptons ($\tilde{\ell}$) are the scalar counterparts of the leptons in the SM. Unlike strongly interacting particles, sleptons exhibit weaker interactions and are usually generated with lower cross-sections in hadron colliders, especially if they are relatively light. Sleptons are primarily identified in the decays of charginos and neutralinos, provided they are light enough to serve as decay products.

In the context of squarks and sleptons, helicity mixing occurs exclusively within the third generation sector, where the scalar counterparts of the left- and right-handed components of a fermion (f_L, f_R) combine into f_i, denoted by i = 1, 2. This phenomenon is observed in stop ($\tilde{t}$) and sbottom ($\tilde{b}$) squarks as well as in stau ($\tilde{\tau}$) sleptons. Since sfermion mixing is primarily influenced by the Yukawa coupling, and the Yukawa couplings of the first and second generations are negligible, it is expected that first and second-generation squarks and sleptons remain mostly unmixed, often represented as f_L and f_R.

Another consequence of the insignificant Yukawa coupling is the near-identical masses of first and second-generation sfermion pairs. This results in seven nearly mass-degenerate, uncombined pairs of sfermions: ($\tilde{e}_R$, $\tilde{\mu}_R$), ($\tilde{e}_L$, $\tilde{\mu}_L$), ($\tilde{\nu}_e$, $\tilde{\nu}_\mu$), ($\tilde{u}_R$, $\tilde{c}_R$), ($\tilde{u}_L$, $\tilde{c}_L$), ($\tilde{d}_R$, $\tilde{d}_R$), ($\tilde{d}_L$, $\tilde{d}_L$). The specific masses of all supersymmetric particles depend on the values of parameters within the Minimal Supersymmetric SM (MSSM). Consequently, the MSSM does not provide precise predictions for the sparticle masses. However, to resolve the hierarchy problem, it is anticipated that all mass parameters are on the order of the soft SUSY breaking

scale (m_{soft}), typically expected to be within the TeV range.

The final member of the Supersymmetric particle family is the gravitino ($\widetilde{G}$), which acts as the superpartner of the graviton. According to theoretical expectations, gravity is conveyed by the spin-2 graviton. Consequently, the gravitino is anticipated to be a spin-3/2 particle within the framework of SUSY. In specific SUSY-breaking models known as gauge-mediated SUSY-breaking (GMSB) [68, 69, 70] models, gravitinos assume the role of the LSP.

SUSY breaking

SUSY is not an exact symmetry in the observable universe; otherwise, the masses of super-partners would mirror those of their SM counterparts. Since no experimental evidence of supersymmetric particles has been observed at colliders, it is deduced that SUSY particles must be more massive than their SM counterparts. Consequently, SUSY must be a broken symmetry. This can occur through explicit symmetry-breaking terms incorporated into the Lagrangian or via spontaneous symmetry-breaking, akin to the mechanism observed in the Higgs mechanism [46][18].

The breaking of this symmetry can reintroduce quadratic divergences into the Higgs mass correction terms. To mitigate this, many researchers advocate for a solution involving soft SUSY breaking [71, 72]. In this scenario, the symmetry breaking happens at a new mass scale, denoted as m_{soft}, analogous to how the spontaneous symmetry breaking in the Higgs mechanism gives rise to the electroweak scale.

The comprehensive Minimal Supersymmetric SM (MSSM) Lagrangian encompasses over 100 independent parameters, with 32 representing masses of particles yet to be discovered and the remainder arising from soft SUSY breaking terms. Navigating this extensive parameter space poses a formidable challenge for experimental constraints. A significant portion of the uncertainty within the MSSM stems from our incomplete understanding of

the precise mechanism governing soft SUSY breaking.

To address this complexity, various supersymmetric models have been proposed, each offering a distinct mechanism for breaking SUSY. These models aim to predict the MSSM's particle spectrum with fewer parameters. Alternatively, some approaches reduce the parameter space by imposing additional phenomenological constraints. This thesis discusses several prominent supersymmetric models, briefly outlined below.

Simplified model spectrum

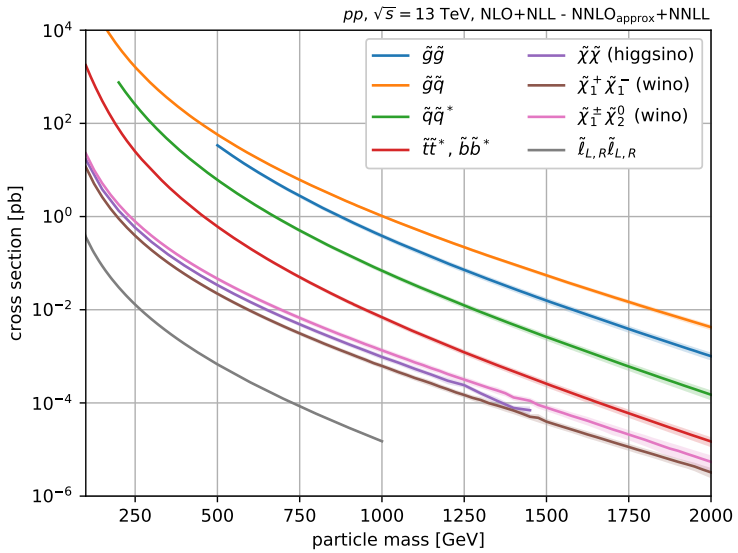

Figure 1.6: SUSY cross sections for the LHC operating at $\sqrt{s} = 13$ TeV [5]

The phenomenological Minimal Supersymmetric SM (pMSSM) [73] stands as one of the most comprehensive and realistic representations of SUSY. However, exploring the 19 parameters of the pMSSM in experimental searches proves exceptionally challenging and time-consuming. Experimental efforts often concentrate on specific parameters or SUSY particles. Consequently, it proves highly beneficial to consider an effective Lagrangian involving only a handful of parameters, such as the masses of relevant SUSY particles and

their interactions. These simplified descriptions, known as Simplified Models [74][75], are tailored to experimental requirements, directly parametrizing collider physics observables. These include the masses of SUSY particles involved in the process, their production cross-sections, and decay branching fractions. Typically, other SUSY particles are assumed to be decoupled or too massive to contribute to the final state under study. The degrees of freedom of the model are further limited when specific experimental signatures are assumed to have 100% branching fractions. This thesis explores several simplified SUSY models, instrumental in calculating production rates for specific processes at the LHC. Notably, the production cross-sections for all SUSY channels illustrated in Figure 1.6 decrease as mass increases.

1.3.3 Gauge-mediated supersymmetry breaking (GMSB)

A different strategy to simplify the complexity of the parameter space involves adopting specific mechanisms for breaking SUSY. These models typically consist of a "visible sector", housing the particles of the Minimal Supersymmetric SM (MSSM), which includes both the SM particles and their corresponding superpartners. Alongside this, there exists an additional "hidden sector", responsible for initiating the process of SUSY breaking.

In the context of gauge-mediated SUSY breaking (GMSB) models, a set of chiral supermultiplets, known as "messengers", acts as intermediaries, connecting the hidden and visible sectors. Additionally, GMSB requires the integration of gravity into SUSY. This leads to the formulation of "supergravity" [76], introducing a massless spin-2 graviton and a spin-3/2 gravitino denoted as $\widetilde{\mathrm{G}}$. Both these particles mediate the gravitational force before SUSY breaking occurs. During the process of SUSY breaking, the gravitino acquires mass, analogous to how the $\mathrm{W}^{\pm}$ and Z bosons obtain their masses in the Higgs mechanism.

In this supergravity model, SUSY breaking can take place through either gravitational or gauge interactions. Specifically, in GMSB models, SUSY breaking in the hidden sector

is transmitted to MSSM particles through ordinary gauge interactions. A key feature of this scenario is that the gravitino is expected to have a substantially lower mass compared to other sparticles, making it a natural candidate for the LSP. Chapter 4 provides further insights into the ongoing efforts to explore these GMSB models.

Chapter 2

The LHC and the CMS detector

This chapter provides a comprehensive overview of the Large Hadron Collider (LHC), the world's most powerful particle accelerator, and the Compact Muon Solenoid (CMS) detector, a key experiment at the LHC. At the LHC, proton bunches are accelerated to near the speed of light, resulting in collisions that produce novel and massive particles. The CMS detector plays a crucial role in identifying these particles by reconstructing their paths and energy deposits.

Section 2.1 gives a summary of the LHC, its functioning, and the key experiments conducted there to analyze collision data. Additionally, the structure of the CMS detector is detailed in Section 2.2.

2.1 The Large Hadron Collider (LHC)

2.1.1 Outline of the accelerator complex

Within the facility at the European Organization for Nuclear Research (CERN), there are multiple accelerators, with the Large Hadron Collider (LHC) [23, 24] being the final stage in this sequence. At the LHC, protons are accelerated to an energy of 6.5 TeV. The LHC is a synchrotron, with a circumference of 27 km, and is situated approximately 100 meters underground at the border between France and Switzerland.

Two basic ingredients of the LHC accelerator; are electric fields for acceleration in the longitudinal direction of the beam and magnetic fields to change the trajectory of the beam or "bending". The accelerating electric fields come in the form of RF cavities, devices that oscillate the electromagnetic fields very rapidly to provide a kick of acceleration to charged

particles entering them. The bending magnets provide a magnetic field transverse to the direction of travel of the beam and so the Lorentz force is exerted perpendicular to both the beam velocity and magnetic field, towards the center of the ring.

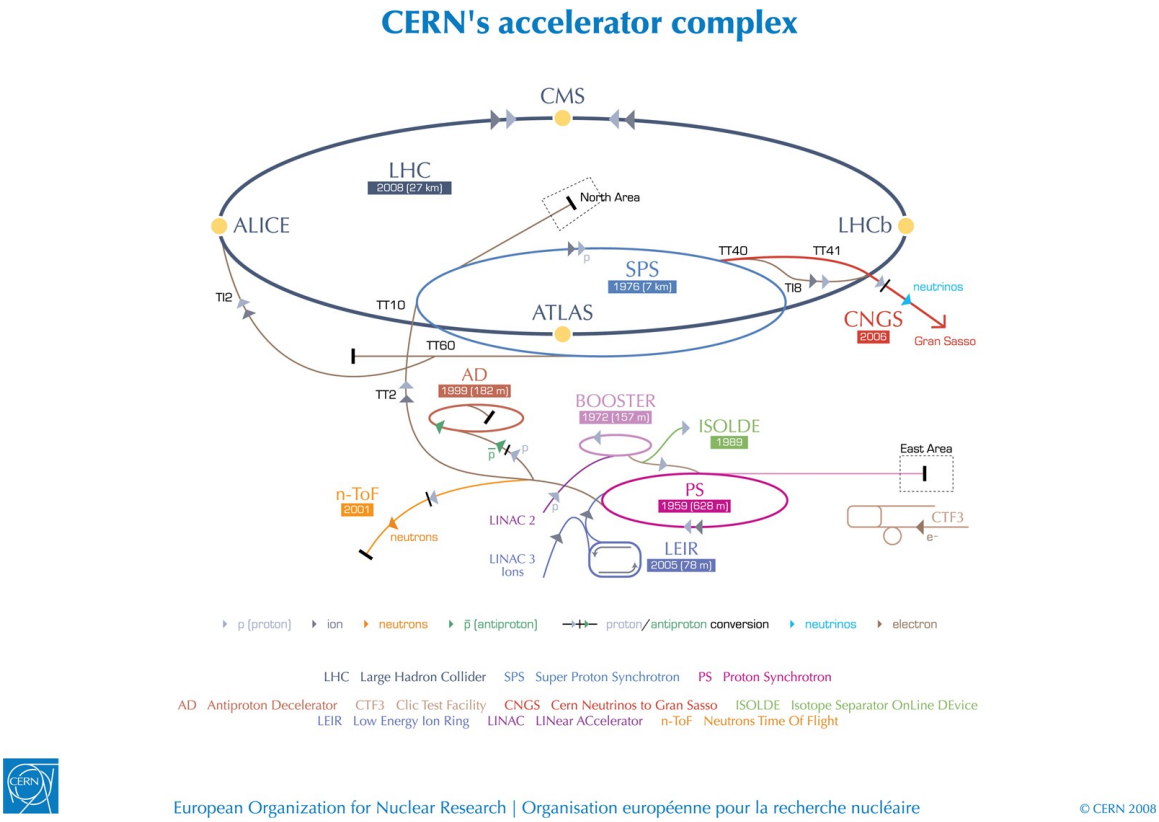

Figure 2.1: Schematic layout of the full accelerator complex [6]

The protons that are circulated through the LHC start in the form of hydrogen gas stored in a small cylinder. Hydrogen gas is first ionized forming negative hydrogen ions and fed to a linear accelerator (Linac2/Linac4) that uses radio frequency (RF) cavities to accelerate these ions to an energy of 50 MeV.

The process begins with hydrogen ions from Linac2/Linac4, stripped of electrons, and accelerated to 1.4 GeV through the Proton Synchrotron Booster (PSB), comprised of four stacked synchrotron rings. These protons then progress to the larger Proton Synchrotron (PS), where their energy is increased to 26 GeV. From there, they enter the Super Proton

Synchrotron (SPS) [77, 23], reaching an energy level of 450 GeV. Subsequently, these protons are injected into the LHC ring, where their energy is ramped up from 450 GeV to 6.5 TeV. At this point, quadrupole magnets squeeze the beams at their interaction points, initiating collisions.

Over several hours, the beam intensity naturally decreases. When the luminosity reaches a low point, the beams are directed out of the accelerator ring, and all their energy is absorbed by a large block known as the "beam dump". For an overview of all CERN accelerators [24], refer to Figure 2.1.

A total of 1232 superconducting dipole magnets that are each 15 m long are used in LHC. These magnets are made of a niobium-titanium alloy and are cooled using superfluid helium at a temperature of 1.9 K. They generate a magnetic field of 8.3 T that bends the paths of the protons to keep them inside the ring. The LHC ring is equipped with 392 quadrupole magnets, which are used to focus the proton bunches by compressing them either vertically or horizontally. A total of 16 RF cavities are used to accelerate the beam, so the beams cannot be continuous and are instead clumped together into bunches. Nominally, the accelerated protons would be grouped into 2808 bunches of $\sim 10^{11}$ protons, separating about 7.5 meters between them. This means that a bunch crossing happens every 25 ns at the interaction points [77, 23]. The bunches are not evenly spaced around the circumference of the ring but are grouped together in "trains".

2.1.2 Experiments at LHC

The Large Hadron Collider (LHC) operates by colliding two beams of proton or heavy ion bunches traveling in opposite directions at four specific collision points. At these collision points, there are four main experiments: CMS (Compact Muon Solenoid) [78], ATLAS (A Toroidal LHC Apparatus) [79], ALICE (A Large Ion Collider Experiment) [80], and LHCb (Large Hadron Collider Beauty) [81].

ATLAS and CMS, as general-purpose experiments, are designed to exploit the wide range of physics provided by proton or heavy ion collisions at high luminosities. CMS, in particular, will be detailed in the next chapter. ALICE is a specialized detector dedicated to heavy-ion physics, focusing on studying the high-density phase of matter known as quark-gluon plasma. LHCb, on the other hand, is an asymmetric detector specifically constructed to measure CP violation in the interactions of hadrons containing a bottom quark.

In addition to these major experiments, there are three smaller ones: Monopole and Exotics Detector at the LHC (MOEDAL), the Large Hadron Collider Forward (LHCf), and Total Elastic and Diffractive Cross-section Measurement (TOTEM). LHCf investigates particles generated close to the colliding proton beams, while MOEDAL searches for magnetic monopoles and other highly ionizing massive particles using nuclear track detectors. TOTEM, on the other hand, measures the total cross-section and elastic scattering of proton-proton collisions.

Although heavy ion collisions are a vital aspect of the LHC physics program, this thesis focuses on the search for new physics and the performance analysis of a CMS subdetector using proton-proton collision data collected at the LHC by the CMS detector.

2.1.3 LHC operation and parameters

Two crucial parameters at the LHC are the center-of-mass energy ($\sqrt{s}$) and the integrated luminosity ($\mathcal{L}_{int}$). The center-of-mass energy determines which particles or processes can occur within the collider, while the luminosity decides whether the process happens at a rate suitable for study.

The LHC was initially planned to collide protons at a center-of-mass energy of 14 TeV with a luminosity of $10^{34}\ cm^{-2}s^{-1}$, enabling the discovery of an H boson resembling the SM with a mass of up to 1 TeV. This setup also held the potential to explore physics beyond the SM at the TeV scale. In reality, protons collided at energies of 7 TeV and 8 TeV in

2011 and 2012 (referred to as Run 1). Following Run 1, the LHC underwent a prolonged period known as a long shutdown (LS) during which necessary upgrades were implemented. Subsequent to this first long shutdown (LS1), the center-of-mass energy was raised to 13 TeV for proton-proton collisions taking place from 2015 to 2018, commonly referred to as Run 2. The second long shutdown (LS2) was from 2019 to 2022 for a series of upgrades, and then it is operating at $\sqrt{s}$ = 13.6 TeV with the beginning of Run 3. As the next step, the High Luminosity LHC (HL-LHC) is planned with the same energy, but with upgraded detectors to collect 3000 fb^{-1} with five times higher instantaneous luminosity.

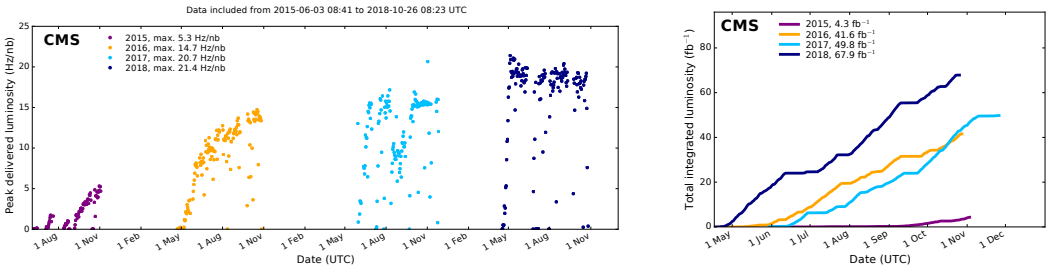

Figure 2.2: Peak luminosity versus day (left plot) and cumulative luminosity versus day (right plot) delivered to CMS for data-taking in 2015 (purple), 2016 (orange), 2017 (light blue), and 2018 (navy blue) are shown [7]

Luminosity is assessed through two indicators: instantaneous and total integrated luminosity. Instantaneous luminosity ($\mathcal{L}$) [23] quantifies the number of collisions per unit time and transverse area, given by:

$$\mathcal{L} = \frac{f N_b n_1 n_2}{4\pi\sigma_x\sigma_y} \tag{2.1}$$

which implies that the instantaneous luminosity depends on the properties of the colliding proton bunches. f is the revolution frequency set at 11.2455 kHz, N_b is the number of bunches in each beam, n_1 and n_2 are the proton counts in each of the two colliding bunches, and σ_x and σ_y denote the horizontal and vertical transverse beam sizes at the interaction point, respectively. In Run 2, luminosities exceeding $2 \cdot 10^{34}\ cm^{-2}s^{-1}$ [7], which is double the intended value, were attained, as illustrated in Figure 2.2. The total amount of data

collected during certain data-taking periods is characterized by the integrated luminosity, $\mathcal{L}_{int}$ which is calculated by integrating the instantaneous luminosity with respect to time:

$$\mathcal{L}_{int} = \int \mathcal{L}\, dt \tag{2.2}$$

Units of $\mathcal{L}_{int}$ are given in units of inverse cross-section, where typically the unit of cross-section is the barn (1 b = $10^{-28} m^2 = 10^{-24} cm^2$) and more commonly the picobarn (1 pb = 10^{-12} b) and the femtobarn (1 fb = 10^{-15} b). The total integrated luminosity during Run 2 data collection (from 2015 to 2018) is displayed in the right panel of Figure 2.2. This illustrates that overall 163.6 fb^{-1} of proton-proton collisions were delivered to CMS by the LHC. The analyses in this thesis use a data set corresponding to a total integrated luminosity of 137 fb^{-1}. The total number of events for a specific physics process, like a particular SUSY signal channel, is obtained by multiplying the production cross-section for that process by the integrated luminosity:

$$N_{event} = \mathcal{L}_{int} \cdot \sigma \tag{2.3}$$

If a process has a very low cross-section the probability of observing it is increased with a larger luminosity.

The luminosity at the LHC is exceptionally high, causing multiple inelastic proton-proton collisions (pile-up) to occur with each bunch crossing. Pile-up effects include in-time pile-up, which refers to the additional signals from particles originating due to multiple proton-proton collisions happening within the same bunch crossing.

This can be suppressed by using information from the tracker to ensure signals are coming from the desired interaction. Out-of-time pile-up (OOTPU) refers to signals generated by particles resulting from additional proton-proton collisions occurring in bunch crossings right before or after the bunch crossing containing the primary interaction. This largely affects the calorimeters as signals propagate outward it may be the case that signals from the previous bunch crossing are still present or that the signals from the following have entered.

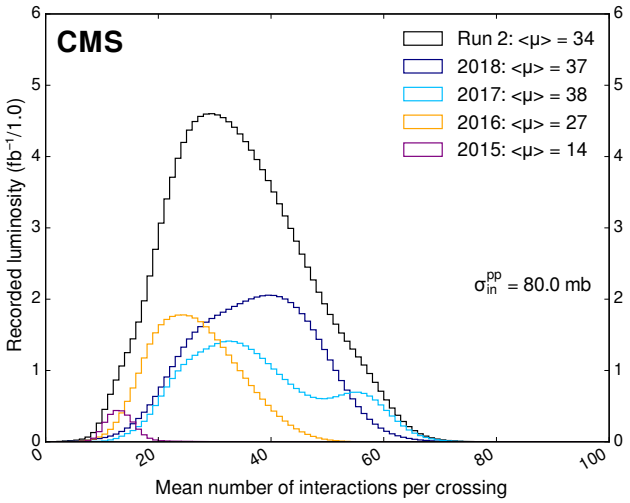

Figure 2.3: Illustration depicting the mean interactions per collision event (pileup) distribution in proton-proton collisions over four years: 2015 (represented in purple), 2016 (in orange), 2017 (in light blue), and 2018 (in navy blue). Additionally, it displays the overall mean values and minimum bias cross-sections [7]

The mean number of interactions per crossing ($\mu = \mathcal{L}\sigma_{inel}/(fN_b)$) depends on instantaneous luminosity ($\mathcal{L}$), inelastic proton-proton collision cross-section (σ_{inel}), collision frequency (f), and the number of bunches per beam (n_b).

Fig 2.3 shows the average interactions per bunch crossing (pileup) recorded by the CMS detector during Run 2 data taking.

2.1.4 Simulating collision events

Simulation plays a crucial role in modeling both SM expectations and the anticipated outcomes of new physics, aiding in the development of targeted analyses. Moreover, simulations are essential for forecasting future scenarios, enabling predictions of the sensitivity of next-generation colliders or detectors for various measurements and searches. In this thesis, simulations are extensively employed to estimate event yields from irreducible background sources, optimize analysis approaches, and even develop data-driven methods for background estimation. This Section focuses on simulating particle collisions prior to their

interactions with a detector, with further details on simulating the detector itself and the particles passing through it provided in Section 2.2.7. In LHC physics analyses, the focus is usually on a specific final state where a particular process of interest takes place. Distinct physics processes are individually simulated to represent those pertinent to a specific analysis. To compute the total expected number of events for a specific analysis, simulated events of all relevant processes are normalized based on their respective cross-sections and then combined.

As protons are composite particles, consisting largely of quarks and gluons, the interaction occurs between the proton composites, also referred to as partons, where the knowledge of the proton composition is collected in a Parton Distribution Function (PDF). The PDF quantifies the probability of finding a specific parton, depending on the four-momentum transfer and the fraction of the longitudinal proton momentum carried by the parton.

The simulation process of an individual collision event can be subdivided into several specific stages, as outlined below. The collisions relevant to physics analysis typically involve large momentum transfer between the two partons in the colliding protons. Events resulting from such collisions referred to as hard scattering [82] processes, can produce massive particles like top quarks or electroweak bosons, which rapidly decay into lighter particles. In conditions of high interaction energies or, equivalently, small distances, Quantum Chromodynamics (QCD) operates in a perturbative manner. Simulating the hard scattering process is the first step of collision event generation.

Based on their characteristics, particles resulting from a hard scatter interaction persist emitting photons and gluons after their formation. In contrast to photons, gluons interact with themselves due to the nonabelian nature of QCD. This means that emitted gluons further emit more gluons, creating a cascading effect. The parton shower, characterized by the emission of an expanding number of gluons, marks a shift from high to low energies. It constitutes the second stage in simulating collision events.

The showering process, where colored gluons and quarks transform into colorless hadrons, continues until the nonperturbative regime of QCD is reached. In the work presented in this thesis, various versions of the PYTHIA program [83] are exclusively utilized to simulate parton showering and hadronization stages in collision events. Many resulting hadrons, particularly those from high-energy quarks and gluons, are heavy and unstable, leading to a sequence of decays until all hadrons become relatively light and stable within the detector's timescale. In this simulation step, the processes of hadronization and subsequent decay are modeled.

In the process of hard scattering, generally, two partons interact, exchanging substantial momentum and leading to the presence of residual colored proton remnants. These remnants then undergo the process of hadronization. Additionally, other partons inside the proton often interact, although typically with lower momentum transfer compared to the hard scattering interaction. The term "underlying event" refers to the collective impact of proton fragment hadronization and secondary interactions among partons inside protons. This underlying event significantly influences the kinematics of particles resulting from the primary hard scattering process. Achieving a precise simulation of this underlying event is crucial for accurately modeling real collision events [84].

The simulation of a proton-proton collision follows a sequential process known as a Markov chain framework. Each step relies on the previous one, and random numbers generated using Monte Carlo (MC) methods dictate the outcomes at each stage. Monte Carlo techniques are extensively used in generating collision events, leading to the common term "MC events" for simulated events. This thesis uses a specialized program to compute matrix elements of hard scattering interactions for generating simulated collision events. These simulations cover essential SM processes and are carried out at the next-to-leading order (NLO) in perturbative QCD. More details on the generation and modeling of the simulation samples for various SM processes relevant to the work in this thesis are given in Section 4.2

and Section 3.2.

2.2 The CMS detector

The Compact Muon Solenoid (CMS) [78] detector is a hermetic cylindrical general-purpose detector that is built to probe the SM primarily near the electroweak scale as well as to enable searches for a wide variety of potential extensions to the SM. The CMS detector, as the name suggests, is optimized for good muon identification. This requires a strong magnetic field, which is generated by the eponymous solenoid, in order to achieve good tracking performance. However, the design strength of the magnetic field constrains the size of the magnet (which explains the "compact" in CMS); and the large material budget of the steel return yoke means that all calorimetry has to happen within the compact volume of the magnet in order to achieve reasonable energy resolution. This requirement on compactness and compatibility with a very strong magnetic field in turn constrains the design of the photodetectors and other electronics used in calorimetry.

CMS has dimensions of 14.6 meters in diameter and 21.6 meters in length, making it roughly half the size of ATLAS. It has a 12 m long superconducting coil to generate a homogeneous magnetic field of up to 3.8 T in the inner detector. The detector comprises a central barrel section and two endcaps, ensuring extensive coverage around the LHC collisions. Its structure consists of concentric layers of subdetectors arranged around the interaction point, as illustrated in Figure 2.4. Each layer is designed to offer precise measurements of the properties of particular types of particles produced at the interaction point. The innermost part of the detector consists of the tracker system. It is placed within the inner magnetic field and detects the curvature of charged particle propagation. The next layer, the electromagnetic calorimeter (ECAL), absorbs photons and electrons and measures their energy. After this, the hadron calorimeter (HCAL) absorbs neutral and charged hadrons and pro-

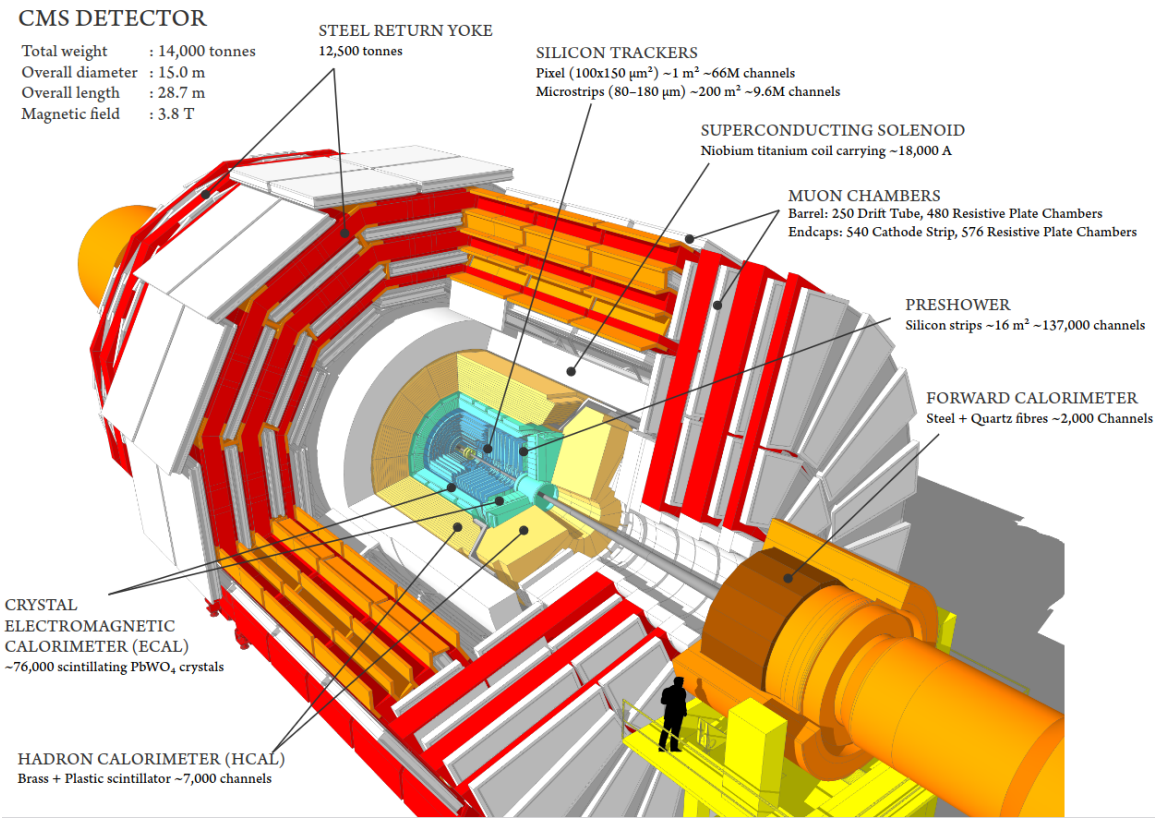

Figure 2.4: A visual representation showing the internal structure of the CMS detector [8]

vides information about their energy. The superconducting solenoid is placed between the HCAL and the iron return yoke. The muon chambers are integrated with the return yoke and measure the muon track curvature in the return solenoid magnetic field that goes up to 2 T. This simplified representation is visually depicted in Figure 2.5, illustrating a cross-sectional view of the CMS detector. The data collected from these individual subdetectors is collectively utilized to identify and reconstruct the particles traversing through the detector. Beginning with an overview of the CMS coordinate system, the next few sections offer some more details on the design of each individual subsystem of the detector.

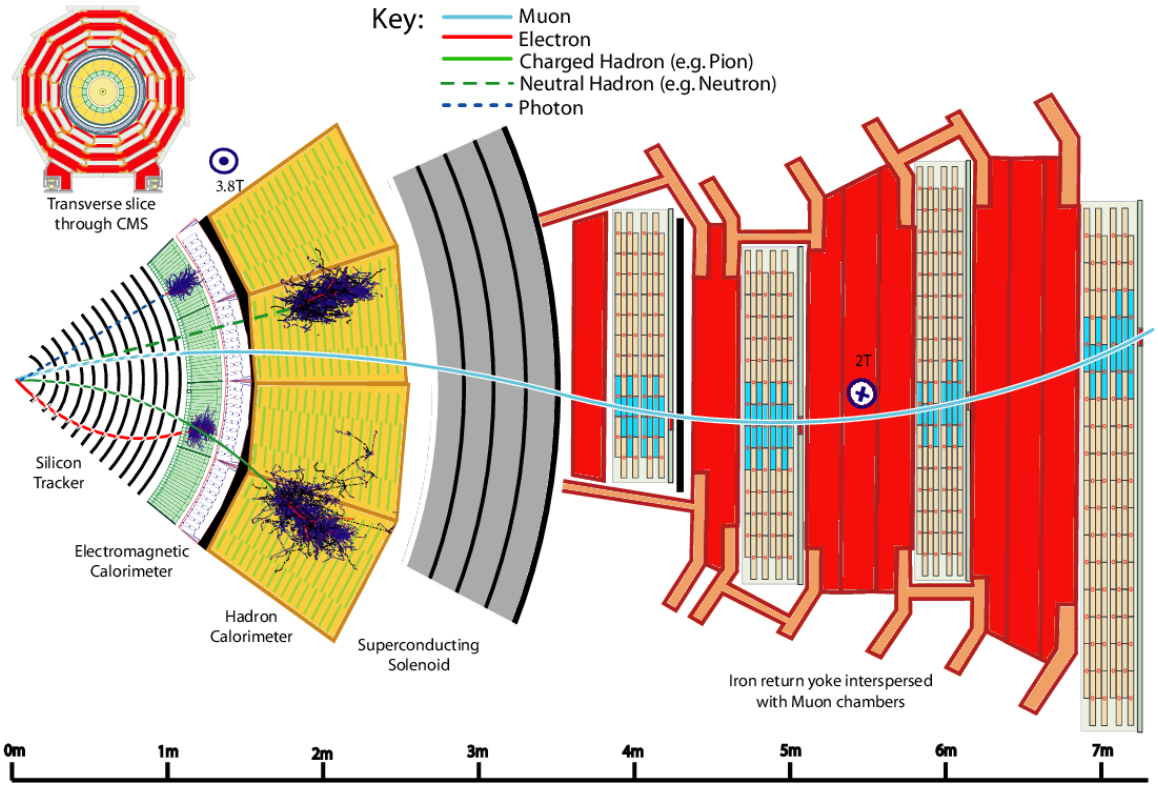

Figure 2.5: An illustration detailing the particular interactions between particles within a transverse slice of the CMS detector, ranging from the area where the beams collide to the muon detector. This illustration includes a positively charged muon and pion, and a negatively charged electron [9]

2.2.1 CMS coordinate system

To measure particles within the CMS detector accurately, a defined coordinate system is crucial. The default CMS coordinate system is established as follows: the origin is the interaction point, situated at the geometric center of the detector. The x-axis extends horizontally toward the center of the LHC ring, the y-axis points vertically upward, and the z-axis aligns parallel to the beam axis, counterclockwise to the proton beam direction when viewed from above the LHC ring. Due to the CMS detector's symmetry around the z-axis, cylindrical coordinates are extensively used.

In this system, the azimuthal angle (ϕ in radians) in the (x, y) plane is measured from

the x-axis ($\phi = \arctan\frac{y}{x}$). The radial coordinate in this plane is represented as r ($r = \sqrt{x^2 + y^2}$). The polar angle (θ) is defined within the (r, z) plane concerning the orientation of the z-axis. Vector components in the (x, y) plane are labeled "transverse", whereas those along the z-direction are termed "longitudinal". The momentum component perpendicular to the z-axis is denoted as transverse momentum (p_T). While longitudinal momentum conservation is not very useful in hadron colliders, $\vec{p_T}$ conservation is expected to be a lot less sensitive to Lorentz boosts along the longitudinal direction. The transverse energy E_T is defined by analogy with p_T as $E_T = Esin\theta$. The chosen coordinate system is specifically

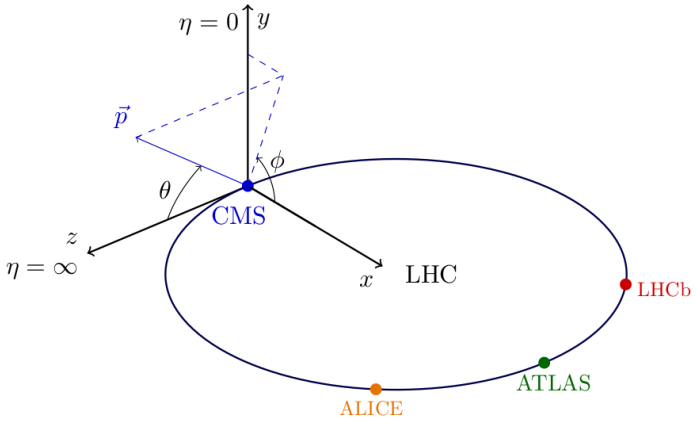

Figure 2.6: This coordinate system is employed for particle measurements within the CMS detector. In this setup, $\vec{p}$ signifies the momentum vector of a particle originating from the central point of the CMS detector [10].

designed to efficiently handle boosts along the proton beam axis. Particle rapidity [85], represented as $y = \frac{1}{2}\ln\frac{E+p_L}{E-p_L}$, where E stands for energy and p_L denotes longitudinal momentum, is a valuable measure in this context. Differences in rapidity are invariant under longitudinal transformations. However, rapidity is energy-dependent, making it less practical for expressing particle directions. Instead, the massless limit approximation of rapidity, called pseudorapidity ($\eta = -\ln\tan(\theta/2)$), is employed. Pseudorapidity is preferred because differences in η remain constant under any arbitrary Lorentz boost along the longitudinal direction. For instance, consider a particle generated in an LHC collision and its

subsequent decay. The difference in pseudorapidity (η) between its decay products remains consistent, regardless of the longitudinal momenta of the incoming partons. This approach ensures uniformity in expressing particle directions, especially in the context of varying energies and momenta.

Angular separations between particles are commonly described using the quantity $\Delta R = \sqrt{\Delta\eta^2 + \Delta\phi^2}$, which remains nearly unchanged under longitudinal boosts. Particle kinematics are typically represented using their $\mathrm{p_T}$, η, ϕ, and energy. An illustration of the coordinate system is given in Fig 2.6.

Missing transverse momentum and impact parameters

When collision events produce neutrinos or hypothetical particles that interact weakly, these particles usually go undetected. Consequently, determining the center of momentum of an observed collision in the longitudinal direction becomes impossible due to the potential presence of weakly interacting particles. However, in the transverse direction, the total momentum approaches zero because the transverse momenta of interacting partons are smaller than their longitudinal momenta. This enables the use of momentum balance in the transverse plane to identify escaping particles. The term 'missing transverse momentum' ($\vec{p}_T^{\,miss}$), or missing transverse energy, refers to the negative vector sum of transverse momentum components of observed particles. This quantity holds great importance in the quest for numerous hypothetical particles and plays a vital role in measuring SM processes. All analyses presented in this thesis utilize p_T^{miss} and other related quantities dependent on it.

Another crucial concept is the impact parameter, which refers to the closest distance between the extrapolated particle trajectory and the collision vertex. This parameter is valuable for identifying the decay products of particles with substantial lifetimes. Particles traveling a significant distance within the detector before decaying often produce decay

products with positive impact parameters. These impact parameters are crucial for identifying jets originating from b-quarks and leptons unrelated to the decay of electroweak bosons.

2.2.2 CMS magnet

The central component of the CMS detector is the superconducting solenoid magnet [78], measuring 6 meters in diameter, 12.5 meters in length, and weighing 200 tons. This magnet generates a strong magnetic field of 3.8 T within its coil, crucial for achieving high-resolution p_T measurements of muons and other charged particles. The solenoid houses the tracking detectors and calorimeters, providing a uniform axial magnetic field. This design prevents energy losses before the calorimeters due to particles showering in the coil material and enhances the connection between particle tracks and calorimeter clusters. Additionally, the magnetic bending power of 4.9 Tesla · meters effectively separates energy deposits from charged and neutral particles when particles hit the inner surface of the calorimeter system perpendicularly. The regular operation involves cooling the solenoid with liquid helium to a temperature of 4.5 K. This configuration supports precise Particle Flow (PF) reconstruction [86], ensuring accurate measurements within the detector.

The magnetic flux is channeled back through a steel return yoke located outside the solenoid, also serving as the absorber material for the muon subdetector. This yoke consists of a barrel section with five wheels and two disks on each end of the endcap. Weighing about 10,000 tons, the iron in the return yoke constitutes a significant portion of the mass of the whole detector. This design ensures a strong magnetic field in the muon subdetector, crucial for achieving precise momentum resolution.

2.2.3 Tracking detector

The tracking detector, the first component particles encounter in CMS, captures spatial measurements (space points) along charged particle paths. These measurements enable precise trajectory reconstruction within the detector, providing accurate charge and momentum information. The uniform magnetic field from the solenoid magnet aids in determining particle properties. Operating at high collision rates of approximately $2 \times 10^{34}\,\mathrm{cm}^{-2}\,\mathrm{s}^{-1}$, where 1000 charged particles must be tracked individually every 25 ns, the tracking detector handles this influx. It's designed to be highly granular, ensuring rapid response and resistance to intense radiation. CMS employs an all-silicon tracking detector to minimize material volume, reducing the effects of multiple scattering, bremsstrahlung, and photon conversions [78, 87]. This detector comprises a pixel detector and a silicon strip tracker, each serving specific roles in the overall setup.

Pixel detector

The pixel detectors are the ones that are closest to the interaction region. Due to the high particle density at small radii, the innermost segment of the tracking detector needs to use pixels to maintain a low occupancy. This pixel detector is made up of individual pixel cells measuring $100\times150\ \mu m^2$, chosen to ensure comparable track resolution in both the (r, ϕ) and z coordinates. The closeness of the pixel detector to the interaction point reduces the impact of uncertainties associated with extrapolating reconstructed particle paths and multiple scattering. It measures the track origin with high precision providing the main input for identifying secondary vertices from long-lived particles such as b hadrons, distinct vertex reconstruction, and separation of prompt from secondary electrons. The pixel detector is split into the barrel and endcap parts. The pixel detector covers the longitudinal range $|\eta| < 2.5$. The initial configuration of the pixel detector used in 2016 consisted of three concentric cylindric layers in the barrel part ("barrel pixel", or BPIX) capped by two layers each

on both sides at nearly fixed z ("forward pixel", or FPIX) and extended from radial lengths ranging from 4.4 cm to 10.2 cm. In 2017, the LHC delivered data to CMS with increased peak luminosity. In order to maintain good tracking performance in this condition the pixel detector was upgraded during the winter shutdown in 2016/2017. The amount of material in the tracking detector volume was approximately halved and it extends up to a radial distance of 16.0 (16.1) cm in the barrel (endcap) region. The main difference of the upgraded pixel detector is an increased number of layers in the barrel (four layers) and the endcap (three layers). Reducing the material content and adding extra measurement layers enhance the precision of all parameters related to reconstructed particle tracks. Consequently, this leads to more effective vertex and track reconstruction, lowering the rates of misidentification. This setup provides a spatial track resolution of 10-40 μm.

The analyses presented in this thesis utilize a variable called the "pixel track seed veto" parameter to identify photons. This variable functions by rejecting any photon associated with a pixel track seed. The pixel track seed is defined as having at least two hits in the pixel detector and is established during the initial tracking iterations. If a photon object is linked to a pixel track seed, it is categorized as an electron in this analysis.

Silicon strip tracker

The CMS silicon strip detector surrounds the pixel detector and utilizes silicon strip modules. As the distance from the interaction point increases, the hit rate density in the tracking detector decreases, allowing the use of silicon strips instead of pixels beyond a certain distance. Covering the same longitudinal range as the pixel detector, it extends to $|\eta| < 2.5$. Similar to the pixel detector, it has barrel and endcap components, with the barrel further divided into inner and outer parts.

The tracker inner barrel (TIB) and inner disks (TID) consist of four layers in the central section and three disks in each endcap, reaching distances of up to 55 cm from the interaction

point. The TIB employs strips around 117 mm long with a pitch ranging from 80 to 120 μm, while the TID uses strips with a pitch of 100 to 141 μm. These layers provide up to four position measurements along the path of a particle, offering a resolution from 13 to 38 μm, decreasing with larger strip pitches.

The tracker outer barrel (TOB) comprises six layers of larger strips, spanning up to 116 cm from the interaction point and covering $\pm$118 cm longitudinally. These strips have a pitch of 122 to 180 μm and a length of 183 mm. TOB provides six (r, ϕ) measurements for each particle, resulting in a resolution between approximately 18 and 47 μm.

The tracker endcaps (TEC) extend to the forward regions at $124 < |z| < 282$ cm and radial distances from 22.5 to 113.5 cm. Each endcap comprises nine disks with concentric rings of radial silicon strips. The strips in TEC have pitches ranging from 97 to 184 μm and lengths varying from 85 to 200 mm. TEC provides up to nine (z, ϕ) measurements for each particle, offering a resolution similar to TOB [78, 88]. The first two layers of TIB and TOB, along with rings one, two, and three of TEC, incorporate double-sided strip modules [78]. In this arrangement, the second module is positioned at an angle relative to the first, allowing measurement of the z (r) coordinate in the barrel (disks).

In the central area (barrel) of the detector, silicon strips run parallel to the beam axis, capturing the r and ϕ coordinates of particles. The endcaps feature rings of strips arranged radially, enabling measurement of the ϕ and z coordinates for particles. The strip modules partially overlap, and the gap between them, known as the "pitch", is always 25% of the strip width. The tracker achieves a 1% resolution for $p_T < 20$ GeV when measuring the transverse momentum (p_T) of charged hadrons at normal incidence. As p_T increases, the relative resolution worsens, eventually reaching the calorimeter energy resolution for track momenta in the several hundred GeV range.

2.2.4 Electromagnetic calorimeter (ECAL)

The electromagnetic calorimeter (ECAL) surrounds the tracking detector and is primarily designed to accurately measure the energy of photons or electrons produced in a collision. Within CMS, electromagnetic calorimetry consists of two main subsystems: the primary ECAL and the preshower detector.

Primary electromagnetic calorimeter

The ECAL is a homogeneous calorimeter made of lead tungstate ($PbWO_4$) crystals serving as both absorber and scintillator. It is divided into the electromagnetic barrel (EB) and the electromagnetic endcap (EE). The pseudorapidity range covered is $|\eta| < 1.479$ for EB and $1.479 < |\eta| < 3.0$ for EE.

As energetic electrons pass through the ECAL, they emit bremsstrahlung photons, and photons transform into electron-positron pairs when interacting with the ECAL material. These produced photons and electron-positron pairs keep interacting with the calorimeter until their energy depletes, transitioning to ionization as the main means of energy loss in this regime. The net result of these interactions is a nearly instantaneous cascade of high-energy particles, called an electromagnetic shower [78]. Numerous photons are produced at wavelengths at which the scintillator material is transparent. These photons can be picked up by a photodetector attached to the crystal, whose response can be calibrated to provide an accurate estimate of the energy of the incoming particle that sets off the cascade. There are two material properties of particular importance in calorimetry:

- The Molière radius of a given material quantifies the transverse size of an electromagnetic shower in that material. This is the diameter of an imaginary transverse cylinder that contains 90% of the shower. In a calorimetric application, a lower Molière radius allows for better position resolution.

- The radiation length is the characteristic distance over which an incoming particle depletes $(1-\frac{1}{e})$ of its energy. In contrast to the Molière radius, which quantifies the lateral size of a shower, the radiation length can be used to determine how quickly an incoming particle loses energy as a function of longitudinal depth.

The crystals in the ECAL have lengths of 23 cm in the EB and 22 cm in the EE, corresponding to 25.8 and 24.7 radiation lengths, respectively. This ensures that over 98% of the energy of electrons and photons up to 1 TeV is contained within the crystals. Approximately one interaction length of crystal material results in about two-thirds of hadrons initiating showers in the ECAL before reaching the HCAL. The transverse dimension of the crystals aligns with the small Molière radius of $PbWO_4$, which is 2.2 cm. Specifically, in the EB, the front face of the barrel crystals measures $2.2 \times 2.2\,\text{cm}^2$, corresponding to 0.0174×0.0174 in the (η, ϕ) plane. In the endcaps, the crystals are arranged in a grid shape (x, y) with a frontal area measuring $2.9 \times 2.9\,\text{cm}^2$. The small Molière radius of material, indicating its tendency to produce collimated electromagnetic showers, enables high granularity. Additionally, $PbWO_4$ has high density and a short radiation length of 0.89 cm, allowing the construction of a compact calorimeter capable of containing high-energy electromagnetic showers. The crystals exhibit an appropriate response time, designed to separate hits from different bunch crossings due to a 25 ns delay between collisions at LHC. Consequently, about 80% of the scintillation occurs within 25 ns. To detect the emitted scintillation light, the scintillating crystals have photodetectors affixed to their backs. This light, emitted in the visible spectrum, is detected by vacuum phototriodes [78] in the EE and avalanche photodiodes in the EB.

Preshower

A more finely-grained detector, referred to as a preshower, is positioned in front of every endcap disk within the pseudorapidity range of $1.653 < |\eta| < 2.6$. It has two layers,

each comprising a lead radiator and a set of silicon strip sensors. These lead radiators, with lengths corresponding to about two and one radiation lengths, trigger electromagnetic showers when photons or electrons pass through. The silicon sensors, featuring perpendicular strips spaced 1.9 mm apart, detect the shape and energy distribution of these showers. The precision of this detector, coupled with the compact size of the initial shower, ensures precise measurement of the shower position.

The ECAL preshower absorbs approximately 5% of the total energy deposited by an electromagnetic particle in the endcaps. Its main purpose is to achieve exceptional spatial resolution in the endcaps, crucial for distinguishing boosted $\pi^0 \rightarrow \gamma\gamma$ decays from high-energy photons, preventing misidentifications. Additionally, the preshower enhances positional accuracy for both electrons and photons, aiding in distinguishing electrons from particles with minimal ionization. The exceptional energy precision of the ECAL enables accurate measurement of the H boson mass in its decay to photons ($H \rightarrow \gamma\gamma$).

The approximate resolution of the ECAL is given by

$$(\frac{\sigma}{E})^2 = (\frac{2.8(5)\%}{\sqrt{E}})^2 + (\frac{0.12(0.6)\%}{E})^2 + (0.30\%), \tag{2.4}$$

where E is the particle energy in GeV, and the first numerical values correspond to the EB, while the values in brackets refer to the EE. The first term describes the stochastic fluctuation in the number of secondary particles within a shower. The second term is the electronic noise term, while the third one comes from calibration errors and energy leakage.

2.2.5 Hadron calorimeter (HCAL)

The hadronic calorimeter (HCAL) is positioned between the ECAL and the magnet within the detector setup. The main goal of the HCAL is to halt high-energy hadrons and quantify their energy, a critical step for precisely reconstructing hadronic jets and ensuring detector hermeticity. This hermetic structure is essential for computing p_T^{miss}, which is vital for

determining the momentum carried away by weakly interacting particles. The HCAL is structured into four main components: HCAL Barrel (HB), HCAL Endcaps (HE), Forward HCAL (HF), and Outer HCAL (HO). Each of these components is described in detail below.

The HB and HE are sampling calorimeters. The sampling calorimeter is made out of alternating layers of absorber and scintillator. The absorber dissipates the energy of the particle, and the scintillator measures how much energy the particle has as a function of travel depth. Particles with different energies have different profiles for the energy dissipated as a function of depth, so that a combined readout at multiple depths is sufficient to reconstruct the energy of the original particle. All scintillator layers in HCAL are plastic scintillators and embedded optical fibers convey scintillation signals outside the detector where it is picked up by a hybrid photodiode (HPD).

HCAL barrel (HB)

The HB is composed of 16 layers of absorbing plates and 17 layers of scintillator tiles covering $|\eta| < 1.3$. Its radius ranges from the outside surface of the ECAL barrel to the inside surface of the CMS magnetic coil: 1.77 m < R < 2.95 m, which is only enough to cover 5.82 interaction lengths for a particle emitted perpendicular to the beam.

The absorber layers are primarily constructed from brass, with the exception of the first and last layers, which are made from stainless steel to provide structural support. These layers are divided into tiles, each covering an area of $\Delta\eta \times \Delta\phi = 0.087 \times 0.087$, which is approximately 25 times the area covered by a single crystal in the ECAL barrel.

HCAL endcaps (HE)

The HE cap off HB on both sides and covers the range $1.3 < |\eta| < 3.0$. The thickness is about 10 interaction lengths, made up of 17 absorber and 18 scintillator layers. The segments in these layers are defined with a size of $\Delta\eta \times \Delta\phi = 0.087 \times 0.087$ for $1.3 < |\eta| < 1.6$, and

for $|\eta| > 1.6$, the segmentation is $\Delta\eta \times \Delta\phi = 0.17 \times 0.17$. The absorber layers in the HE are also constructed using brass. Brass is ideal as an absorber for both HB and HE because of its nonmagnetic characteristics, useful in a region with a high magnetic field.

Outer calorimeter (HO)

The combination of the HB and EB in the central region lacks sufficient stopping power to completely contain hadronic showers produced by high-energy jets. The HO subdetector is added to capture the escaping energy tails from these showers. The HO is located outside the solenoid magnet and has a 19.5-cm-thick iron absorber combined with two layers of plastic scintillator tiles. It is used to increase the nuclear absorption length in the central region and to measure the tails of high-energy or late-developing hadronic showers. Upon integrating the HO subdetector, the overall calorimeter achieves a depth of 11.8 λ_I, enhancing its effectiveness, particularly at the boundary between the barrel and endcaps.

Forward calorimeter (HF)

In many physics analyses, the total missing p_T^{miss} plays a crucial role, and it needs to be measured as accurately as possible. If only hadronic jets up to η = 3.0 are reconstructed (from HB, HE, and HO), which leaves open the possibility that a high-energy jet was emitted in the collision at higher η but simply missed the detector acceptance. Practically, this would lead to a high uncertainty on p_T^{miss} for each collision. To reduce the effect of this issue as far as possible, the fourth component of the hadronic calorimeter, the HF, covers the range 3.0 < $|\eta|$ < 5.2. The key challenge in this operating environment is the extreme radiation; accordingly, the design is kept as simple and radiation-hard as possible. It is made of Cherenkov radiating quartz fibers as an active material, radiation-hard steel as absorbers, and photo-multipliers to collect light.

2.2.6 Muon detector

Muons play a crucial role in the CMS physics program, evident from its inclusion in the CMS name. The identification of muons is achieved with notable efficiency and precision, allowing for the accurate measurement of their momentum. MMuons serve as a valuable tool for identifying various physics phenomena, including the H boson, top quarks, supersymmetric particles, and more.

The muon system serves as the outermost layer of the CMS detector, positioned outside the solenoid magnet. The arrangement of the four muon detector planes is interleaved with the magnetic flux-return iron yoke, generating a magnetic field of up to 2 T. Its cylindrical structure, comprising a central barrel and two endcaps, is designed in alignment with the solenoid. The significant amount of material preceding and surrounding the muon system makes it rare for hadrons to penetrate through, ensuring highly effective muon identification. Additionally, the powerful CMS magnet contributes to exceptional momentum resolution for muons. The muon chamber employs three kinds of gaseous detectors: cathode strip chambers (CSC), drift tubes (DT), and resistive plate chambers (RPC). To achieve good muon identification and energy reconstruction, readouts from the inner tracker are combined with those from three muon subdetectors. Because muons are much heavier than electrons, they only lose a small fraction of their energy as they interact with the ECAL and HCAL, and return yoke material. Instead of producing a shower, they leave a trail of ionized particles and punch through the whole detector. Each of the three muon subdetectors is covered below.

Drift tubes

The barrel section of the muon system employs DT chambers and spans the region with a pseudorapidity of $|\eta| < 1.2$. In general, a DT works on the following principle: a wire at high positive voltage acts as an anode. The wire is surrounded by a mixture of 85%

Ar and 15% CO_2 gas. When a muon passes through the gas, it ionizes its atoms creating some free electrons and positive ions. These electrons start drifting toward the wire, and as they accelerate, they in turn ionize other atoms in their path, amplifying the number of free electrons that eventually reach the wire. The time taken by the electromagnetic cascade to reach the anode can be used to reconstruct the perpendicular distance of the muon track from the wire. Muon positions are determined where they intersect with wires, providing two-dimensional measurements along their paths. In DTs, the electron drift time can reach 400 ns, longer than LHC bunch crossings. DTs are suited for the barrel region due to lower muon and background rates, uniform magnetic field, and extended drift time. The barrel region of the muon system includes four wheels, each featuring four chambers. Within these chambers, there are three superlayers containing parallel wires, allowing for precise measurements in both (r, ϕ) and (r, z) coordinates. The accuracy of hits varies from 250 to 600 μm in (r, z) [88] and approximately 250 μm in (r, ϕ).

Cathode strip chambers

The region 0.9 < $|\eta|$ < 2.4 of the muon system is instrumented with CSCs. These CSCs consist of cathode strips carrying positive charges, extending radially outward, and nearly perpendicular anode wires, both within a gas-filled volume. For the CMS CSCs, the gas used is a mixture of 40% Ar, 50% CO2, and 10% CF4. Cathode Strip Chambers (CSCs) detect muon positions in the (r, z) plane when muons dislodge electrons from gas atoms. Electrons move toward the anode, causing an electron avalanche. Positive ions migrate to cathode strips, offering (r, ϕ) measurements. CSCs have short drift paths, ensuring rapid response and accurate segmentation. They suit high pseudorapidities with high muon and background rates and handle nonuniform magnetic fields. Each endcap has four stations with trapezoidal CSC chambers. Each chamber has six layers for precise two-dimensional muon position measurements in the (r, ϕ) plane. CSCs provide accurate p_T determination

with a resolution of about 150 μm along ϕ.

Resistive plate chambers

In order to accurately match muons with the correct bunch crossing at the high luminosities of the LHC, a specialized triggering detector composed of RPCs is implemented. In addition to the DTs and CSCs, both the barrel and a section of the endcaps are equipped with RPCs. The fundamental element of this design is a set of two parallel plates made with a highly resistive material, with the space between the plates occupied by a gas. In CMS, the plates in the RPCs are made of 2 mm thick bakelite, the gap between the plates is 2 mm, and the gas between the plates is primarily $C_2H_2F_4$. The plates are maintained at a voltage difference just below the breakdown voltage. The barrel RPC modules are inserted into the DT stations. There are six barrel layers: two each in the first two inner stations, and one each in the two outer stations. Along ϕ, the modules have the same segmentation as DT modules. There are three endcap layers on each side, divided into three annular layers; along ϕ, these are also segmented in trapezoidal sections just like the CSCs and have the same $\triangle\phi$ segmentation as the barrel modules.

When a muon enters the space between the plates in an RPC, it ionizes the gas, triggering an electron avalanche. Due to the higher applied voltage, this avalanche reaches the detecting strips between the plates much faster. In CMS, RPCs have two gas gaps with readout strips placed between them. They offer a time resolution of approximately 1 ns, which is significantly shorter than the time between bunch crossings. However, their spatial resolution, around 1 cm, is lower compared to DTs and CSCs. DTs and CSCs are designed to provide highly accurate information on the full trajectory of a muon. However, because the delay between the passage of a muon and the avalanche reaching the anode or cathode could be more than 25 ns (the time between two consecutive bunch crossings), there is some ambiguity in the bunch crossing corresponding to the production of a given muon. This would

make operating at high trigger rates very challenging. The RPC design features excellent timing resolution, and, by removing the ambiguity on bunch crossing, allows operation at very high trigger rates.

2.2.7 Detector simulation

Comprehensive simulation of proton-proton collision events is crucial for understanding actual outcomes detected by the CMS detector and for developing effective analyses. To achieve this, a Geant4 [89] model of the CMS detector is employed. Geant4 enables the construction of complex geometric models with various materials, prediction of particle interactions within detector materials, modeling of external electromagnetic fields' impact, and simulation of detector readout. Initially, collision events are simulated as described in Section 2.1.4. The generated particles then undergo Geant4 simulation within the CMS detector, producing signals similar to actual collision data. These simulated signals are analyzed using the same algorithms and software as real data, making Geant4 simulation a crucial component in all simulated collision events discussed in this thesis.

2.2.8 Trigger system and data acquisition

The LHC collides proton bunches at a rate of approximately 4×10^7 Hz, but only a fraction is relevant for CMS physics. To identify these important events, a two-step trigger system [78] is utilized. Initially, the Level-1 (L1) trigger system rapidly reduces the event rate to 10^5 Hz. This system, comprising specialized hardware processors, makes fast decisions. Events approved by the L1 trigger are then transmitted to the High-Level Trigger (HLT). Operating on a computer farm, the HLT further reduces the event rate from approximately 10^5 Hz to about 10^3 [90, 91] Hz before storing the data for subsequent offline analysis

L1 trigger

CMS uses the L1 trigger system based on FPGAs (Field Programming Gate Arrays) and ASICs (Application Specific Circuits). Several L1 trigger algorithms, each called a "seed", target different physical scenarios. The L1 trigger system detects events containing electrons, photons, muons, and hadronic jets by considering their p_T and $|\eta|$ values. It also chooses events having substantial total transverse momentum (sum of particle momenta) or missing transverse momentum (p_T^{miss}). Certain event seeds are "prescaled", indicating that only one event out of every N event meeting the criteria is accepted, with N representing the prescale factor [91].

The L1 trigger system can be split into three successive steps: local, regional, and global. The calorimeter trigger obtains information from the ECAL and HCAL and locally constructs primitives from energy deposits. After this, at the regional level, it combines these primitives and constructs simplified objects, like jets, electrons, etc. Finally, it calculates the high-level variables at the global level such as total missing transverse energy. The muon trigger gets information from the muon system about the track segments, hit patterns, and reconstructed tracks at the regional level and combines all this information into a simplified muon identification at the global level. Information from both, the muon and calorimeter trigger is used to make the decision about accepting an event or not. The data from each bunch crossing is saved temporarily by each subdetector in a buffer. If an L1 accept signal is sent to the subdetectors for a given bunch crossing, each of them sends subdetector information via a data acquisition system to the next filtering step – the HLT.

High level trigger

The HLT is entirely a software-based system with more than 10,000 CPU cores and is located on-site. It can access the readouts from all subdetectors at their full resolution, including those of the tracking detector. The HLT takes data from every collision that passes

the L1 trigger and performs an event reconstruction based on the full detector information. There are more than 400 different filters that select for a broad spectrum of interesting physics signatures; each such filter is called a "trigger path". Each trigger path is an ordered set of processing steps that reconstruct and select particles. After meeting the criteria outlined in an HLT path, an event is permanently saved and processed for further physics analysis [78, 90].

2.2.9 Computing and software

The CMS experiment uses a so-called CMS software (CMSSW) [92] framework with a modular architecture. The CMSSW framework offers essential services for simulation, calibration, alignment, and reconstruction modules to process event data for analysis purposes. The CMSSW framework works with the different data formats and transforms one into another. GEN is the Monte Carlo simulated data format containing generator-level events before detector simulation. The RAW data includes detector information, L1 trigger outcomes, HLT selection results, and some higher-level objects generated during HLT processing. RECO data also stores the reconstructed object information. AOD is the reduced RECO format, which includes information important for physics analysis. MINIAOD [93] and NANOAOD are even more reduced data formats for faster event processing.

2.2.10 Reconstruction of the particle flow elements

The identification and reconstruction sequence within each PF block follows this specific order. It begins with detecting and reconstructing muon candidates, which leads to the removal of corresponding PF elements (tracks and clusters) from the PF block.

In the PF algorithm [86], muon identification involves applying specific criteria related to the global and tracker muon properties. Initially, isolated global muons are chosen by considering inner tracks and calorimeter energy deposits within a distance $\triangle$R to the muon

direction in the (η, ϕ) plane that is less than 0.3. Next in the process, electron identification and reconstruction are carried out to capture the energy from all bremsstrahlung photons. This step involves identifying energetic and isolated photons, whether they are converted or unconverted. Tracks and clusters from the ECAL or preshower associated with these electrons are excluded from further analysis. Electron reconstruction utilizes combined information from both the inner tracker and the calorimeters. Due to the extensive material present in the tracker, electrons often emit bremsstrahlung photons, and photons frequently convert into e^+e^- pairs, leading to a cascade of bremsstrahlung emissions. Consequently, the fundamental characteristics and technical challenges related to tracking and energy deposition patterns for electrons and photons are similar. Hence, the reconstruction of isolated photons is performed alongside electron reconstruction. All tracks and clusters in the PF block designated for electron and photon reconstruction are marked and excluded from further processing. The remaining elements in the block are cross-identified, including charged hadrons ($\pi^{\pm}$, $K^{\pm}$, or protons), neutral hadrons like K_L^0 or neutrons, and photons, originating from processes such as parton fragmentation, hadronization, and jet decay (e.g., π^0 decays). Within the tracker coverage ($|\eta| < 2.5$), ECAL and HCAL clusters not associated with any tracks are interpreted as photons and neutral hadrons respectively. Beyond the tracker acceptance, ECAL clusters linked to specific HCAL clusters are presumed to originate from the same hadron shower, while unlinked ECAL clusters are categorized as photons. Secondary particles created by hadrons undergoing nuclear interactions in the tracker material are identified and reconstructed. Once the overall event information is available, after processing all blocks and identifying all particles, a post-processing step is performed to revisit the reconstructed event.

Hadronic τ decays

The τ decay results in either a charged lepton (electron or μ) accompanied by two neutrinos or a few hadrons and one neutrino. Hadronic τ decays, referred to as τ_h decays, can be distinguished from quark and gluon jets based on criteria such as multiplicity, collimation, and isolation of the decay products. The particles forming the jet are grouped into τ_h candidates corresponding to one of the primary τ decay modes: $\tau^- \to h^-\nu_\tau$, $\tau^- \to h^-\pi^0\nu_\tau$, $\tau^- \to h^-\pi^0\pi^0\nu_\tau$, $\tau^- \to h^-h^+h^-\nu_\tau$. Due to the substantial material in the inner tracker, photons from π^0 decay often convert before reaching the ECAL. Neutral pions are thus identified by collecting reconstructed photons and electrons within a narrow window of size 0.05 $\times$ 0.20 in the (η, ϕ) plane. Each τ_h candidate is then required to have a mass consistent with its decay mode and carry a unit charge.

Primary vertices

During data collection period, an average of around 20 additional interactions, known as pileup, occurred for each bunch crossing. These interactions were spread along the beam axis in the CMS coordinate system, forming a normal distribution with a standard deviation of approximately 5 cm. Determining the number of pileup interactions could be done either by counting interaction vertices (N_{vtx}) reconstructed through charged-particle tracks, considering a vertex reconstruction efficiency of about 70% for pileup interactions, or by evaluating the instantaneous luminosity of the specific bunch crossing using dedicated detectors and, with additional data, the proton-proton inelastic cross-section [94]. This led to an extra transverse momentum (p_T) averaging about 1 GeV per pileup interaction per unit area in the (η, ϕ) plane. Pileup interactions, including those from different bunch crossings, could directly affect the energy measurements in the calorimeters, which serve as input for particle reconstruction. The primary vertices, located at different points along the beam axis, were ranked based on the quadratic sum of the transverse momenta of their constituent

tracks, denoted as $\sum p_T^2$. The primary vertex with the highest $\sum p_T^2$ was identified as the hard-scatter vertex, while the remaining vertices were categorized as pileup vertices.

Chapter 3

SUSY search in jets and missing transverse momentum final state

3.1 Introduction

The analysis targets several signal models that primarily vary in the number of jets and b-tagged jets generated during the decay of gluinos and/or squarks. For gluino pair production, the T1tttt, T1bbbb, T1qqqq, and T5qqqqVV [95] simplified models spectra (SMS) SUSY scenarios are considered, as illustrated in Fig. 3.1. The T1bbbb and T1qqqq models are similar to the T1tttt model, except that the top quark-antiquark ($t\bar{t}$) system is substituted with bottom quark-antiquark ($b\bar{b}$) or light-flavored (u, d, s, c) quark-antiquark ($q\bar{q}$) pairs, respectively. In the T5qqqqVV scenario, every gluino undergoes decay into a pair

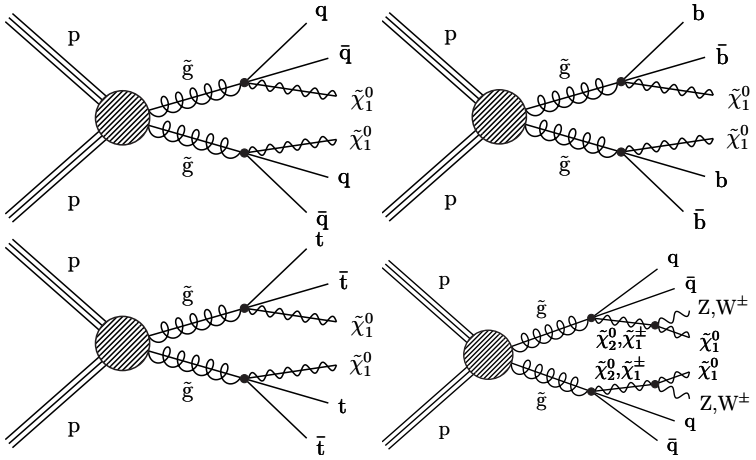

Figure 3.1: Diagrams depicting the events for the direct gluino production scenarios examined in this search: the (top left) T1qqqq, (top right) T1bbbb, (bottom left) T1tttt, (bottom right) T5qqqqVV, SMS scenarios, with $\tilde{\chi}_1^0$ the lightest neutralino, taken to be a weakly interacting LSP [11].

of light-flavored quarks ($q\bar{q}$), and either the next-to-lightest neutralino, $\tilde{\chi}_2^0$, or the lightest

chargino, $\tilde{\chi}_1^{\pm}$. The probability of decay into each channel, $\tilde{\chi}_2^0$, $\tilde{\chi}_1^+$, or $\tilde{\chi}_1^-$, is 1/3. The subsequent decays of $\tilde{\chi}_2^0$ ($\tilde{\chi}_1^{\pm}$) result in the production of the lightest neutralino, $\tilde{\chi}_1^0$, and an on- or off-mass-shell Z (W) boson. In this model, the masses are assigned such that $m_{\tilde{\chi}_1^{\pm}} = m_{\tilde{\chi}_2^0} = 0.5(m_{\tilde{\chi}_1^0} + m_{\tilde{g}})$.

Three simplified models, namely T2tt, T2bb, and T2qq (illustrated in Fig. 3.2), are explored for squark-antisquark production. In the T2tt scenario, top squark-antisquark pairs are produced, and the squark (or antisquark) subsequently decays into a top quark (or antitop quark), and the lightest neutralino, $\tilde{\chi}_1^0$. The T2bb and T2qq models are similar to T2tt, except that they involve bottom squarks and quarks, or light-flavored squarks and quarks, respectively, replacing the top squarks and quarks.

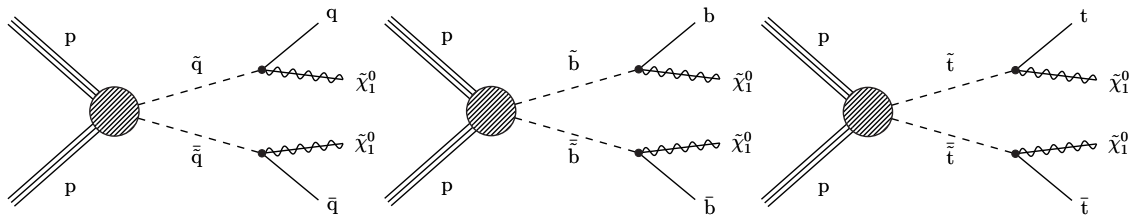

Figure 3.2: From left to right, diagrams representing the events of direct squark production scenarios targeted in this search: T2qq, T2bb, and T2tt SMS scenarios. Here, $\tilde{\chi}_1^0$ is the lightest neutralino, assumed to be a weakly interacting LSP [11]

The high expected production rates of gluinos and squarks, make them the main focus in the search for SUSY at the LHC. After these particles are produced, they usually decay into jets, leptons, and significant missing transverse momentum. This study is distinct from those specifically looking for leptons and contributes to an independent set of SUSY searches within CMS. Signatures of SUSY in final states characterized by multiple jets and missing transverse momentum have been extensively investigated by both the ATLAS and CMS collaborations [96, 97, 98, 99]. In a previous study conducted by the CMS collaboration [96], squarks with masses up to 960 GeV (for the T2tt model), 990 GeV (for the T2bb model), and 1390 GeV (for the T2qq model) have been excluded. Additionally, gluinos

with masses up to 1960 GeV (for the T1tttt model), 1950 GeV (for the T1bbbb model), 1825 GeV (for the T1qqqq model), and 1800 GeV (for the T5qqqqVV model) have been excluded. A similar study conducted by the ATLAS collaboration [99] reveals that, in a simplified model featuring only gluinos with a massless lightest neutralino, gluino masses below 2.3 TeV are excluded. Moreover, in a simplified model involving the strong production of the first and second generations of squarks, with decay to a massless lightest neutralino, squark masses below 1.85 TeV are excluded, assuming mass-degenerate squarks of the first two generations.

3.2 Datasets and triggers

Datasets

The datasets collected during 2016, 2017, and 2018 with the CMS detector were analyzed for this analysis. The dataset used in this study corresponds to a total integrated luminosity of 137.2 fb^{-1} from proton-proton collisions at a center-of-mass energy of 13 TeV. For the year 2016, `17Jul2018 re-reco` version of the data was used, and similarly, `31Mar2018 re-reco` version of data was utilized for 2017. For 2018, the `17Sep2018 re-reco`, `22Jan2019 re-prompt reco`, and `prompt reco` versions of data were used for different periods. Various versions of CMS software (CMSSW) were employed to handle the MC samples for the SM. The 2016 samples were primarily reconstructed using CMSSW version 9_4_X (RunIISummer16MiniAODv3). The MC samples from 2017 were reconstructed using CMSSW 9_4_X (RunIIFall17MiniAODv2) release, whereas the 2018 MC samples were reconstructed with CMSSW 10_2_X release.

Triggers

Triggers [100, 101] play a crucial role in retaining a selected portion of data events that hold significance for physics analysis. A set of MET ($p_{\mathrm{T}}^{\mathrm{miss}}$) × MHT ($H_{\mathrm{T}}^{\mathrm{miss}}$) triggers are used for event selection from data in the signal region, indicated by the specified HLT paths below:

- `HLT_PFMETX_PFMHTX_IDTight_v* (X=90,100,110,120,130,140)`,
- `HLT_PFMETNoMuX_PFMHTNoMuX_IDTight_v* (X=90,100,110,120,130,140)`,
- `HLT_PFMETX_PFMHTX_IDTight_PFHT60_v* (X=100,110,120,130,140)`,
- `HLT_PFMETNoMuX_PFMHTNoMuX_IDTight_PFHT60_v* (X=100,110,120,130,140)`

Here, `X` signifies the threshold imposed on the online $p_{\mathrm{T}}^{\mathrm{miss}}$ and $H_{\mathrm{T}}^{\mathrm{miss}}$, computed via the PF algorithm; the asterisks denote the possibility of multiple versions of the same trigger being employed. The selection of events during the three-year data collection period was based on a logical OR combination of all the specified trigger paths. The same set of triggers was also used for selecting events in the single-electron control region (CR), single-muon CR, and the QCD-validation region. In 2016, events in a single-photon CR were collected using the `HLT_Photon175` trigger, which had a threshold of 175 GeV for the photon p_{T}. In 2017 and 2018, the `HLT_Photon200` trigger was used, which required a photon p_{T} threshold of 200 GeV. The details of the CMS trigger study and the CMS trigger naming scheme can be found in [102, 103, 104].

3.3 Object definitions, search variables, event selection

The search regions for the analysis require large $H_{\mathrm{T}}^{\mathrm{miss}}$, large H_{T}, a large number of jets N_{jet}, and no leptons. To maximize sensitivity to the diverse topologies, a loose baseline selection is initially applied in $H_{\mathrm{T}}^{\mathrm{miss}}$, H_{T}, and N_{jet}. In this study, jets were reconstructed

from PF candidates utilizing the anti-k_T algorithm [105] with a size parameter of 0.4. The baseline selection is defined by the following criteria:

- $N_{\text{jet}} \geq 2$: All events must have at least two "good" jets with a p_{T} greater than 30 GeV, $|\eta|$ less than 2.4, and meet specific jet identification criteria.

- $H_{\text{T}} > 300$ GeV: Here, H_{T} represents the total transverse momentum in the event, calculated as the sum of the transverse momenta ($\vec{p}_T$) of all selected jets that satisfy the specified criteria mentioned above.

- $H_{\text{T}}^{\text{miss}} > 300$ GeV: In this case, $H_{\text{T}}^{\text{miss}}$ represents the absolute value of the negative vectorial sum of the $\vec{p}_T$ for all the jets in the event where the jets must meet the criteria above.

- **Muon veto:**

  Muon candidates are chosen based on the "Medium Muon" selection [106, 107] recommended by the muon physics object group [108], with the requirement to have $p_{\text{T}} > 10$ GeV, $|\eta| < 2.4$, and an isolation requirement, $I_{\text{mini}} < 0.2$, where I_{mini} is the mini-isolation variable is defined below. Any event containing a muon meeting the above-mentioned criteria is rejected.

  In the process of top decay, the distance between the lepton and b-jet decreases as the transverse momentum (p_T) of the top-jet increases. This suggests using a cone size that scales inversely with the top-jet p_T. Alternatively, the p_T of the lepton itself can be utilized as a rough indicator. This approach proves to be more effective in discriminating, as it also serves as a constraint on the hardness of the lepton. Softer leptons necessitate larger isolation cones, making isolation more challenging. A suitable cone size of $R_{\text{iso}} = \frac{15\,\text{GeV}}{p_{T_\ell}}$ is determined, which is adopted as the standard cone definition. Based on this, the mini-isolation variable (I_{mini}) [109] is defined as the

ratio of the p_T of the lepton to the scalar sum of p_T of all charged particles within the cone R_{iso}, each with $p_T > 1$ GeV, including the lepton. This variable works well in identifying isolated leptons in scenarios featuring substantial hadronic activity or boosted regimes but still performs well in cleaner environments.

- **Electron veto:**

  Electron candidates are chosen based on the "cut-based veto" selection [110] recommended by the electron and photon physics object group [108]. Electron candidates are required to have $p_{\text{T}} > 10$ GeV, $|\eta| < 2.5$, and $I_{\text{mini}} < 0.1$. Any event containing an electron meeting the criteria above is rejected.

- **Photon veto:**

  Well-identified and isolated photon candidates with $p_{\text{T}} > 100$ GeV are selected in the barrel ($|\eta| < 1.4442$) or the endcap ($1.566 < |\eta| < 2.5$) region. The requirements for barrel (endcap) photons in 2016 include $H/E < 0.0597$ (0.0481), $\sigma_{i\eta i\eta} < 0.01031$ (0.03013), neutral hadron isolation $< 10.910 + 0.0148p_{\text{T}} + 0.000017p_{\text{T}}^2$ $(5.931 + 0.0163p_{\text{T}} + 0.000014p_{\text{T}}^2)$, charged hadron isolation ($\text{Iso}_{\text{h}^\pm}$) < 1.295 (1.011), and electromagnetic particle isolation $< 3.630 + 0.0047p_{\text{T}}$ $(6.641 + 0.0034p_{\text{T}})$. For 2017 and 2018, the requirements for barrel (endcap) photons are $H/E < 0.04596$ (0.0590), $\sigma_{i\eta i\eta} < 0.0106$ (0.0272), neutral hadron isolation $< 24.032 + 0.01512p_{\text{T}} + 0.00002259p_{\text{T}}^2$ $(19.722 + 0.0117p_{\text{T}} + 0.000023p_{\text{T}}^2)$, charged hadron isolation < 1.694 (2.089), and electromagnetic particle isolation $< 2.876 + 0.004017p_{\text{T}}$ $(4.162 + 0.0037p_{\text{T}})$. The isolation requirements are on the energy within a cone of radius, $\Delta R < 0.3$ around the direction of photon momentum. Photon candidates are further required to have no associated tracks in the pixel detector. Events with a photon satisfying these criteria are rejected.

- **Isolated track vetoes:**

  Events containing one or more isolated charged tracks are rejected to minimize backgrounds from unidentified electrons, muons, and hadronic τ decays.

- **Angular cut:**

  The majority of QCD multijet events in the search region have jets with under-measured momenta, resulting in an artificial momentum imbalance. A signature of such events is a jet aligned closely with the $H_{\mathrm{T}}^{\mathrm{miss}}$ vector direction. To reduce this background, events are excluded if the two highest-p_{T} jets are located within 0.5 radians of the $H_{\mathrm{T}}^{\mathrm{miss}}$ vector in the azimuthal coordinate:

  $$\Delta\phi(j_1,\ H_{\mathrm{T}}^{\mathrm{miss}}) > 0.5 \text{ and } \Delta\phi(j_2,\ H_{\mathrm{T}}^{\mathrm{miss}}) > 0.5 \tag{3.1}$$

  This condition is loosened for the third- and fourth-highest-p_{T} jets:

  $$\Delta\phi(j_3,\ H_{\mathrm{T}}^{\mathrm{miss}}) > 0.3 \text{ and } \Delta\phi(j_4,\ H_{\mathrm{T}}^{\mathrm{miss}}) > 0.3 \tag{3.2}$$

- **Event cleaning:**

  Events containing jets that have $p_{\mathrm{T}} > 30$ GeV and $\eta < 5$ but fail the loose jet identification criteria are rejected. Additionally, event filters are employed to discard events with spurious $E_{\mathrm{T}}^{\mathrm{miss}}$ signals.

- **Corrections:**

  The "ECAL Level1 pre-firing issue" [111] causes events with high p_{T} forward objects to suffer from a reduced trigger efficiency. The MC is corrected based on the pre-firing inefficiency to account for this effect in the data.

  In the 2018 data, starting with Run 319077 (just before the 2018C data-taking period), one sector of the minus side of the Hadronic endcap was disabled unexpectedly. This is often described as the "HEM problem". The unmodified PF algorithm [86] may

generate additional jets and/or electrons in the disabled sector, because there may be energy measured in ECAL without any corresponding energy measured in HCAL. To improve the agreement between data and MC, events in both MC and data having any activity in that region are vetoed. A wider veto region is used for jets, with an additional cut to minimize the reduction in signal efficiency.

- **Tagging of b-jets:**

  The count of selected jets $N_{\text{b-jet}}$ satisfying the deep secondary vertex b-tagging algorithm criteria at the medium working point (2016: $\texttt{DeepCSVM} > 0.6324$; 2017/2018: $\texttt{DeepCSVM} > 0.4941$) is used as a discriminating variable [112, 113].

The search variables, including N_{jet}, $N_{\text{b-jet}}$, $H_{\text{T}}^{\text{miss}}$, and H_{T}, are binned as follows: N_{jet} has bins: $2-3$, $4-5$, $6-7$, $8-9$, and ≥ 10; $N_{\text{b-jet}}$ has bins: 0, 1, 2, ≥ 3, and ≥ 2 (only for the 2-3 N_{jet} bin); and $H_{\text{T}}^{\text{miss}}$ and H_{T} are divided into a total of 10 orthogonal 2D intervals, as depicted in Figure 3.3. Search regions where $H_{\text{T}}^{\text{miss}}$ exceeds H_{T} are excluded, as this is not physically feasible. In addition, a low-$H_{\text{T}}^{\text{miss}}$ sideband, $250 < H_{\text{T}}^{\text{miss}} < 300$ GeV is defined for each selected search interval in N_{jet} and $N_{\text{b-jet}}$, shares the same H_{T} boundaries as the bins within $300 < H_{\text{T}}^{\text{miss}} < 350$ GeV. This sideband plays a role in measuring the QCD background.

For $N_{\text{jet}} = 2 - 3$ bin, a special $N_{\text{b-jet}} \geq 2$ bin is created so as not to lose the $N_{\text{b-jet}} = 3$ events. For $N_{\text{jet}} \geq 7$, bins C1, 1, and 4 within the $H_{\text{T}} - H_{\text{T}}^{\text{miss}}$ categorization are omitted due to low population and limited expected signal sensitivity. Consequently, the total number of distinct search bins stands at 174 ($1 \times 3 \times 10 + 2 \times 4 \times 10 + 2 \times 4 \times 8$, where the terms are the number of N_{jet} categories multiplied by the number of $N_{\text{b-jet}}$ bins and the number of $H_{\text{T}} - H_{\text{T}}^{\text{miss}}$ bins for each category, and the categories are $N_{\text{jet}} = 2-3, 4-5, 6-7; 8-9, \geq 10$, respectively).

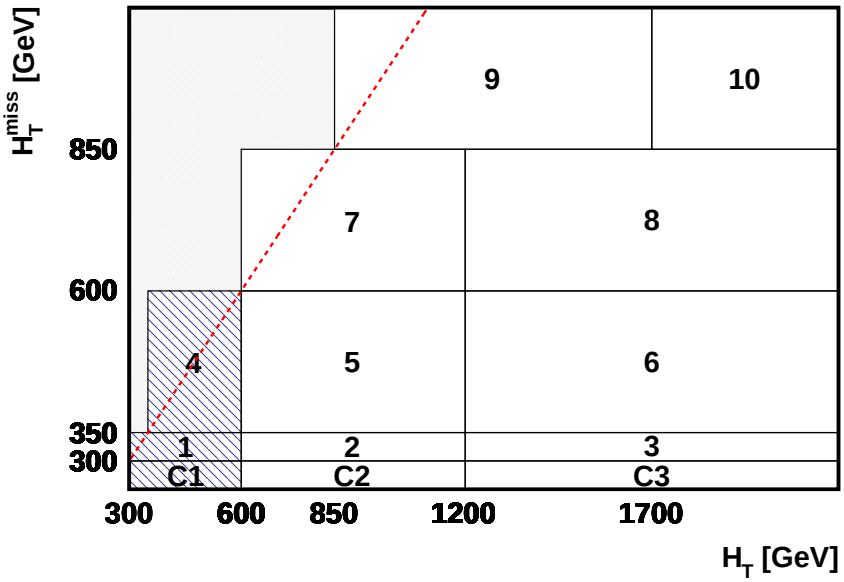

Figure 3.3: A visual representation of the signal and QCD sideband bins in a two-dimensional plane, featuring H_{T} and $H_{\mathrm{T}}^{\mathrm{miss}}$. The same H_{T} and $H_{\mathrm{T}}^{\mathrm{miss}}$ regions are utilized for every N_{jet} and $N_{\mathrm{b-jet}}$ bin, except for the hashed bins, which are excluded when N_{jet} is greater than or equal to 8. The red dashed line indicates the criteria of $H_{\mathrm{T}}^{\mathrm{miss}} \leq H_{\mathrm{T}}$ selection [12].

3.4 SM Backgrounds

The primary background sources originate from several SM processes, including the production of top quarks via either top quark-antiquark ($\mathrm{t\bar{t}}$) pairs or single top quarks, as well as the generation of on- or off-mass-shell W or Z bosons (in W+jets and Z+jets events respectively). Additionally, events with multiple jets resulting from QCD processes contribute to the background. If a W boson decays to a neutrino and an undetected or out-of-acceptance charged lepton, such as a τ lepton with either a leptonic or hadronic decay, both top quark and W+jets events can exhibit significant $H_{\mathrm{T}}^{\mathrm{miss}}$ and hence contribute to the background. These background components are assessed using a control sample involving a single lepton. Likewise, Z+jets events can show noticeable $H_{\mathrm{T}}^{\mathrm{miss}}$ if the Z boson decays

into two neutrinos. To account for this background, a control sample of γ + jets events is utilized, alongside another control sample where a Z boson decays into an e^+e^- or $\mu^+\mu^-$ pair. Significant $H_{\mathrm{T}}^{\mathrm{miss}}$ in QCD multijet events may occur due to jet p_{T} mismeasurements, jets falling outside the selection criteria, or b jets producing one or more neutrinos. The QCD background contribution is assessed using specific control samples in combination with the "rebalance and smear" technique [96].

In each of the 174 analysis bins, the background originating from SM processes is estimated using event counts derived in corresponding control samples from the data, along with correction factors derived from MC simulated event datasets.

3.4.1 Z ($\rightarrow \nu\bar{\nu}$) + jets background

The γ + jets sample is used to determine the yields in the 46 analysis bins corresponding to $N_{\mathrm{b-jet}} = 0$. The $\mathrm{Z} \rightarrow \ell^+\ell^-$ sample is used to establish the systematic uncertainty of the physics modeling of γ+jets for $N_{\mathrm{b-jet}} = 0$ bins. The extrapolation to bins with $N_{\mathrm{b-jet}} > 0$ is performed using the $\mathrm{Z} \rightarrow \ell^+\ell^-$ dataset. This procedure is followed in order to take benefit of both the enhanced statistical accuracy of the γ+jets sample and the more straightforward transfer factors using the $\mathrm{Z} \rightarrow \ell^+\ell^-$ sample. The photon (dilepton) samples require a photon (dilepton) candidate with $p_{\mathrm{T}} > 200$ GeV. The photon or two lepton candidates are removed from the event and the standard jet clustering is redone, resulting in significant $H_{\mathrm{T}}^{\mathrm{miss}}$ in the event. The leptons and photons are identified with the same veto criteria as discussed in section 3.3, except for the increased photon (dilepton) p_{T} threshold.

Categories of photons

In the simulation, photons are classified into different categories based on their origin and characteristics. These categories include "prompt photons" which are photons radiated by either another photon or a quark. Prompt photons are further subdivided into "direct prompt

photons" and "fragmentation prompt photons". Direct prompt photons are those that have a ΔR separation of more than 0.4 to any outgoing quarks or gluons, while fragmentation prompt photons are all other prompt photons that do not meet the criteria for being "direct". The second main category is "non-prompt photons", which includes all photons that do not fall under the prompt category. This often includes photons from the decay of neutral pions or η within jets.

Measurement of Z ($\rightarrow \nu\bar{\nu}$) + jets background for $N_{\mathrm{b-jet}} = 0$

The prediction of the number of Z ($\rightarrow \nu\bar{\nu}$) + jets background events in each of the analysis bins ($N^{\mathrm{pred}}_{Z\rightarrow\nu\nu}$) is calculated using Eq. 3.3. This prediction relies on the number of γ+jets events in the corresponding bin ($N^{\mathrm{obs}}_{\gamma}$), the purity of γ+jets sample (β_{γ}), and the ratio between the numbers of Z($\rightarrow \nu\bar{\nu}$) + jets events and γ+jets events ($\mathcal{R}_{Z(\nu\bar{\nu})/\gamma}$), fraction of prompt photons that are direct ($\mathcal{F}_{\mathrm{dir}}$).

$$N^{\mathrm{pred}}_{Z\rightarrow\nu\nu} = \mathcal{R}_{Z(\nu\bar{\nu})/\gamma} \cdot \mathcal{F}_{\mathrm{dir}} \cdot \beta_{\gamma} \cdot N^{\mathrm{obs}}_{\gamma} \tag{3.3}$$

The following Section describes each component on the right-hand side of Eq. 3.3 and the associated systematic uncertainties for each term.

Number of γ+jets events ($N^{\mathrm{obs}}_{\gamma}$)

The observed photons in the γ + jets control sample come from three sources: direct prompt photons, fragmentation prompt photons, and non-prompt photons. Direct prompt photons are most useful for predicting the Z ($\rightarrow \nu\bar{\nu}$) + jets background because their production processes most neatly map to the Z boson production processes. Any photon in the γ+jets or QCD simulation samples is either non-prompt, direct prompt, or fragmentation prompt.Figure 3.4 illustrates the comparison between γ + jets events observed in data and expected γ + jets events from various simulations in both the barrel and endcap region.

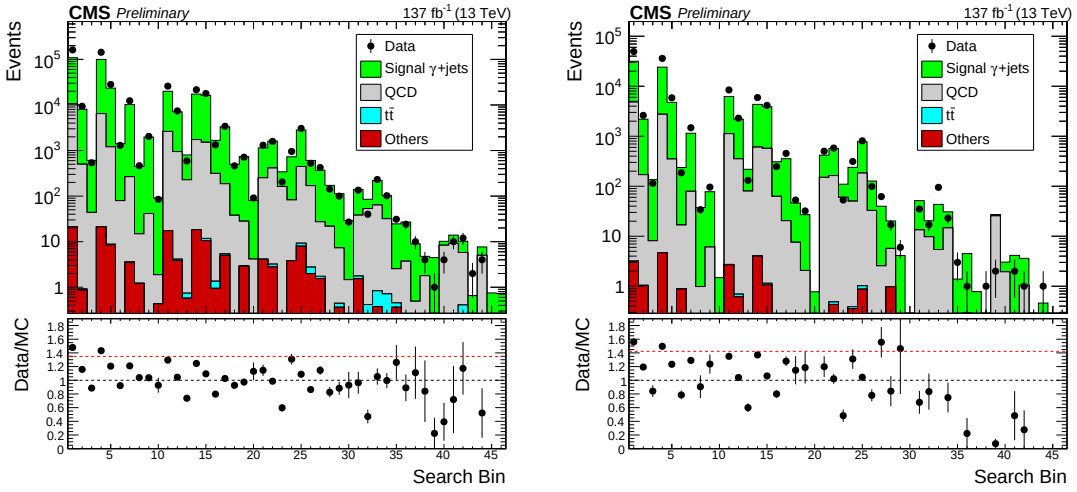

Figure 3.4: Numbers of observed events in the photon control sample compared to simulation for events with a photon in the barrel region (left) and endcap region (right). Run 2 data appear as black points, simulation as stacked histograms, with the data over simulation ratio in the lower panel. The red dashed line in the ratio plot denotes the sample average [12].

Photon purity

The photon purity, β_γ is defined as the fraction of all photons (prompt+non-prompt) that are prompt. Prompt photons can be distinguished by both the shape of their showers in the ECAL, as described by the well-known $\sigma_{i\eta i\eta}$ quantity, and their track isolation. Prompt photons are expected to have narrow showers and low-track isolation, while non-prompt photons are characterized by broader shower shapes and longer charged hadron isolation tails.

A combination of templates derived from simulations and data is used to perform a fit on the charged hadron isolation distribution in data, and the relative fraction of prompt and non-prompt photons in the data is determined. The prompt shape is taken from γ+jets MadGraph simulation [114, 115] while the non-prompt shape is taken from QCD MadGraph simulation. The purity is found to be significantly dependent on $H_{\mathrm{T}}^{\mathrm{miss}}$, requiring an evaluation of purity within distinct $H_{\mathrm{T}}^{\mathrm{miss}}$ ranges: $H_{\mathrm{T}}^{\mathrm{miss}} \in$ [250-300, 300-350, 350-600, 600-∞].

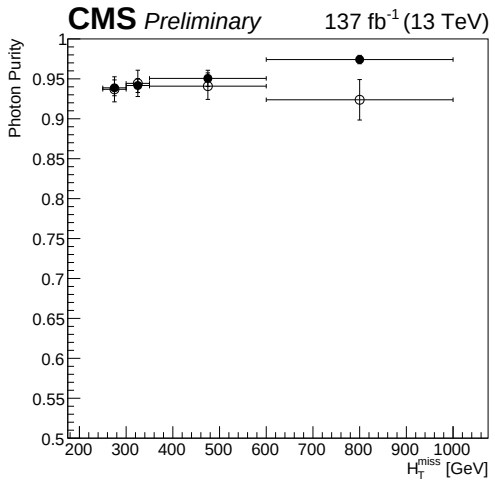

Figure 3.5: Summary of purity fits versus $H_{\mathrm{T}}^{\mathrm{miss}}$ for barrel (solid points) and endcap (open points) photons. The figure shows the purity as measured in the full Run 2 dataset. Uncertainties are based on comparing results using various template shapes for non-prompt photons taken either from the data CR, MC SR, or MC CR [12].

In addition to $H_{\mathrm{T}}^{\mathrm{miss}}$ cuts, all events are required to pass all other baseline selections. The MC templates are derived separately in each $H_{\mathrm{T}}^{\mathrm{miss}}$ range. Although the templates derived from MC simulations are found to provide a reasonable description of both the prompt and non-prompt distributions, an alternative shape for non-prompt photons is obtained using a data sideband. This sideband is created by reversing the $\sigma_{i\eta i\eta}$ cut, resulting in a sample primarily composed of non-prompt photons.

Fitting results using both the nominal templates and the alternate data-derived templates for non-prompt photons are averaged to obtain the central values of photon purity. Systematic uncertainties are taken as the difference between purity fit results with the nominal and alternative non-prompt templates. Figure 3.5 illustrates the photon purity with respect to $H_{\mathrm{T}}^{\mathrm{miss}}$ separately for barrel and endcap photons.

$\mathcal{R}_{Z(\nu\bar{\nu})/\gamma}$ and $\mathcal{F}_{\text{dir}}$

To account for the difference in cross sections and kinematic distributions of Z ($\rightarrow \nu\nu$) + jets and γ + jets events, a transfer factor $\mathcal{R}_{Z(\nu\bar{\nu})/\gamma}$ is used, where $\mathcal{R}_{Z(\nu\bar{\nu})/\gamma}$ is the ratio of Z ($\rightarrow \nu\nu$) + jets and γ + jets events calculated using leading-order generator-level simulation for each analysis bin with $N_{\text{b-jet}} = 0$. The γ + jets simulation is weighted event-by-event with data/MC scale factor (SF) and trigger efficiencies. Defining $\mathcal{C}^{\gamma}_{\text{d/MC}}$ as the product of these SFs and efficiencies, $\mathcal{R}_{Z(\nu\bar{\nu})/\gamma}$ is obtained as follows:

$$\mathcal{R}_{Z(\nu\bar{\nu})/\gamma} = \frac{N^{\text{MC}}_{Z(\nu\bar{\nu})}}{\mathcal{C}^{\gamma}_{\text{d/MC}} N^{\text{MC}}_{\gamma}} \tag{3.4}$$

The method does not require that $\mathcal{R}_{Z(\nu\bar{\nu})/\gamma}$ be independent of the analysis variables, but the fact that the ratio is nearly independent of $H^{\text{miss}}_{\text{T}}$, H_{T}, and N_{jet} simplifies the validation, reducing our dependence on simulation. The most significant variation in $\mathcal{R}_{Z(\nu\bar{\nu})/\gamma}$ is for $H^{\text{miss}}_{\text{T}}$ at low boson p_{T} where the Z and γ mass difference is important. In Fig. 3.6, the values

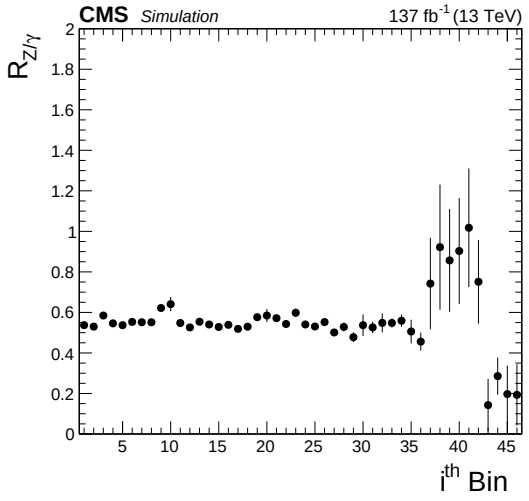

Figure 3.6: Distribution of $\mathcal{R}_{Z(\nu\bar{\nu})/\gamma}$ in the variable analysis bins of the SR from the combined 2016, 2017, and 2018 MC samples. The simulations used here are based on Leading Order (LO) calculations for both photons and Zs. The yields N^{MC}_{γ} used to calculate $\mathcal{R}_{Z(\nu\bar{\nu})/\gamma}$ are weighted by the factor w_{ρ} introduced below, a correction of about 5% [12].

of $\mathcal{R}_{Z(\nu\bar{\nu})/\gamma}$ are shown for the 46 search bins with $N_{\text{b-jet}} = 0$, determined using 2016, 2017, and 2018 MC samples.

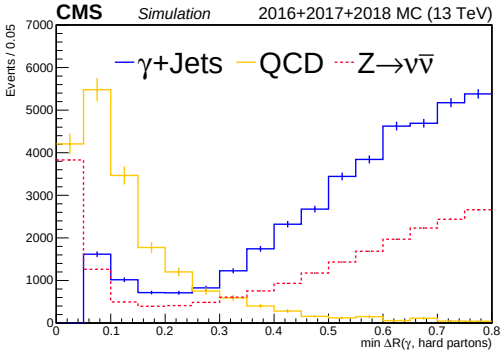

Figure 3.7: The minimum ΔR of the gen-level photon with respect to "hard" partons - after photon CR selection [12].

Fragmentation photons (those with low ΔR to its quark parent) must be treated carefully when computing $\mathcal{R}_{Z(\nu\bar{\nu})/\gamma}$ because γ + jets events that make up the $\mathcal{R}_{Z(\nu\bar{\nu})/\gamma}$ denominator are generated with the requirement that $\Delta R(\gamma, \text{partons}) > 0.4$. The minimum ΔR between the photon and "hard" partons for MC samples with a lower cutoff of 0.05 can be seen in Fig. 3.7. Because these fragmentation prompt photons are included in the γ + jets data sample and are experimentally indistinguishable from direct prompt photons (unlike non-prompt photons), a correction is necessary to account for this missing component in the simulation. This correction is obtained by using prompt photons from the QCD simulation. $\mathcal{F}_{\text{dir}}$ is a correction applied to the γ + jets simulation to account for the fraction of photons with $\Delta R < 0.4$. The value of $\mathcal{F}_{\text{dir}}$ for each of the 46 analysis bins with $N_{\text{b-jet}} = 0$ is depicted in Fig. 3.8, including total uncertainties. These uncertainties include statistical uncertainties, data-MC differences, and the matching of the QCD and γ + jets simulations at the $\Delta R(\gamma, \text{partons})$ transition.

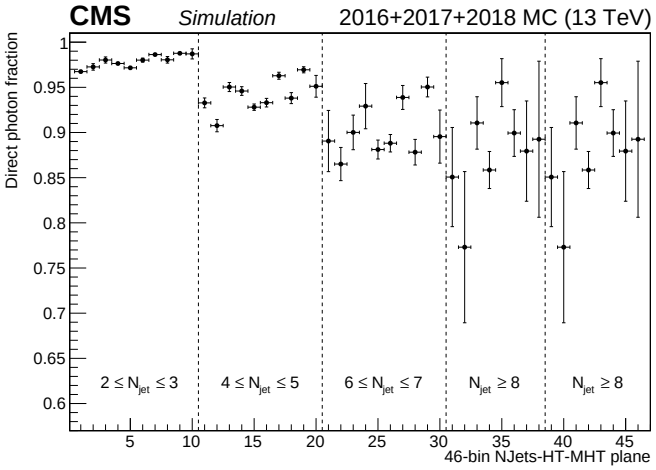

Figure 3.8: Distribution of $\mathcal{F}_{\text{dir}}$ in the 46 analysis bins [12].

$\mathbf{Z \to \ell^+\ell^-}$ selection

Leptons in the dilepton CR are selected using definitions given in the section 3.3 above. Two opposite-sign muon or electron pairs having dilepton invariant masses within 15 GeV of the Z boson mass are selected. After removing the leptons from the event, the same kinematic selection as the SR is applied, including vetoes on events with isolated tracks, photons, or any additional leptons. Additionally, to reject $\bar{\text{tt}}$ contamination, dilepton pair is required to have $p_{\text{T}} > 200$ GeV.

$\mathcal{R}_{Z(\nu\bar{\nu})/\gamma}$ double ratio

The primary source of systematic uncertainty for the γ + jets method comes from our understanding of the accuracy of the leading-order modeling of $\mathcal{R}_{Z(\nu\bar{\nu})/\gamma}$. To address this, a correction to $\mathcal{R}_{Z(\nu\bar{\nu})/\gamma}$ is estimated using $\text{Z} \to \ell^+\ell^-$ + jets data. The correction, called the double ratio (ρ) is given by the Eq. 3.5 below.

$$\rho = \frac{\mathcal{R}^{\text{obs}}_{\text{Z}\to\ell^+\ell^-/\gamma}}{\mathcal{R}^{\text{MC}}_{\text{Z}\to\ell^+\ell^-/\gamma}} = \frac{N^{\text{obs}}_{\text{Z}\to\ell^+\ell^-}}{N^{\text{MC}}_{\text{Z}\to\ell^+\ell^-}} \cdot \frac{N^{\text{MC}}_{\gamma}}{N^{\text{obs}}_{\gamma}} \cdot \frac{\beta_{\ell\ell}}{\mathcal{C}^{\ell\ell}_{\text{d/MC}}} \cdot \frac{\mathcal{C}^{\gamma}_{\text{d/MC}}}{\mathcal{F}_{\text{dir}}\beta_{\gamma}}, \tag{3.5}$$

where $\beta_{\ell\ell}$ and $C^{\ell\ell}_{\mathrm{d/MC}}$ are the purity and SF product, respectively, for the $\mathrm{Z} \to \ell^+\ell^-$ control sample. The anticipated ρ value is close to unity, with potential deviations attributed to the influence of higher-order processes on the overall cross sections of γ + jets and Z+jets processes. In addition, ρ is expected to be independent of the analysis variables $H_{\mathrm{T}}^{\mathrm{miss}}$, H_{T}, and N_{jet}. Linear fits of ρ as functions of each analysis variable are performed to check for any significant deviations from these assumptions in the data.

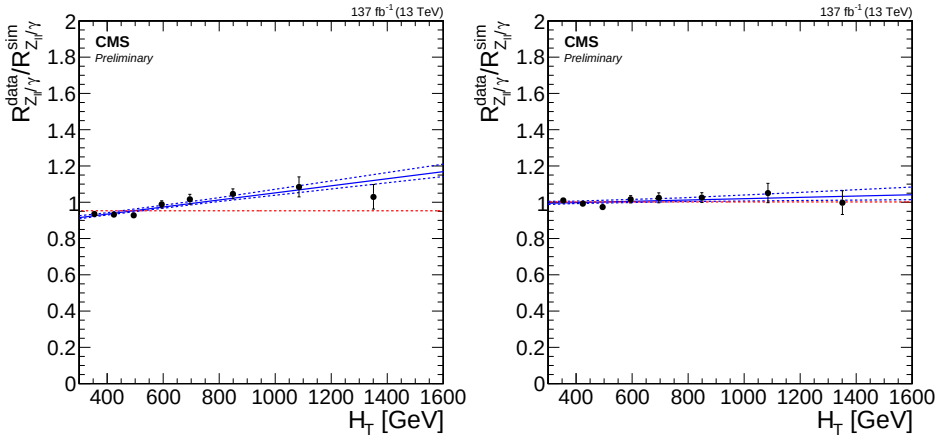

Figure 3.9: ρ versus H_{T} from Run2 data and simulations (left plot). Points with error bars represent the calculated ρ values in each bin, including statistical uncertainties. The plot displays a straight-line fit represented by the solid blue line, accompanied by uncertainties indicated by blue dashed lines. Additionally, the average value is denoted by a red dashed line on each graph. The fit is utilized to correct the γ+jets MC, resulting in the distribution and fit shown in the right-side plot [12].

The average value of $\langle\rho\rangle$ is 0.953. Due to the observed modest non-zero slope in the H_{T} dependence of ρ, as depicted in Fig. 3.9 (left plot), the H_{T} fits are used to determine a weighting function $w_\rho = [0.8566 + 0.0001950 \min(H_{\mathrm{T}}, 900\ \mathrm{GeV})]^{-1}$. This weighting function is then applied event by event to the γ + jets simulation. The distribution of the weighted events is given in Fig. 3.9 (right plot). As expected, after reweighting, $\langle\rho\rangle$ (= 1.002) is essentially unity. This value is applied as a multiplicative correction to the $\mathrm{Z}\to \nu\bar{\nu}$

+ jets background estimate, as in Eq. 3.6.

$$N^{\text{pred}}_{Z\to\nu\nu} = \langle\rho\rangle \cdot \mathcal{R}_{Z(\nu\bar{\nu})/\gamma} \cdot \mathcal{F}_{\text{dir}} \cdot \beta_\gamma(H_{\text{T}}^{\text{miss}}) \cdot N^{\text{obs}}_\gamma \tag{3.6}$$

Measurement of Z ($\to \nu\bar{\nu}$) + jets background for $N_{\text{b-jet}} > 0$

Starting with Z ($\to \nu\bar{\nu}$) + jets prediction in bins with $N_{\text{b-jet}} = 0$, as described above, an extrapolation in the $N_{\text{b-jet}}$ variable is performed using the Z $\to \ell^+\ell^-$ + jets control sample. For this sample, the $N_{\text{b-jet}}$ distribution is assumed to be common for various $\left(H_{\text{T}}, H_{\text{T}}^{\text{miss}}\right)$ bins. However, there is a significant dependence of the $N_{\text{b-jet}}$ distribution on N_{jet} as observed in the simulation. To explicitly express this shape dependence, the following formulation is used.

$$N(\text{Z} \to \nu\nu)^{\text{H}_\text{T},\, \text{H}_\text{T}^\text{miss}}_{\text{N}_\text{jet},\, \text{N}_\text{b-jet}} = \text{N}_{\text{Z}\to\nu\nu}(\gamma + \text{jets})^{\text{H}_\text{T},\, \text{H}_\text{T}^\text{miss}}_{\text{N}_\text{jet},\, 0} \cdot \mathcal{F}_{\text{N}_\text{jet},\, \text{N}_\text{b-jet}}(\text{Z} \to \ell^+\ell^-), \tag{3.7}$$

The prediction $N_{\text{Z}\to\nu\nu}(\gamma + \text{jets})^{H_\text{T},\, H_\text{T}^\text{miss}}_{N_\text{jet},\, 0}$ comes from Eq. 3.6 and the extrapolation factors, $\mathcal{F}_{N_\text{jet},\, N_\text{b-jet}}$ for bins with $N_{\text{b-jet}} > 0$ are directly measured using Z $\to \ell^+\ell^-$ data.

A self-consistency test of the assumption that the extrapolation factors are independent of the kinematic variables $(H_\text{T},\, H_\text{T}^\text{miss})$, is provided by the MC comparison presented in Fig. 3.10. Here the extrapolation factors are derived from Z$\to \ell^+\ell^-$simulation as described above and applied to the expected Z$\to \ell^+\ell^-$simulation events for $N_{\text{b-jet}} = 0$. The results are then overlaid on the expected distribution in all four analysis variables directly from the Z$\to \ell^+\ell^-$simulation. The ratio plots show evidence in some $(N_\text{jet},\, N_\text{b-jet})$ bin groups of trends as functions of $(H_\text{T},\, H_\text{T}^\text{miss})$.

3.4.2 QCD multi-jet background

QCD multi-jet processes can give rise to events with large H_T^miss for three reasons. First, mismeasurement of the energy of jets can lead to a transverse momentum imbalance sometimes called "fake" H_T^miss. Second, jets that fall outside of the acceptance of the jet selection,

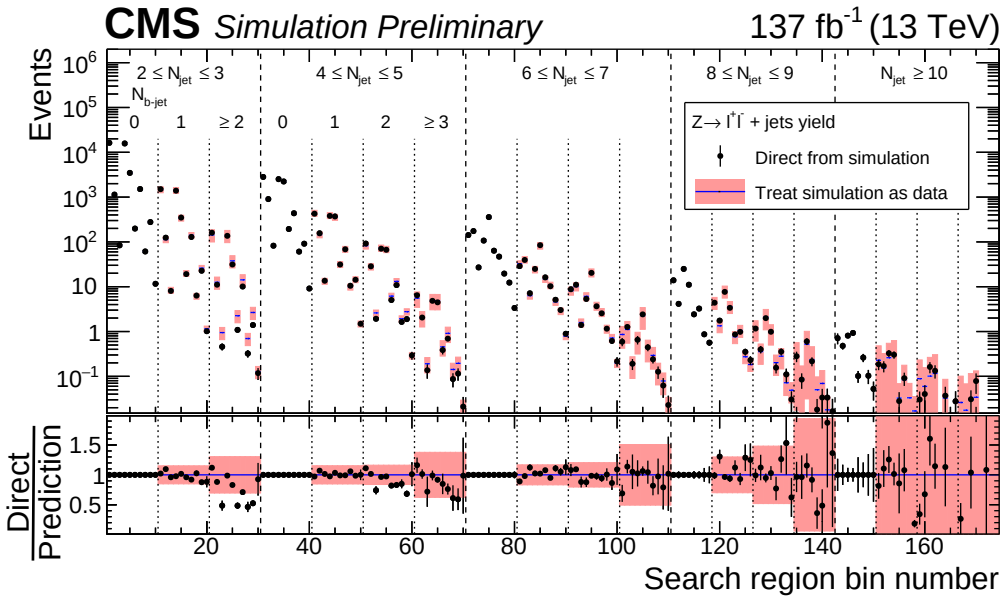

Figure 3.10: Yields scaled to the integrated luminosity of the data from the $Z\to \ell^+\ell^-$ simulation by the procedure described in the text for measuring $\mathcal{F}_{N_{\text{jet}},\, N_{\text{b-jet}}}$ (blue bars with pink bands) compared with the direct expectation from simulation (points with error bars). The pink bands show the statistical uncertainties of the prediction combined with the systematic uncertainty attributable to the kinematic dependence. For bins corresponding to $N_{\text{b-jet}} = 0$ the agreement is exact by construction [11].

namely because they have $p_{\text{T}} < 30$ GeV or $|\eta| > 5$, can give rise to $H_{\text{T}}^{\text{miss}}$ because they are neglected in the vectorial sum. Third, QCD events containing b-quarks can contain neutrinos, which can give rise to real $H_{\text{T}}^{\text{miss}}$. The rebalance and smear (R+S) method is designed to predict the multi-jet background in the case that any of the above sources of $H_{\text{T}}^{\text{miss}}$, or combinations of these sources, are present.

Events are collected by the group of triggers requiring H_{T} to exceed various thresholds between 200 and 1050 GeV, resulting in the seed sample. A minimal selection is applied offline to the seed sample, including the standard baseline event filters and the lepton and photon vetoes. Once the seed sample is collected, each event is subjected to two procedures.

In the first step, called *rebalance*, the jet momenta are re-scaled to force the event into resembling a particle-level QCD-like event. In other words, *rebalance* attempts to undo

the effects of the detector smearing on the particle-level jets, under the assumption that the event was truly of QCD origin. In this step, a posterior density representing the probability of different configurations of parton-level jet four-vectors $\vec{J}_{\text{part}}$, given the set of measured jet four-vectors $\vec{J}_{\text{meas}}$, is maximized with respect to the transverse momenta of the jets. During this maximization, the magnitudes of the jet four-vectors are allowed to vary, taking into account the detector response associated with each jet denoted as $\text{P}(p_{\text{T,meas}}|p_{\text{T,part}})$, and following a low-$H_{\text{T}}^{\text{miss}}$ constraint introduced through the prior $\pi(\vec{J}_{\text{part}})$, which is dependent on the parton-level jets. The posterior density is formulated as follows:

$$\text{P}(\vec{J}_{\text{part}}|\vec{J}_{\text{meas}}) \sim \text{P}(\vec{J}_{\text{meas}}|\vec{J}_{\text{part}}) \cdot \pi(\vec{J}_{\text{part}}). \tag{3.8}$$

The prior is taken to be the $H_{\text{T}}^{\text{miss}}$ distribution of the generated jets in simulation. The prior is binned in the number of b-tags and the H_{T}. The binning in the number of b-tags accommodates $H_{\text{T}}^{\text{miss}}$ arising from neutrinos in the final state, and the binning in H_{T} accommodates $H_{\text{T}}^{\text{miss}}$originating from jets that do not meet the jet selection criteria. After the rebalancing process, a collection of jets known as the rebalanced jets is obtained.

The jet response, representing the ratio of the measured jet p_{T} to the actual jet p_{T}, is obtained from the simulation that has been corrected according to jet energy resolution scale factors. The response is categorized into bins based on both p_{T} and η. The p_{T} binning accounts for the inherent resolution of the calorimeters, which changes with the jet energy, while the η binning addresses variations in the material density between the interaction point and the calorimeters, typically fluctuating with pseudorapidity.

The second step is to *smear* the rebalanced jets according to the detector response associated with each jet. This is done by re-normalizing each rebalanced jet by a number obtained from a random sampling of the appropriate response template. This process yields an event sample that is consistent with reconstruction-level jets in a QCD event. Each event has this smearing procedure applied multiple times, which serves to increase the statistical

precision of the estimate.

Each time an event passes through the smearing step, the desired event selection criteria are applied as if the event were from QCD simulation. The weighted number of rebalanced and smeared events falling into a given SR constitutes the central value of the QCD background estimate. The QCD prediction and observed counts in low $\triangle\phi$ analysis bins is

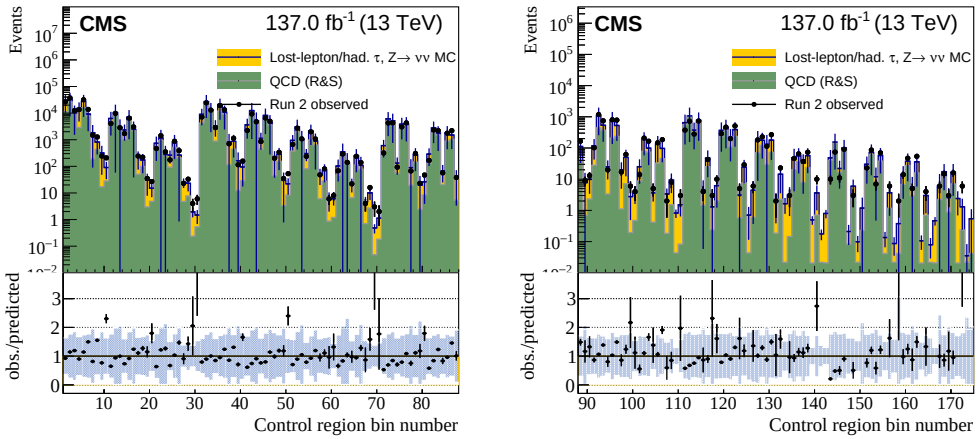

Figure 3.11: Comparison between the prediction and observed counts in the low $\triangle\phi$ analysis control bins in all of the Run 2 data. These regions are analogous to the SRs but with the $\Delta\phi$ selection inverted. Non-QCD contributions are derived from the data-driven methods. The blue-shaded region in the ratio represents the systematic and statistical uncertainties in the QCD prediction and a 30% uncertainty for the non-QCD background components [12].

shown in Fig. 3.11. Statistical and systematic uncertainties are combined in quadrature. The discrepancies between prediction and observed counts are mostly within the 1 σ uncertainty.

3.4.3 $t\bar{t}$ and W+jets background

The $t\bar{t}$ and W+jets processes are SM backgrounds for this analysis which arise in two ways. In the first case, the W boson decays to an electron or muon (with true p_T^{miss} coming from associated neutrinos) but this lepton fails to be identified and the event survives after the lepton veto. In the second case, the W boson decays to a hadronic τ giving a jets + p_T^{miss}

signature that is an irreducible background for this search.

The average transfer factor (TF) method is used to get the background (lost lepton + hadronic τ) prediction in the SR from the CR yield (one lepton). In MC, as the generator level information is available, it is possible to identify an event having either one lepton / zero lepton or hadronic τ and hence is straightforward to obtain the ratio of (lost lepton + hadronic τ) event yield to (one lepton) yield representing TF in MC. To account for discrepancies between data and MC in the yields of "found" leptons, weights denoted as $\mathrm{SF}_{e,\mu}(p_{\mathrm{T}}, \eta)$, covering reconstruction, identification, and isolation, are applied on an event-by-event basis. Before deriving SFs for the "lost" leptons, the SFs for the found leptons are first averaged over each analysis bin.

The $\mathrm{t\bar{t}}$, W+jets, and single top MC samples are used to derive the TF. From MC events passing baseline selection of $N_{\mathrm{jet}} > 2$, $H_{\mathrm{T}} > 300$ GeV and $H_{\mathrm{T}}^{\mathrm{miss}} > 300$ GeV and high $\Delta\Phi$ requirement, a set of events with a single well-identified and isolated electron or muon is selected. This selection requires that the electron should have passed "veto" identification criteria and isolation requirement of $I_{\mathrm{mini}} < 0.1$, while the muon should pass "medium" identification and isolation cut of $I_{\mathrm{mini}} < 0.2$. To make sure that the electron or muon selected is a prompt lepton coming from W decay, reconstruction level lepton should match to the generator level lepton and satisfy an additional requirement of $m_{\mathrm{T}} < 100$ GeV. Here matching is defined as the angle between generator level and reco level lepton should be within $\Delta\mathrm{R} < 0.3$ and relative p_{T} difference ($\Delta p_{\mathrm{T}}/p_{\mathrm{T}}$) between reconstruction and generator lepton should be less than 10%. One-lepton (e or μ) events selected in this way are distributed across the 174 search bins by first applying b-tagging data/MC SFs. These weights define the one-lepton MC yields in the CR [N_{found}(MC)]. Similarly, for the "Lost Lepton+Hadtau" MC yield, [N_{lost}(MC) + $N_{Had\tau}$ (MC)] across various search bins, a subset of events with no isolated lepton or track is selected from the events passing the baseline selection. From

these, the transfer factors in each of the 174 search bins are determined as follows:

$$TF_{\text{MC}} = (N_{\text{lost}}(MC) + N_{Had\tau}(MC))/N_{\text{found}}(MC). \tag{3.9}$$

To adjust for data/MC differences, separate e and μ MC yields in each bin are first corrected by the bin-averaged data/MC SFs to obtain the corrected N_{found} yields [N_{found} ($MC_{\text{corrected}}$)]. The data/MC SF, $\mathcal{C}_{\text{lost}}$, used to correct TF_{MC}.

$$\mathcal{C}_{\text{lost}} = (N_{1\text{prompt}} - N_{\text{found}}(MC_{\text{corrected}}))/N_{\text{lost}}(MC). \tag{3.10}$$

The average transfer factor for each analysis bin is given by

$$TF = \mathcal{C}_{\text{lost}} \cdot (N_{\text{lost}}(MC) + N_{Had\tau}(MC))\,/N_{\text{found}}(MC_{\text{corrected}}). \tag{3.11}$$

TF derived with corrected MC yield is applied on one lepton CR from data to get the "Lost Lepton+Hadtau" yield in the SR. Here one lepton CR in data is defined exactly like in MC and obtained by applying SR triggers to the MET dataset.

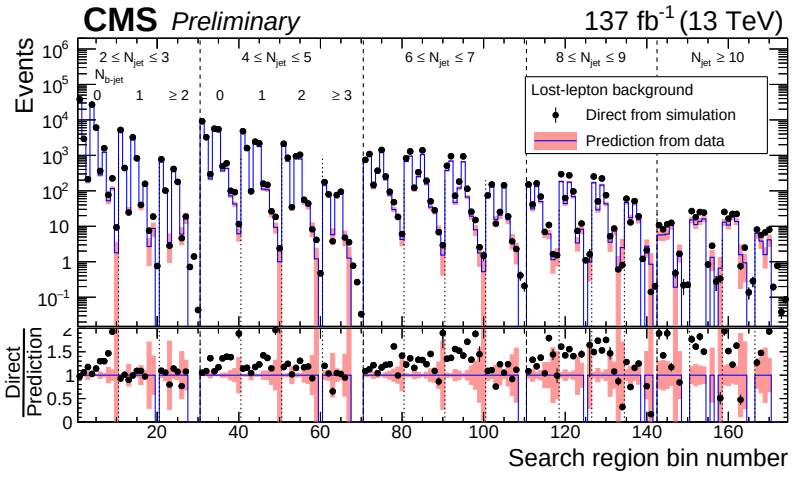

Figure 3.12: Comparison of Lost Lepton+Hadronic tau prediction from 2016+2017+2018 data (pink shaded region) against expectation based on 2016+2017+2018 MC in the SR (solid dots) scaled to 137 fb^{-1} luminosity of data [12].

The method is implemented on one lepton CR of the 2016, 2017, and 2018 MET datasets from Run2 to get a total Lost Lepton + Hadronic tau background. The same set of SR

triggers is used for the CR. The medium working point associated with DeepCSV b-tagging algorithm [116] and SFs are used for all three years. After preliminary data versus MC comparisons in the one lepton CR, the average TF setup is run to estimate the prediction of LL+Hadtau background. The MC prediction is compared against MC expectation in inclusive distributions to gain confidence that there are no major flaws in the estimation strategy. Figure 3.12 shows a comparison of background prediction from Run 2 data against MC-based expectations in the 174 search bins.

The major source of uncertainty for this background is from limited data CR statistics and is treated as "gamma uncertainty" for statistical interpretation. Other sources of uncertainty are jet energy scale uncertainty, uncertainty on lepton SFs, and variation in lepton acceptance caused by uncertainty on the Parton Distribution Function. These uncertainty sources are treated as "log-normal" uncertainties in statistical interpretation.

Uncertainties in background predictions

The uncertainties in the background predictions primarily arise from statistical uncertainties in control sample yields, systematic uncertainties in the transfer factors, and systematic uncertainties in the modeling of the search variables.

3.5 Results

Figure 3.13 illustrates the event counts observed in the 174 search bins. The observed event counts align with the expected backgrounds. Therefore, there is no evidence found for the presence of SUSY particles in this dataset. Upper limits on the production cross-sections for different signal scenarios are calculated using a likelihood fit. The fit involves the SUSY signal strength (μ), the ratio of cross sections ($\mu \equiv \sigma_{\mathrm{SUSY}}/\sigma_{\mathrm{SM}}$), along with signal uncertainties, predicted SM background contributions as illustrated in Fig. 3.13, uncertainties associated with these backgrounds, and the control region yields. Nuisance parameters

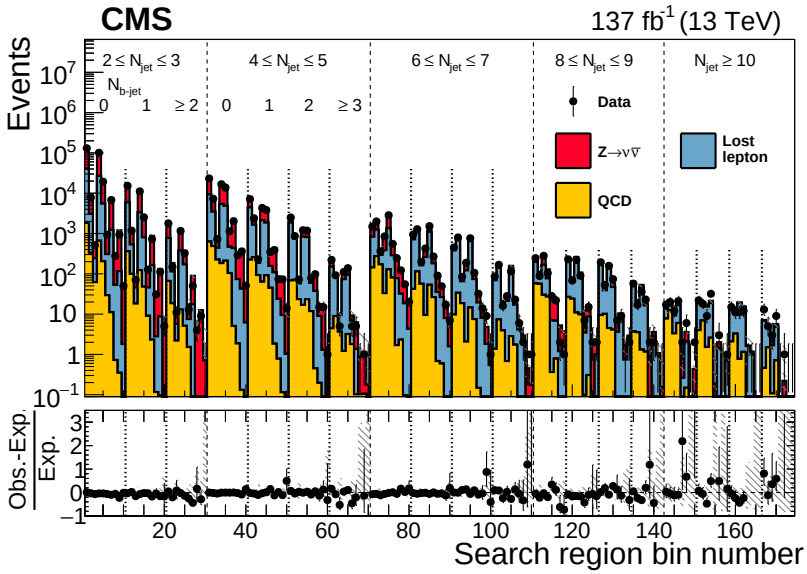

Figure 3.13: The observed event counts alongside the pre-fit SM background predictions are shown in the 174 analysis bins. Here, "pre-fit" implies no constraints from the likelihood fit have been incorporated. Bin numbers match those in Fig. 3.10. Shaded areas indicate the overall uncertainty in background predictions. The lower panel illustrates fractional differences between the data and SM predictions [11].

representing uncertainties in the background, signal shape, normalization, and statistical uncertainties from control samples are constrained in the fit. The likelihood function for each search bin is defined as the product of probability density functions, with Poisson distribution for control region yield and log-normal distribution for nuisance parameters from various sources of systematic uncertainties in signal and background yields. When setting limits, we use the $CL_{(s)}$ method [117, 118], comparing a *model* with signal+background hypothesis to the background-only (null) hypothesis. Here, *model* refers to a cross-section prediction with certain free parameters. In the scenario where s and b represent the estimated signal and background events respectively, and n is the observed data count in a particular search bin, the probability of observing n data events under the signal+background hypothesis is given by:

$$P(n, s+b) = \frac{e^{-(s+b)}(s+b)^n}{n!} \tag{3.12}$$

Under the background-only hypothesis, the probability of observing n data events becomes:

$$P(n,b) = \frac{e^{-b}b^n}{n!} \tag{3.13}$$

Subsequently, we define a test statistic as:

$$-2\ln(Q) = -2 \times \ln\left(\frac{P(n,s+b)}{P(n,b)}\right) \tag{3.14}$$

This test statistic, or likelihood ratio, is useful for distinguishing between the signal+background hypothesis and the background-only hypothesis. For each n, there is a corresponding unique Q value:

- If $P(n,s+b) = P(n,b)$, then $-2\ln(Q) = 0$.
- If $P(n,s+b) > P(n,b)$, then $-2\ln(Q) < 0$.
- If $P(n,s+b) < P(n,b)$, then $-2\ln(Q) > 0$.

For $n = n_{\text{obs}}$, the observed data count in a search bin, the corresponding Q value is denoted as Q_{obs}. With the known Q_{obs}, we define two quantities: $CL_{(b)}$ and $CL_{(s+b)}$, representing the probability of obtaining $Q \leq Q_{\text{obs}}$ under the background-only and signal+background hypotheses, respectively:

$$CL_{(b)} = P_b(Q \leq Q_{\text{obs}}) \tag{3.15}$$

$$CL_{(s+b)} = P_{(s+b)}(Q \leq Q_{\text{obs}}) \tag{3.16}$$

Determining $CL_{(b)}$ and $CL_{(s+b)}$ involves assessing the fraction of the area of the background-only and signal+background probability distribution when $-2\ln(Q)$ is more than $-2\ln(Q_{\text{obs}})$ value. Consequently, the confidence level (CL) of the signal+background hypothesis, normalized to the background-only hypothesis, is expressed as:

$$CL_{(s)} = \frac{CL_{(s+b)}}{CL_{(b)}} \tag{3.17}$$

Achieving a 95% CL upper limit implies $CL_{(s)} < 0.05$. For the observed limit, n_{obs} is equated to the observed data count, while for the expected limit, n_{obs} is equated to the total background estimate. The expected limit measures the (in)compatibility of the background estimate with the model having a mean of $(s+b)$, thereby defining the experimental sensitivity to rejecting the signal+background hypothesis.

The limits for gluino (squark) pair production models are established based on the masses of gluino ($m_{\tilde{g}}$) or squark ($m_{\tilde{q}}$) and the LSP ($m_{\tilde{\chi}_1^0}$). A total of 174 search bins are utilized for each combination of SUSY particle masses. The figure 3.14 presents the observed limits (black curves) and expected limits (red curves) for the gluino pair production models. Gluinos with masses up to 2180 GeV, 2310 GeV, 2000 GeV, and 2030 GeV are excluded [11] based on T1tttt, T1bbbb, T1qqqq, and T5qqqqVV models, respectively. These results mark a significant improvement from our previous analysis [96].

Similarly, the observed exclusion limit (black curves) and expected exclusion limit (red curves) for scenarios involving the production of squark pairs are displayed in Figure 3.15. Squarks with masses up to 1190, 1220, and 1630 GeV are excluded in the T2tt, T2bb, and T2qq scenarios, respectively. These values represent an improvement from our previous study [96]. Notably, for the T2tt model, cross-section upper limits are not presented for small values of $m_{\tilde{\chi}_1^0}$ if $m_{\tilde{t}} - m_{\tilde{\chi}_1^0} \approx m_t$, indicated by the unshaded diagonal region in the upper-left plot of Fig. 3.15. This exclusion is due to the difficulty in distinguishing SUSY signal events from SM $\mathrm{t\bar{t}}$ events in this region, leading to substantial signal contamination in the control regions. Apart from the primary T2qq model featuring four squark flavors (up, down, strange, and charm) with dual quark spin states, Fig 3.15 (lower plot) represents a scenario where only one of these eight states (referred to as *single* $\tilde{q}$) is observable at the LHC. Under these conditions, the upper limit on the squark mass is lowered to 1130 GeV.

The SUSY analysis presented in this chapter is published in [11]. I worked on estimating the SM background contribution arising from Z boson decaying to pairs of neutrinos

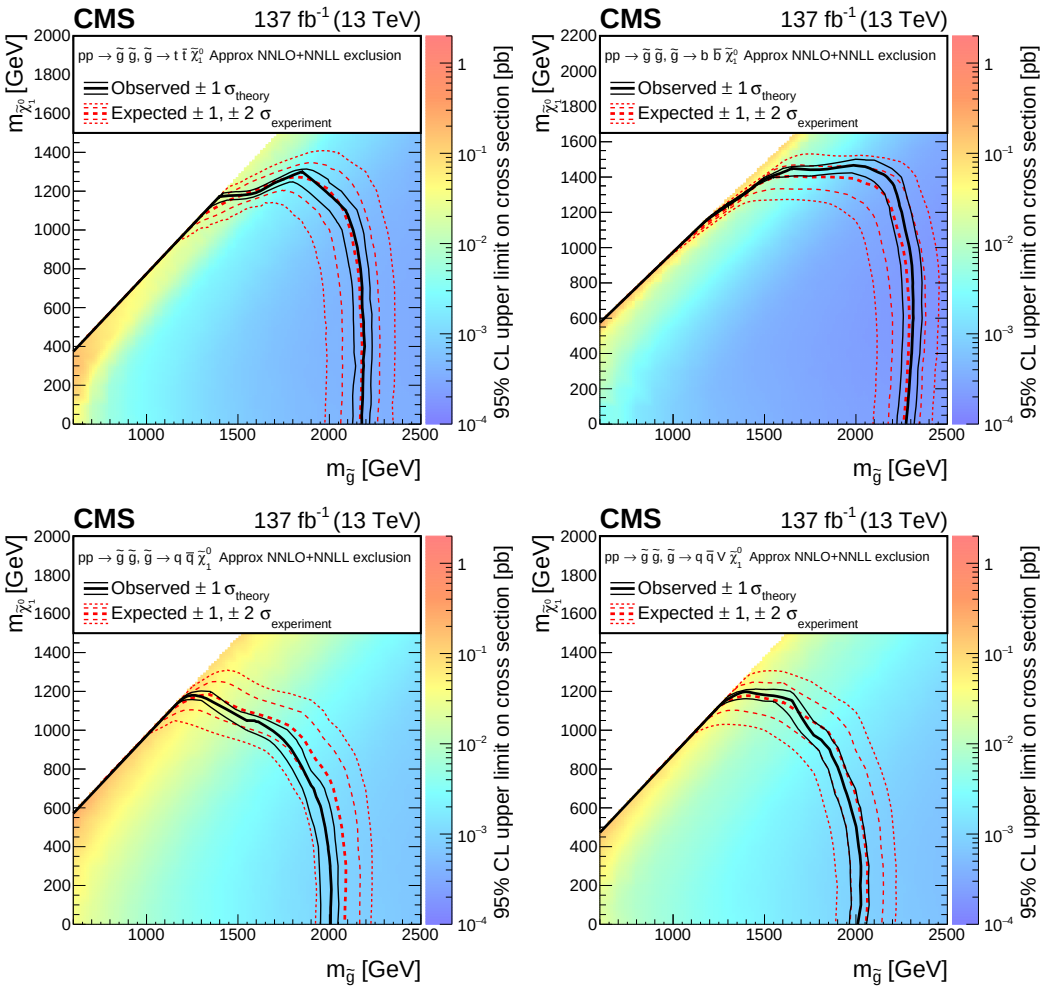

Figure 3.14: The figures present the 95% confidence level upper limits on the production cross sections of various signal models: T1tttt (top left), T1bbbb (top right), T1qqqq (bottom left), and T5qqqqVV (bottom right). These limits depend on the gluino and LSP masses, denoted as $m_{\tilde{g}}$ and $m_{\tilde{\chi}_1^0}$. The thick solid (black) curves depict the observed exclusion boundaries under the assumption of approximate-NNLO+NNLL cross sections. The thin solid (black) curves illustrate the alterations in these boundaries as the signal cross sections undergo fluctuations within their theoretical uncertainties. The thick dashed (red) curves demonstrate the anticipated boundaries under the background-only hypothesis, while the two sets of thin dotted (red) curves delineate the regions containing 68% and 95% of the expected distribution of boundaries under this hypothesis [11].

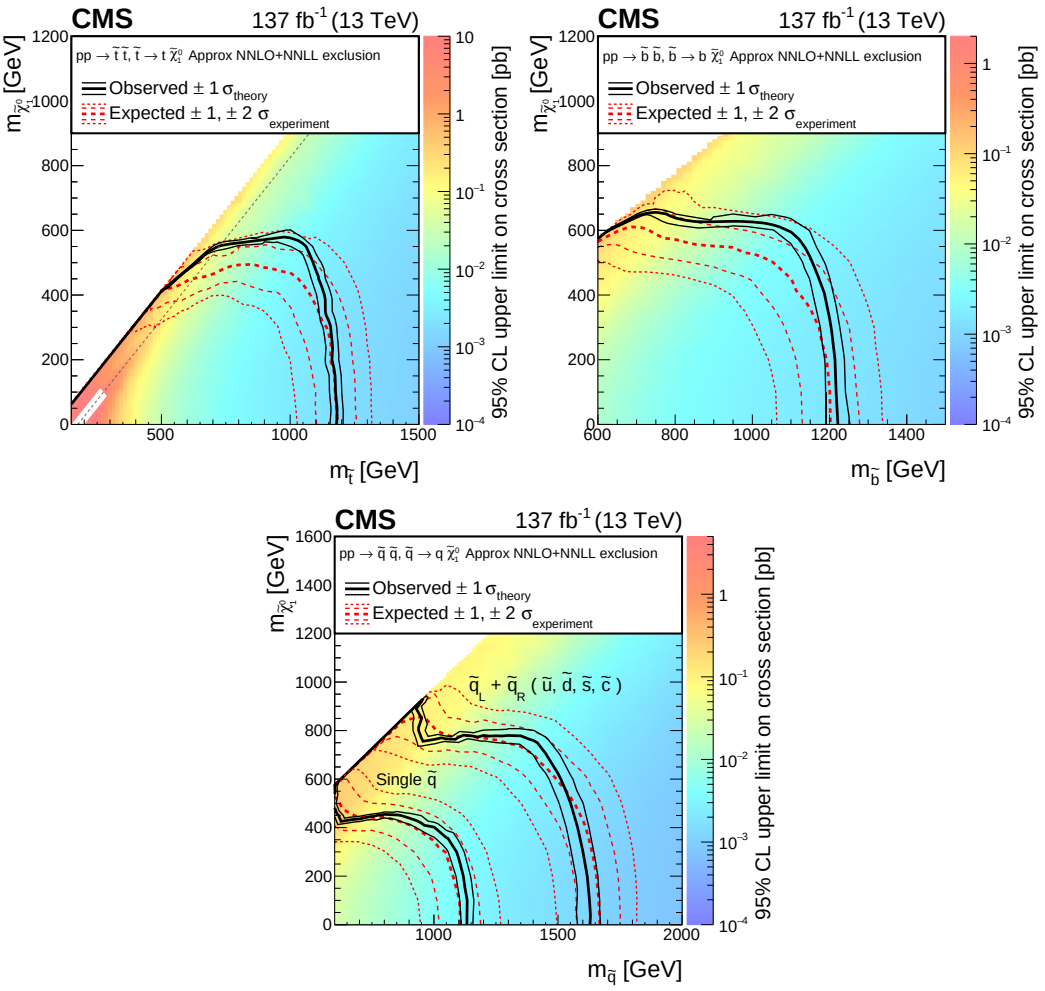

Figure 3.15: The upper limits at a CL of 95% on the production cross sections of the T2tt, T2bb, and T2qq signal models are shown in the respective panels. The interpretation of the curves is explained in the caption of Fig. 3.14. Additionally, the diagonal dotted line in this model corresponds to $m_{\tilde{t}} - m_{\tilde{\chi}_1^0} = m_t$ [11].

accompanied by jets. Despite exhaustive efforts, conclusive evidence supporting SUSY production remained elusive. However, the study established upper limits on the production cross-section for various signal scenarios.

Chapter 4

SUSY search in a photon, a lepton, and missing transverse momentum final states

4.1 Introduction

This chapter presents a search for General Gauge Mediated (GGM) [119, 120, 121] SUSY signatures involving the production of a neutralino-chargino pair, leading to a final state having a photon and a lepton (either e or μ), along with significant p_T^{miss}. The photon (lepton) in the final state originates from neutralino, $\tilde{\chi}_1^0$ (chargino, $\tilde{\chi}_1^{\pm}$) decay into a gravitino,$\tilde{\mathrm{G}}$ and a photon (or $\mathrm{W}^{\pm}$ boson), where $\mathrm{W}^{\pm} \to \ell^{\pm}\nu$. In this analysis, we focus on the following three simplified models, as depicted in Figure 4.1.

- **T5WG:** Simplified version of gluino pair production, where each gluino decays to a quark-antiquark pair and an intermediate neutralino or chargino. Neutralino and chargino masses are set equal, with a 50% branching ratio for gluino decay to the neutralino or chargino states, resulting in a final state of photon plus lepton. The branching fractions BR($\tilde{\chi}_1^0 \to \tilde{\mathrm{G}}\gamma$) and BR($\tilde{\chi}_1^{\pm} \to \tilde{\mathrm{G}}\mathrm{W}^{\pm}$) are set to unity.

- **T6WG:** Similar to T5WG, this model assumes strong production of a pair of squarks. The squark decays to a quark plus an intermediate neutralino or chargino, with a 50% branching ratio for the squark decay to neutralino or chargino.

- **TChiWG:** Model for direct production of $\tilde{\chi}_1^0\tilde{\chi}_1^{\pm}$ pair with mass-degenerate $\tilde{\chi}_1^0$ and $\tilde{\chi}_1^{\pm}$. $\tilde{\chi}_1^0$ undergoes direct decay to a photon and a gravitino, while $\tilde{\chi}_1^{\pm}$ decays to a W boson and a gravitino. This corresponds to an electroweak production mechanism.

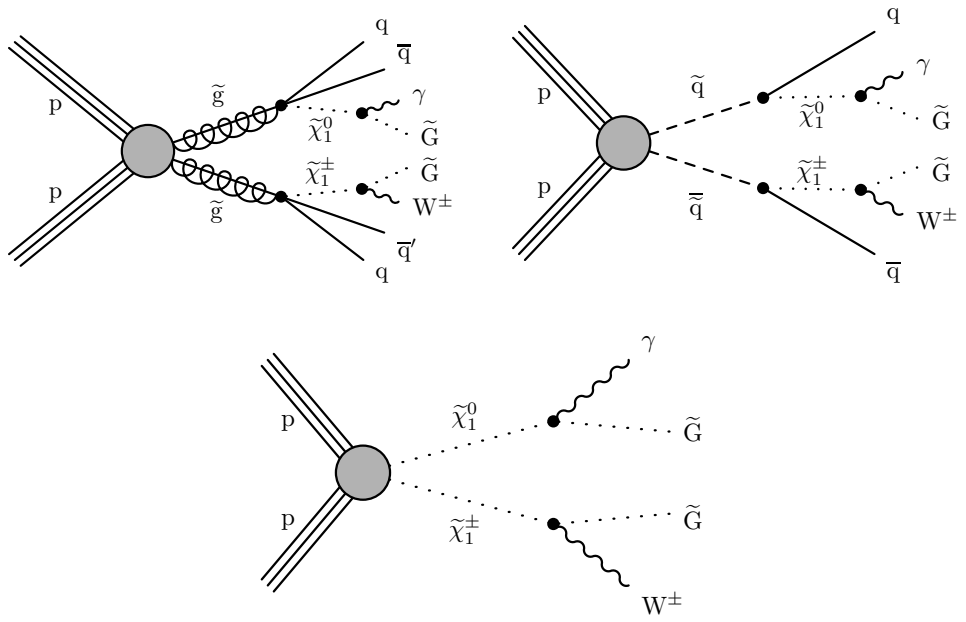

Figure 4.1: Diagrams showing the production of signal events from gluino pair production in the T5WG simplified model (top left), signal events from squark pair production in the T6WG simplified model (top right), and direct electroweak production of $\tilde{\chi}_1^0\tilde{\chi}_1^\pm$ pair (bottom) considered in this analysis [13].

For many years, searches for Gauge-Mediated SUSY Breaking (GMSB) signatures have been carried out at multiple colliders, including the Tevatron, and LHC. Analyses involving events with one or more photons have been undertaken to explore neutralino as NLSP, but no evidence of GMSB has been discovered thus far. Analyses in the photon plus lepton channel were conducted using 8 TeV and 13 TeV proton-proton collision data from ATLAS and CMS detector [122, 123, 14]. None of these analyses observed any significant excess of events over the respective SM predictions. For a model involving electroweak production of a neutralino and chargino, gaugino masses below 930 GeV are excluded previously. Additionally, models on gluino and squark pair production led to the exclusion of gluino masses up to 1.75 TeV and squark masses up to 1.43 TeV in the past analysis. This thesis outlines an ongoing analysis to enhance the sensitivity from the earlier CMS result [14] in the photon plus lepton final state, utilizing the full Run 2 dataset.

In Section 4.2, a description of the data samples along with details of the signal and background simulation samples, and trigger criteria is provided. Section 4.3 provides an overview of object definitions, and the event selection utilized in this analysis. Methods for estimating primary backgrounds in the analysis, utilizing control samples from the data, are detailed in Section 4.4. The observed data in the control region is compared with the expected SM prediction, as described in Section 4.5.

4.2 Datasets and triggers

Collision dataset

The dataset used in this study corresponds to an integrated luminosity of 137.64 fb^{-1} from proton-proton collisions at $\sqrt{s} = 13$ TeV, recorded by the CMS detector at the LHC from 2016 to 2018. The 2016 data is categorized into pre-VFP (Preamplifier Feedback Voltage Bias) and post-VFP eras to address the investigated effect of Highly Ionizing Particles

(HIP). The pre-VFP era of 2016 exhibits the presence of the HIP effect [124, 125], while the post-VFP era of 2016 does not. The luminosity corresponding to 2016 (pre-VFP era), 2016 (post-VFP era), 2017, and 2018 data-taking periods are 19.52 fb^{-1}, 16.81 fb^{-1}, 41.48 fb^{-1}, and 59.83 fb^{-1} respectively. Electrons and photons decay through electromagnetic interaction in ECAL, collectively known as `EGamma` objects. Thus, the dataset for the $e\gamma$ channel contains two `EGamma` objects, abbreviated as `EG`, and it is labeled `DoubleEG`. Similarly, the dataset for the $\mu\gamma$ channel includes a muon and an `EGamma` object, also abbreviated as `EG`, and it is labeled `MuonEG`. Events containing both an electron and a photon ($e\gamma$ channel) were chosen from the `DoubleEG` primary dataset utilizing the diphoton trigger. Conversely, events featuring a muon and a photon in the final states ($\mu\gamma$ channel) were selected from the `MuonEG` dataset, triggered by the muon-photon cross-triggers. In this analysis, the `SingleMuon` dataset, containing events with at least one muon, and the `SingleElectron` dataset, containing events with at least one electron, are employed for various background estimations and efficiency measurements. Tables 4.1 to 4.4 list the dataset names utilized in this analysis, where the convention for dataset naming is documented in [126].

Table 4.1: Data samples for the year 2016 (pre-VFP era) used in the analysis

Dataset
DoubleEG/Run2016B-ver1_HIPM_UL2016_MiniAODv2-v1
DoubleEG/Run2016B-ver2_HIPM_UL2016_MiniAODv2-v3
DoubleEG/Run2016C-HIPM_UL2016_MiniAODv2-v1
DoubleEG/Run2016D-HIPM_UL2016_MiniAODv2-v1
DoubleEG/Run2016E-HIPM_UL2016_MiniAODv2-v1
DoubleEG/Run2016F-HIPM_UL2016_MiniAODv2-v1
MuonEG/Run2016B-ver1_HIPM_UL2016_MiniAODv2-v2
MuonEG/Run2016B-ver2_HIPM_UL2016_MiniAODv2-v2
MuonEG/Run2016C-HIPM_UL2016_MiniAODv2-v2
MuonEG/Run2016D-HIPM_UL2016_MiniAODv2-v2
MuonEG/Run2016E-HIPM_UL2016_MiniAODv2-v2
MuonEG/Run2016F-HIPM_UL2016_MiniAODv2-v2

Table 4.2: Data samples for the year 2016 (post-VFP era) used in the analysis

Dataset
DoubleEG/Run2016F-UL2016_MiniAODv2-v1
DoubleEG/Run2016G-UL2016_MiniAODv2-v1
DoubleEG/Run2016H-UL2016_MiniAODv2-v1
MuonEG/Run2016F-UL2016_MiniAODv2-v2
MuonEG/Run2016G-UL2016_MiniAODv2-v2
MuonEG/Run2016H-UL2016_MiniAODv2-v2

Table 4.3: Data samples for the year 2017 used in the analysis

Dataset
DoubleEG/Run2017B-UL2017_MiniAODv2-v1
DoubleEG/Run2017C-UL2017_MiniAODv2-v2
DoubleEG/Run2017D-UL2017_MiniAODv2-v1
DoubleEG/Run2017E-UL2017_MiniAODv2-v1
DoubleEG/Run2017F-UL2017_MiniAODv2-v2
MuonEG/Run2017B-UL2017_MiniAODv2-v1
MuonEG/Run2017C-UL2017_MiniAODv2-v1
MuonEG/Run2017D-UL2017_MiniAODv2-v1
MuonEG/Run2017E-UL2017_MiniAODv2-v1
MuonEG/Run2017F-UL2017_MiniAODv2-v1

Table 4.4: Data samples for the year 2018 used in the analysis

Dataset
EGamma/Run2018A-UL2018_MiniAODv2-v1
EGamma/Run2018B-UL2018_MiniAODv2-v1
EGamma/Run2018C-UL2018_MiniAODv2-v1
EGamma/Run2018D-UL2018_MiniAODv2-v2
MuonEG/Run2018A-UL2018_MiniAODv2-v1
MuonEG/Run2018B-UL2018_MiniAODv2-v1
MuonEG/Run2018C-UL2018_MiniAODv2-v1
MuonEG/Run2018D-UL2018_MiniAODv2-v1

Simulation

All MC simulation samples used in this analysis, including their cross-sections, are listed in Table 4.5. The SM processes are primarily generated using MadGraph_aMC@NLO [114]

generator, except W+γ samples, which are generated at leading order (LO) using MadGraph generator. To correct the cross-section of W+γ sample, a constant next-to-next leading order (NNLO) k-factor [127] of 1.34 [128, 129] is applied. The hard scattering processes are interfaced with Pythia8 [83] for the simulation of parton showers, hadronization, and decay. Detector simulations are conducted using a Geant4 [89] based package with a detailed description of the CMS detector. To address the potential mis-modeling of the pile-up profile in simulations, MC events are reweighted. This reweighting adjusts the distribution of the number of vertices in the MC events to match the one observed in the data, as illustrated in Figure 4.2.

Table 4.5: List of the MC samples used for signal and SM background processes, with their cross sections in pico barn (pb)

Process	Sample name	σ(pb)
SUSY signal	SMS-T5Wg_TuneCUETP8M1_13TeV-amcatnloFXFX-pythia8	
	SMS-TChiWG_TuneCUETP8M1_13TeV-amcatnloFXFX-pythia8	-
$W\gamma$	WGToLNuG_TuneCP5_13TeV-madgraphMLM-pythia8	412.7
	WGJets_MonoPhoton_PtG-40to130_TuneCP5_13TeV-madgraph-pythia8	19.75
	WGJets_MonoPhoton_PtG-130_TuneCP5_13TeV-madgraph-pythia8	0.8099
$Z\gamma$	ZGToLLG_01J_5f_TuneCP5_13TeV-amcatnloFXFX-pythia8	51.1
$t\bar{t}\gamma$	TTGJets_TuneCP5_13TeV-amcatnloFXFX-madspin-pythia8	3.757
$t\bar{t}$	TTJets_TuneCP5_13TeV-amcatnloFXFX-pythia8	750.5
WW	WW_TuneCP5_13TeV-pythia8	75.95
WZ	WZ_TuneCP5_13TeV-pythia8	27.59
$WW\gamma$	WWG_TuneCP5_13TeV-amcatnlo-pythia8	0.2147
$WZ\gamma$	WZG_TuneCP5_13TeV-amcatnlo-pythia8	0.04345
DY	DYJetsToLL_M-50_TuneCP5_13TeV-amcatnloFXFX-pythia8	6404.0
γ	GJet_Pt-40toInf_DoubleEMEnriched_MGG-80toInf_TuneCP5_13TeV_Pythia8	874.2
QCD	QCD_Pt-20_MuEnrichedPt15_TuneCP5_13TeV-pythia8	

Trigger

Triggers [100, 101] play a crucial role in retaining a selected portion of data events that hold significance for physics analysis. In the $e\gamma$ channel, signal candidate events are collected using the diphoton HLT trigger, with each HLT diphoton path being initiated through a log-

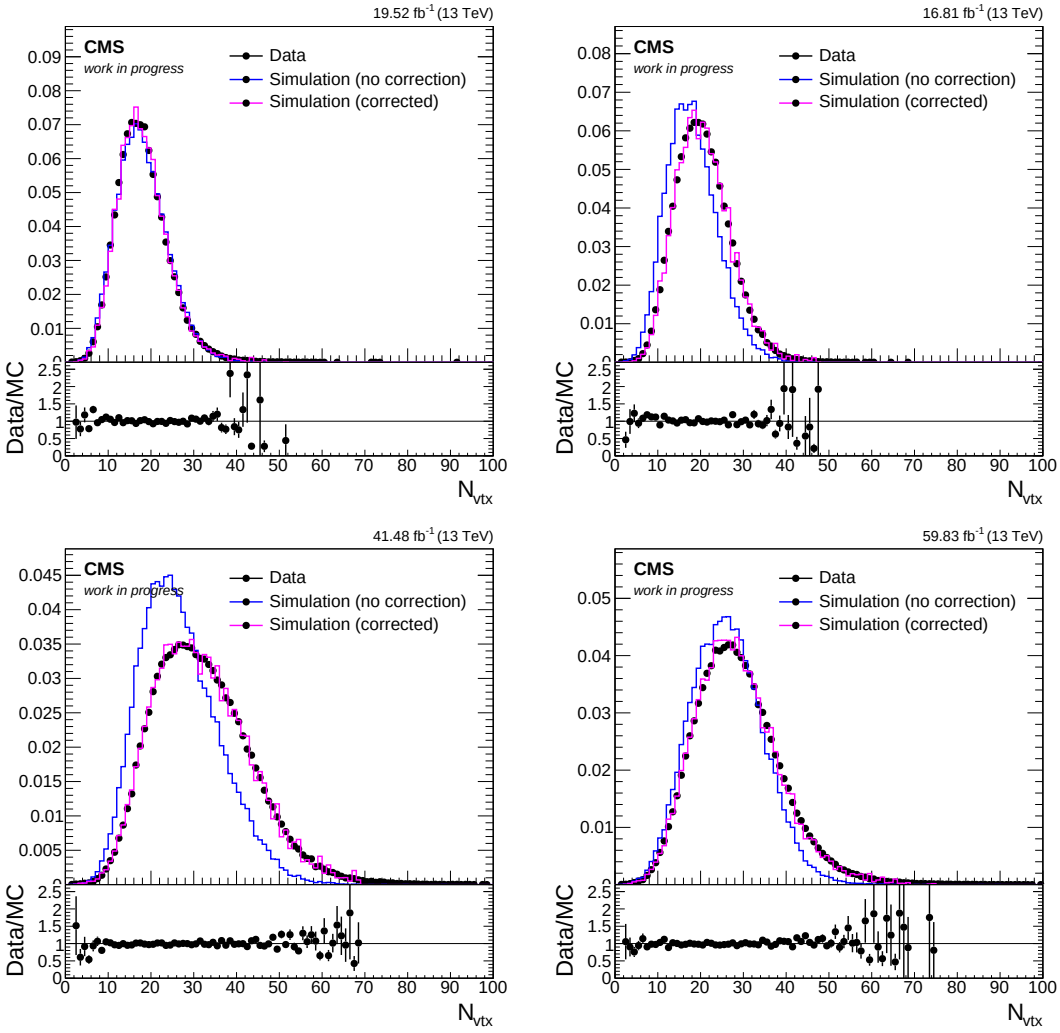

Figure 4.2: To correct pile-up profile mismodeling in simulations, we reweight simulation events to match the distribution of reconstructed vertices in simulation to that measured in the data. The distribution of reconstructed vertices is compared between data (depicted by black dots) and simulation (represented by solid lines) for the years 2016 (upper left for the pre-VFP era, upper right for the post-VFP era), 2017 (lower left), and 2018 (lower right). Simulated events are shown both before the pile-up reweighting (illustrated in blue) and after the pile-up reweighting (depicted in magenta). The lower panel displays the ratio between the data and the reweighted simulation.

ical OR operation involving a list of Level 1 (L1) EGamma triggers. Conversely, in the $\mu\gamma$ channel, events are selected using a muon-photon cross trigger supplemented by a muon trigger in logical OR to compensate for potential trigger inefficiencies caused by the isolation requirement in the L1 EGamma seed. Table 4.6 provides an overview of the triggers used in this analysis for selecting $e\gamma$ or $\mu\gamma$ events. The triggers are named according to criteria, such as the p_T threshold, and other identification criteria for the electron, muon, or photon objects. The details of the CMS trigger study and the CMS trigger naming scheme can be found in [102, 103, 104].

Table 4.6: Dataset types and the corresponding HLT paths used to select events during different data-taking periods. The $e\gamma$ signal events are selected from DoubleEG/EGamma dataset using diphoton trigger and the $\mu\gamma$ signal events are selected from MuonEG datasets using muon-photon triggers. For background estimations, samples of events selected from the SingleElectron dataset using a single electron trigger and the SingleMuon dataset using a single muon trigger are used.

Dataset	**Trigger**
	2016
DoubleEG	HLT_Diphoton30_18_R9Id_OR_IsoCaloId_AND_HE_R9Id_Mass90
MuonEG	HLT_Mu17_Photon30_CaloIdL_L1ISO OR HLT_Mu38NoFilterNoVtx_Photon38_CaloIdL
SingleElectron	HLT_Ele27_WPTight_Gsf_v*
SingleMuon	HLT_IsoMu24_v* || HLT_IsoTkMu24_v*
	2017
DoubleEG	HLT_Diphoton30_22_R9Id_OR_IsoCaloId_AND_HE_R9Id_Mass90
MuonEG	HLT_Mu17_Photon30_IsoCaloId OR HLT_Mu43NoFiltersNoVtx_Photon43_CaloIdL
SingleElectron	HLT_Ele35_WPTight_Gsf_v
SingleMuon	HLT_IsoMu27_v*
	2018
DoubleEG	HLT_Diphoton30_22_R9Id_OR_IsoCaloId_AND_HE_R9Id_Mass90
MuonEG	HLT_Mu17_Photon30_IsoCaloId OR HLT_Mu43NoFiltersNoVtx_Photon43_CaloIdL
EGamma	HLT_Ele32_WPTight_Gsf_v*
SingleMuon	HLT_IsoMu24_v*

4.3 Object definitions, search variables, and event selection

Photon

Photons with p_T more than 35 GeV reconstructed in the ECAL barrel ($|\eta| < 1.4442$) are selected. They are required to match the trigger objects of the HLT within a radius of $\Delta R <$ 0.3 and should have $R_9 > 0.5$, where R_9 is a shower shape variable [130] which makes a good separation between unconverted photons (energy not spread in the tracker) and converted photons (energy spread by the magnetic field before reaching ECAL). Out of such preselected photons, those fulfilling the cut-based loose-ID criteria [131] are selected as candidate photons. The loose-ID criteria require H/E $<$ 0.04596, where H (E) [132] signifies the energy deposition in the HCAL (ECAL), and $\sigma_{i\eta i\eta} <$ 0.0106, where $\sigma_{i\eta i\eta}$ [132] characterizes the shower spread in the η direction. Additionally, it involves charged hadron isolation [132], $\text{Iso}_h^{\pm} < 1.694$, where $\text{Iso}_h^{\pm}$ calculates the sum of p_T for all charged particles around the photon candidate. The conditions also encompass $\text{Iso}_h^0 < 24.032 + 0.01512 \cdot p_T + 0.00002259 \cdot p_T^2$, where Iso_h^0 represents the neutral hadron isolation [132], calculating the sum of p_T for all neutral hadrons around the photon candidate, and $\text{Iso}_{pho} < 2.876 + 0.004017 \cdot p_T$, where Iso_{pho} represents the photon isolation [132], which is the sum of p_T for photons around the photon candidate. The isolation parameters are calculated by summing the sideways momentums of charged hadrons (charged hadron isolation), photons (photon isolation), and neutral hadrons (neutral hadron isolation) within a cone of $\triangle = 0.4$ around the direction of the electron or photon. As the energy of incoming electrons or photons increases, more energy is dispersed around their direction in the different subdetectors. Hence, the cutoffs set for the isolation measures are often adjusted based on the p_T of the particle. To mitigate the occurrence of electron faking as photon events, candidate photons must satisfy a "pixel track seed veto" requirement, described in Section 2.2.3. Additionally,

photons within a radius of $\Delta R < 0.02$ of an electron are rejected, a selection is known as the "electron veto" in later sections of this chapter. This veto is essential for eliminating very rare instances in which ECAL clusters fail to match with pixel seeds, yet electrons are still reconstructed through the ECAL-driven tracking algorithm.

Electron

Electrons with p_T more than 25 GeV within $|\eta|$ less than 2.5 are used, while those falling in the barrel-endcap region ($1.4442 < |\eta| < 1.566$) are excluded for improved acceptance efficiency. Electrons that meet kinematic criteria are required to align with the sub-leading leg of the diphoton trigger. Additionally, a preselection cut of $R_9 > 0.5$ (0.8) is applied to electrons in the barrel (endcap) region to mimic the R_9 filters in the trigger.

Candidate electrons are required to pass a cut-based medium identification selection [110, 130], which includes specific values for variables like $\sigma_{i\eta i\eta}$, eta width ($\Delta\eta_{in}$), phi width ($\Delta\phi_{in}$), H/E, $|\frac{1}{E} - \frac{1}{p}|$, as well as requirements for expected missing hits in the inner tracker layers and a conversion veto. The relative isolation cut is eliminated from the medium identification selections. Instead, a condition is imposed stating that the mini-isolation of the electron, as explained in Section 3.3, be below 0.1. All these mentioned selections differ depending on whether the electrons are in the barrel or endcap region. These criteria collectively help to identify suitable candidate electrons for further analysis.

Muon

Muons with p_T greater than 25 GeV and $|\eta|$ less than 2.4 are selected. A muon is required to match the trigger leg to qualify as a muon candidate. Muons are identified based on standard medium identification criteria [133]. These criteria involve satisfying the PF muon identification, being reconstructed as a global muon or tracker-muon, having more than 80% valid tracker hits, and meeting either the good global muon criteria or having a segment

compatibility greater than 0.451. Additionally, muons are subject to pass impact parameter selection and isolation checks, ensuring that their transverse impact parameter (Dxy) is below 0.05 cm and longitudinal impact parameter (Dz) is below 0.1 cm. Furthermore, muons are required to have a mini-isolation value of less than 0.2 to meet the criteria for selection.

p_T^{miss} and $M_T(l, p_T^{miss})$

The missing transverse momentum (p_T^{miss} or MET) is determined by taking the negative vector sum of the transverse momenta of all reconstructed objects in an event.

For this analysis, the signal region is defined as $p_T^{miss} > 120$ GeV and $M_T(l, p_T^{miss}) > 100$ GeV, where

$$M_T = \sqrt{2 p_T^{miss} p_T^l (1 - cos\Delta\phi(l, p_T^{miss}))}$$

is the transverse mass of the lepton and p_T^{miss} system. This variable effectively distinguishes between SUSY signal and SM backgrounds. Additionally, recommended MET filters are applied to remove events with spurious MET, such as detector noise, cosmic rays, and beam halos.

Jet and HT

This search utilizes AK4 Particle Flow (PF) jets, reconstructed via the anti-k_T algorithm [105] with a radius of 0.4. The selection criteria involve choosing jets with p_T exceeding 30 GeV and having an absolute value of η less than 2.5. Jets overlapping with photon or lepton candidates are excluded to prevent double counting. The scalar sum of p_T of all jets is defined as HT.

Photon final state radiation (FSR)

Energetic and isolated photons can be produced during the decay of vector bosons (W or Z) or emitted from leptons. These events are termed final state radiation (FSR) and have the potential to mimic SUSY signals when substantial p_T^{miss} is present. The simulation shows that the distance between the photon and the lepton is usually closer in FSR events compared to SUSY signal events. As a result, three additional criteria are introduced to mitigate FSR contributions. First, the candidate photon must be well separated from the candidate lepton by $\Delta R(\ell, \gamma) > 0.8$. Second, there should not be any nearby leptons reconstructed close to the candidate photon within $\Delta R < 0.3$. Third, in the $e\gamma$ channel, an additional requirement that the invariant mass of electron and photon ($M_{e\gamma}$) must exceed the mass of the Z boson (M_Z) by at least 10 GeV. These measures collectively enhance the distinction between FSR and SUSY signal events.

4.4 SM Backgrounds

The SM backgrounds in this study are categorized into three groups. The primary background arises from vector boson (W or Z) production accompanied by a photon (V + γ). For this background, neutrinos from leptonic decays of vector bosons escape the detector, contributing to genuine p_T^{miss}. The second category of background arises from misidentified objects, such as mis-reconstructed electrons or jets resulting in fake photons, and the misidentification of a jet as a lepton. These backgrounds are estimated using data-driven methods in the $p_T^{miss} < 70$ GeV CR and extrapolated to the SR. Lastly, there are rare but non-negligible backgrounds originating from the associated production of multiboson or top quarks along with a photon, which is taken from simulation.

4.4.1 Misidentification of electrons as photons

The misidentification of electrons as photons may occur due to mismatches between ECAL clusters and track seeds in the pixel detector during the reconstruction process. Such instances can originate from Drell-Yan di-electron events where the supposed photon candidates are mis-reconstructed electrons. Moreover, $t\bar{t}$ and WW events with final states featuring ee or $e\mu$ combinations can also enter the signal selection if one electron is mistaken as a photon.

To estimate this background, an electron-enriched proxy sample is created, and a misidentification rate, representing the rate of fake photons arising from electron objects, is applied to it. The proxy sample is generated by reversing the pixel track seed veto and electron veto for the signal photon candidates while applying the other selection criteria. Ensuring a pixel seed match for the photon effectively replaces it with a well-reconstructed electron. The misidentification rate is determined using a tag-and-probe method [134] in the $p_T^{miss} < 70$ GeV control region. The process involves selecting di-electron events from Z boson decays, triggered by `HLT_Ele27_eta2p1_WPLoose_Gsf` using `SingleElectron` dataset. A well-reconstructed electron with $p_T > 30$ GeV, which closely matches the single electron trigger leg within a radius of $\Delta R < 0.3$, is designated as the "tag" object. Subsequently, a photon that satisfies all selection criteria except for the pixel track seed veto and electron veto is chosen as the "probe". The invariant mass of the tag and probe pair should correspond to the mass of the Z boson. If the probe fails either the pixel track seed veto or electron veto criteria, the event contributes to the denominator sample of misidentification rate, labeled as ee. If the probe passes both pixel track seed veto and electron veto criteria, the event enters the numerator sample of misidentification rate, denoted as $e\gamma$ in this context. The electron to photon misidentification rate (R) is defined as the ratio of the number of $Z \to ee$ events in the numerator sample ($N^{e\gamma}$) to the number of $Z \to ee$ events in the denominator

sample (N^{ee}), $R = N^{e\gamma}/N^{ee}$. To determine $N^{e\gamma}$ and N^{ee}, a fit within the range [60 GeV, 120 GeV] is performed on the tag and probe invariant mass using the RooFit [135] package. The fit model comprises two probability density functions: one that describes the shape of the signal ($Z \to ee$ process), and the other that models the background. The Breit-Wigner

	Signal Model	Background Model
nominal shapes	Breit-Wigner convoluting with crystal ball	μ + probe template
alter signal shapes	Drell-Yan simulation convoluting with Gaussian	μ + probe template
alter background shapes	Breit-Wigner convoluting with crystal ball	exponential function

Table 4.7: Nominal and alternative functional templates used to fit the tag-and-probe invariant mass.

function is chosen to characterize the signal shape while accounting for radiation loss and resolution effects involves convoluting the signal function with a double-sided crystal ball density function. It is noted that the background in the denominator sample primarily arises from processes involving a genuine electron, such as di-electron decay of $t\bar{t}$. Conversely, in the numerator, backgrounds can originate from processes featuring a true photon, such as $W(\to \nu e)+\gamma$ and $Z(\to ee)+\gamma$. In both cases, utilizing lepton flavor symmetry enables the replacement of the tag electron with a muon and the background shape is approximated using the distribution of μ plus probe invariant mass. Finally, the distribution of the μ+probe invariant mass is smoothed using a Gaussian kernel estimator.

The systematic uncertainties in the fit mainly arise from the mis-modeling of the signal and background shape. To evaluate this, the invariant mass distributions are refitted using alternative shapes. The specific choices of fitting functions are summarized in Table 4.7. We use the differences in fake rates obtained using the nominal templates and the altered templates to measure the systematic uncertainties. Figure 4.3 depicts the fitting results of the numerator samples using the nominal fitting functions across different probe p_T bins, while Figure 4.4 illustrates the corresponding outcomes for the denominator samples. After determining the normalization and parameters for the signal functions from the fit, the

values of N^{ee} and $N^{e\gamma}$ are calculated by integrating the signal shapes in their respective samples over the range of 80 GeV to 101 GeV.

The misidentification rate, $R = N^{e\gamma}/N^{ee}$ is applied to the proxy sample to estimate the number and shape of the electron fake as a photon in the signal region. However, it is important to note that the kinematic distributions of signal photon candidates may differ from the ones from Z decay events, which could result in a different fake rate. To accurately extrapolate the misidentification rate to the signal region, dependencies on three variables are considered. The variables are p_T of the probe, the η of the probe, and the number of vertices (N_{vtx}) in the event. The choice of p_T and η is motivated by tracker efficiency dependence on these two variables, while N_{vtx} is used to account for the pileup effect. The misidentification rate as a function of p_T of the probe, η of the probe, and N_{vtx} are illustrated in Figure 4.5. The dependencies of the misidentification rate on p_T of the probe and N_{vtx} can be represented using parametric functions as follows:

$$\begin{aligned} f(p_T) &= (a + b \cdot p_T)^{-\alpha} \\ f(N_{vtx}) &= c + \beta \cdot N_{vtx} \end{aligned}$$

The parameters obtained by fitting the functions to fake rate distributions are a, b, c, α, and β. Assuming that the fake rate depends on each variable independently, the combined fake rate can be expressed as a function of p_T of the probe, η of the probe, and N_{vtx} using the following formula:

$$f(p_T, \eta, N_{vtx}) = N \cdot f(p_T) \cdot f(N_{vtx}) \cdot f(\eta) \tag{4.1}$$

Here, $f(\eta)$ is determined by the fake rate within the corresponding η bin. Here, N represents a constant, and it is determined by applying the misidentification rate to the denominator sample, requiring that the predicted number of fake photons matches $N^{e\gamma}$. This combined fake rate is applied to the electron-enriched proxy sample to estimate the SM back-

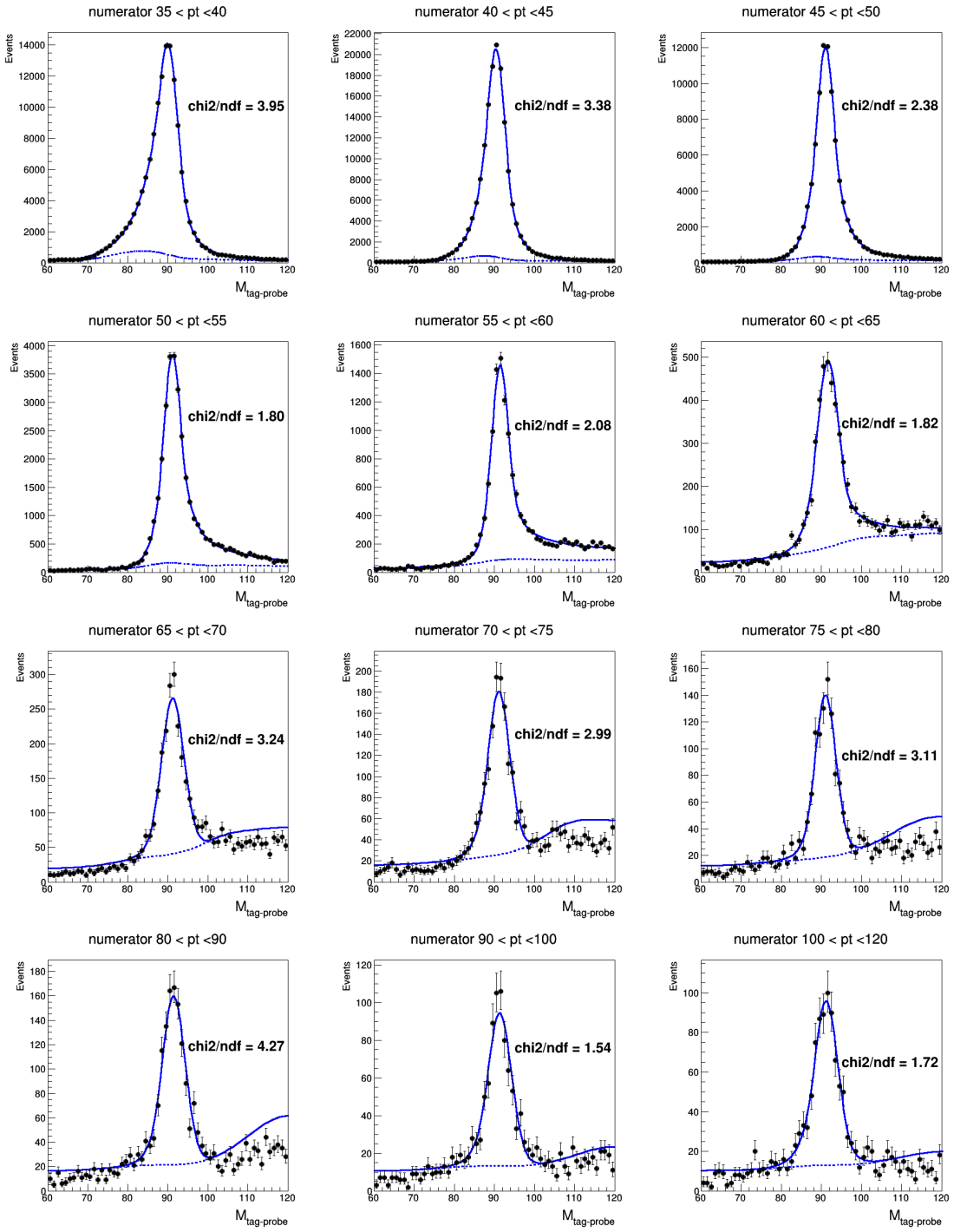

Figure 4.3: Fitting is performed to the tag-and-probe invariant mass within the numerator samples, characterized as samples where probe electrons fail to be matched with pixel track seeds. These fits are using 2018 data and are performed for different p_T bins. The data, signal+background model, and background-only model are denoted by black dots, blue solid lines, and blue dashed lines, respectively [13]. Above each plot, the chi-squared per degree of freedom, indicating the goodness of fit, is reported.

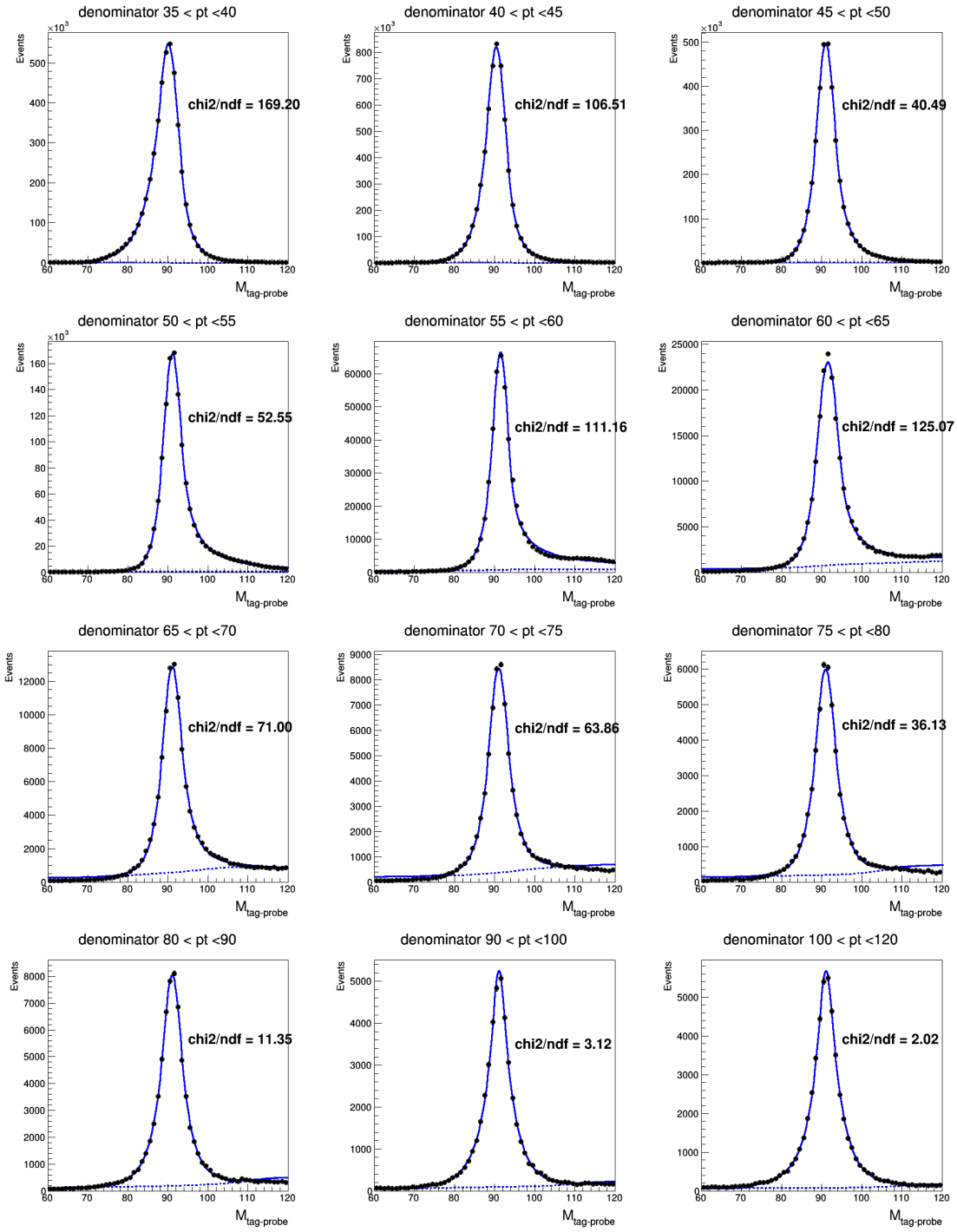

Figure 4.4: Fitting is performed to the tag-and-probe invariant mass within the denominator samples, characterized as samples where probe electrons match pixel track seeds. These fits are using 2018 data and are performed for different p_T bins. The data, signal+background model, and background-only model are denoted by black dots, blue solid lines, and blue dashed lines, respectively [13]. Above each plot, the chi-squared per degree of freedom, indicating the goodness of fit, is reported.

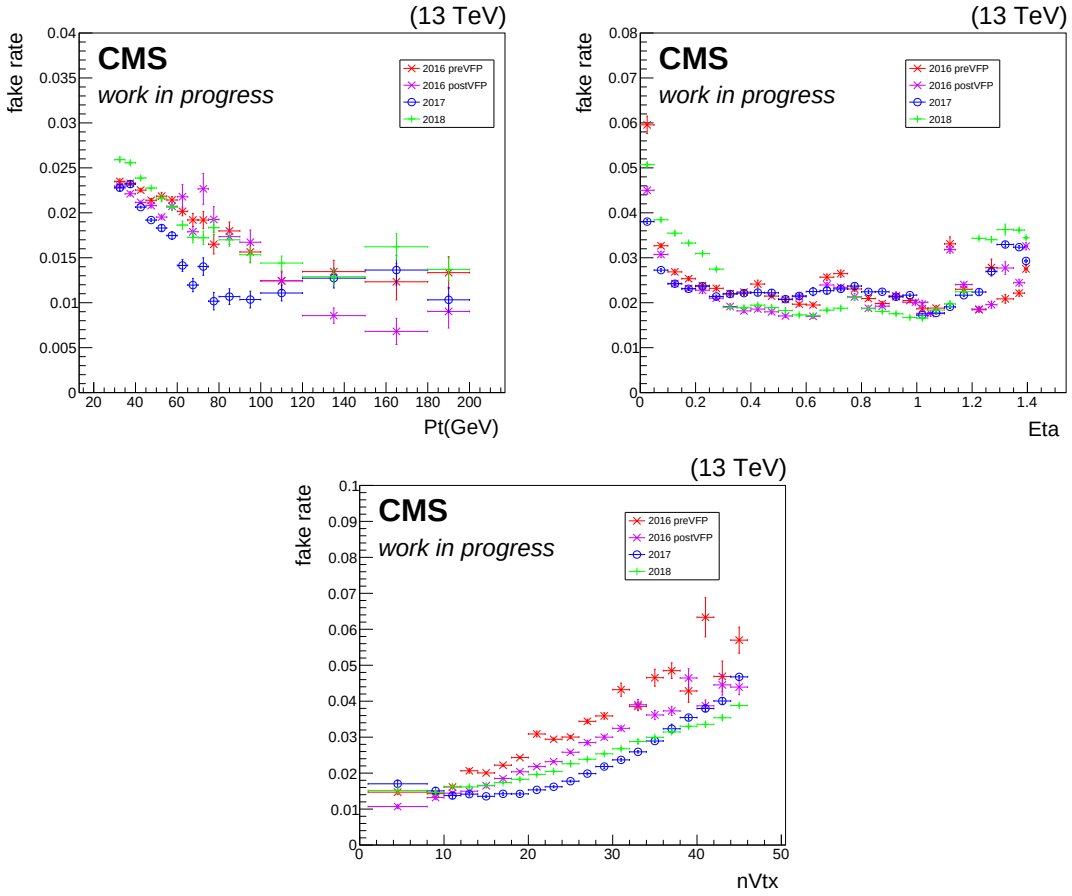

Figure 4.5: The Figure displays the electron misidentification rate as a function of p_T of the probe (top left), η of the probe (top right), and number of vertices (N_{vtx}) in the event (bottom) for the years 2016 (pre-VFP era, and post-VFP era), 2017, and 2018 [13].

ground contribution from misidentified electrons. To evaluate uncertainties in the electron-to-photon misidentification background, toy Monte Carlo studies are conducted.

4.4.2 Misidentification of hadrons as photons

Jets with electromagnetic fluctuations can deposit a substantial portion of their energy in the ECAL and mimic photon signals. This commonly happens when jet energy is mostly carried by a π^0 or η particle that subsequently decays into two nearly collinear photons. The rate at which jets are misidentified as photons is relatively low. However, due to the large cross-section of the QCD process, these misidentified jets can still contribute significantly to the backgrounds. Estimating such backgrounds through simulation is challenging due to the need for large statistics and potential inaccuracies in modeling hadron fragmentation and hadronization. Therefore, a data-driven approach is employed to predict this background. Initially, a proxy-to-fake transfer factor is determined, representing the ratio of the estimated number of fake photons to the number of jet proxy objects, in $p_T^{miss} < 70$ GeV control region. This transfer factor is then applied to a control sample with e/γ enriched jets to predict the jet fakes as a photon contribution in the high p_T^{miss} signal region.

To calculate the proxy-to-fake transfer factor, the fraction of hadrons within the candidate photons (hadron fractions) needs to be determined. Fake photons are characterized by broader shower shapes and more hadronic activities compared to genuine photons. Therefore, variables such as shower shape variable ($\sigma_{i\eta i\eta}$) [136] and charged hadron isolation ($\text{Iso}_{\text{h}^\pm}$) [136] can distinguish between genuine and fake photons. Hadron fraction is derived using a template fit to the $\text{Iso}_{\text{h}^\pm}$ distribution in data. Initially, a well-identified lepton and a photon passing all selection criteria except $\sigma_{i\eta i\eta}$ and $\text{Iso}_{\text{h}^\pm}$ are selected from the data. Among these photons, those passing the shower shape cut, i.e. $\sigma_{i\eta i\eta} < 0.01031$ are chosen as the fit target. The $\text{Iso}_{\text{h}^\pm}$ distribution of photons falling within the range of $0.0103 < \sigma_{i\eta i\eta} < 0.015$ is used to create the hadronic template, whereas the true photon template

is obtained from the γ+jet simulation, where photons are matched to prompt photons at the generator level. The fit to the $\text{Iso}_{\text{h}^\pm}$ distribution is made using RooFit [135] package. The fit is performed in fourteen p_T bins of probe separately for the $e\gamma$ and $\mu\gamma$ channels. The fitting results for the $e\gamma$ channel are shown in Figure 4.6. After determining the normalization of the hadronic template, integration is performed over the range $0 < \text{Iso}_{\text{h}^\pm} < 1.295$ to estimate the number of fake photons in the candidate samples. The hadron fractions, f_{had} is defined as $f_{had} = \frac{N_{fake}}{N_{sig}}$, where N_{fake} represents the estimated number of fake photons, and N_{sig} is the number of events that meet all selection criteria. Figure 4.7 illustrates the computed f_{had} as a function of photon p_T.

After the hadron fractions have been determined, the number of fakes in the candidate photons can be calculated, and it is used as the numerator for the transfer factor. The denominator sample for the transfer factor is a jet-enriched proxy sample, formed by photon objects that pass loose identification conditions (H/E, Iso_{pho}, Iso_{h^0}), alongside requirements like pixel track seed veto, electron veto, and FSR veto. The photon object should have either $\sigma_{i\eta i\eta} > 0.01031$ or $1.29 < \text{Iso}_{\text{h}^\pm} < 15$ GeV. In the control region with $p_T^{miss} < 70$ GeV, the transfer factor is calculated as the ratio of events in the numerator sample to those in the denominator sample. To extend this transfer factor from low p_T regions to high p_T regions with limited statistics, the photon p_T spectrum of the numerator and denominator samples is fitted separately using a sum of two exponential functions, as illustrated in Figure 4.8. This transfer factor is then applied to a control sample with e/γ enriched jets to predict the jet fakes as a photon contribution in the high p_T^{miss} signal region.

The choice of the $\sigma_{i\eta i\eta}$ selection criteria for the hadronic template introduces a significant source of systematic uncertainty in the fraction of fakes. This uncertainty is evaluated by varying the definition of the hadronic template and repeating the fit with the modified template. The scanning of the lower bound of the hadronic template is performed in steps of 0.0101 from 0.01031 to 0.0112, while the upper bound is scanned in steps of 0.0105

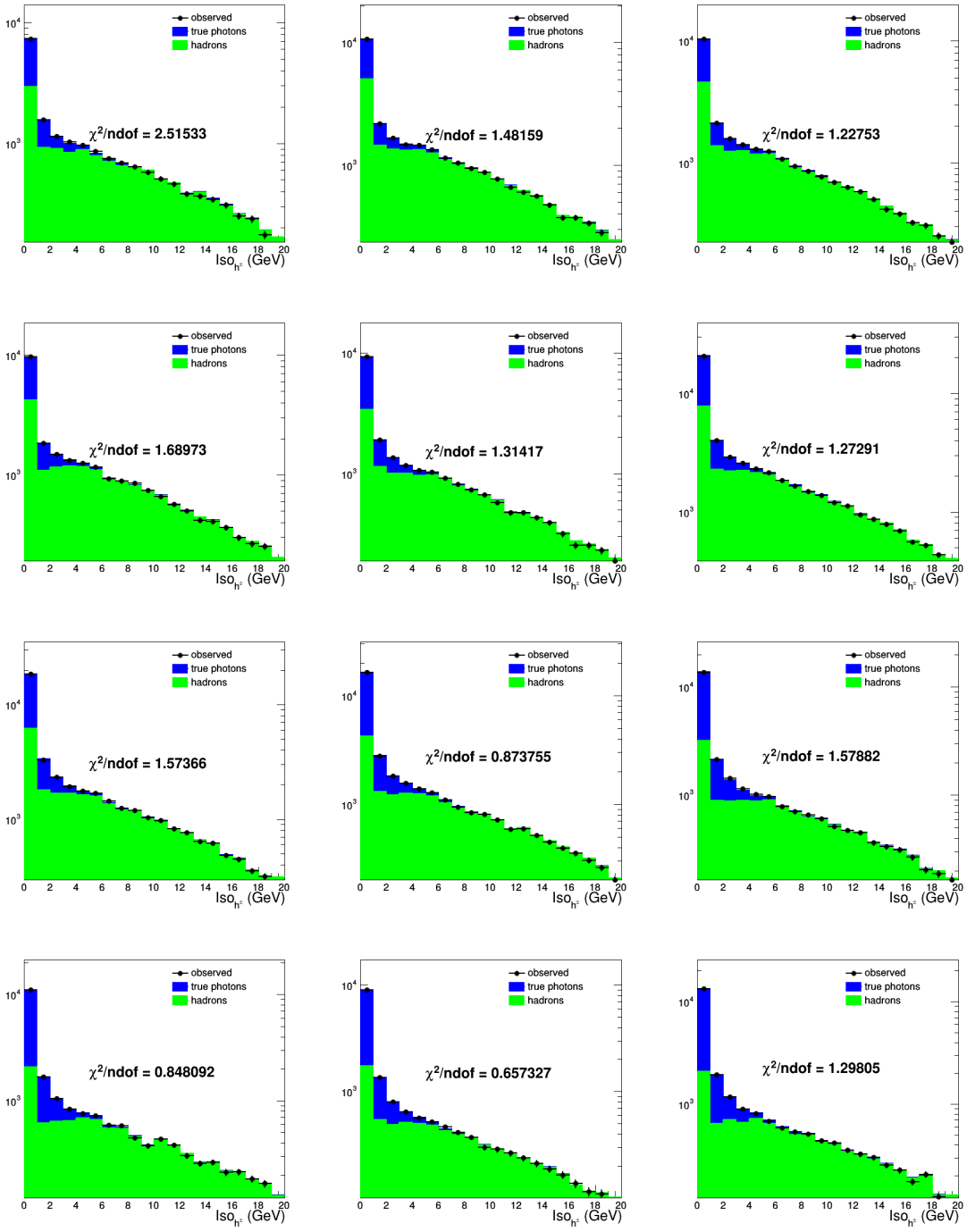

Figure 4.6: For hadron fraction measurements, template fits on charged hadron isolation ($\mathrm{Iso}_{\mathrm{h}^{\pm}}$) are performed across different photon p_T bins, with the data, true photon template, and hadronic template denoted by black dots, blue-filled histograms, and green-filled histograms, respectively. The fitting results for the eγ channel in the year 2018 are shown [13]. Above each plot, the chi-squared per degree of freedom, indicating the goodness of fit, is reported.

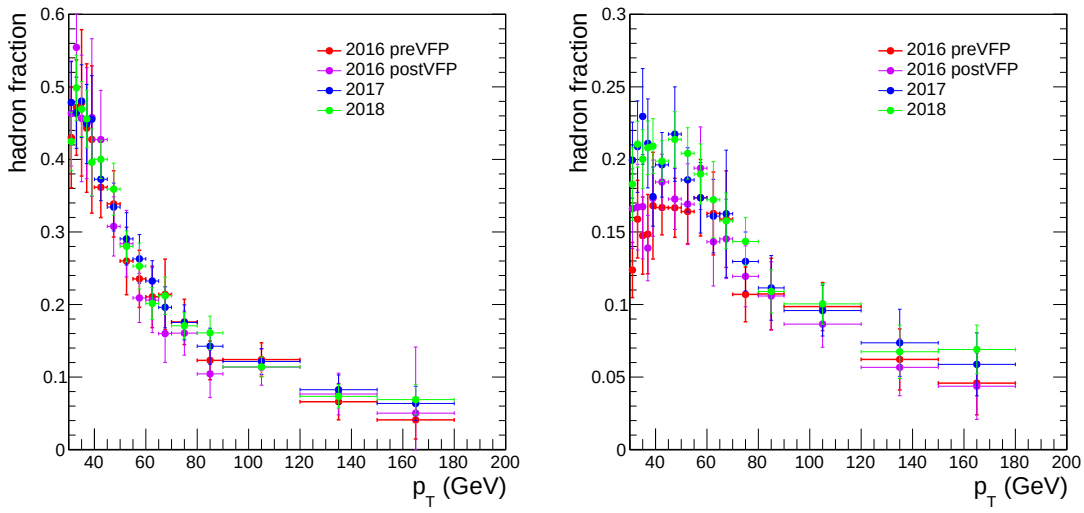

Figure 4.7: Hadron fractions as a function of photon p_T are shown in the $e\gamma$ (left) and $\mu\gamma$ (right) channels for the years 2016 (pre-VFP era, post-VFP era), 2017, and 2018. These fractions are estimated from template fits on $\mathrm{Iso}_{\mathrm{h}^{\pm}}$, as illustrated in Figure 4.6.

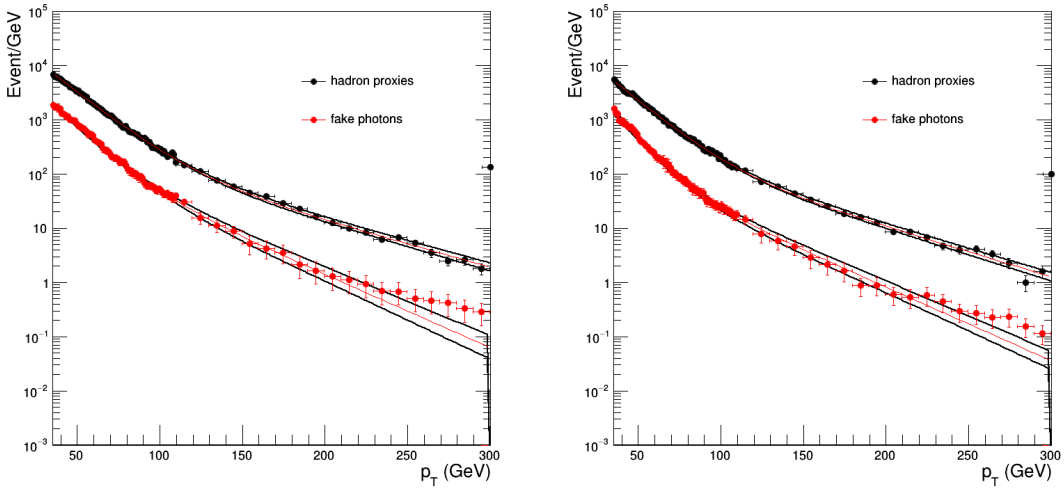

Figure 4.8: For jet-fake-photon transfer factor measurements, function fits on the p_T distributions of photons in the $e\gamma$ (left) and $\mu\gamma$ (right) channels for the year 2017 are shown. The p_T distributions of the proxy objects (denominator sample) and fake photons (numerator sample) are represented by black and red dots, respectively, with the one standard deviation error bands of the fittings displayed in black lines [13].

from 0.0140 to 0.0185. The systematic uncertainties in the hadron fraction get propagated to the functional form of the fake photons via the p_T spectrum fitting. To quantify these uncertainties, 1000 parameter sets were generated from a Gaussian distribution based on the fitting parameters and their errors. This resulted in a one standard deviation error band for the p_T distribution, as depicted in Figure 4.8.

4.4.3 Misidentification of hadrons as leptons

Events with jets and prompt photons can enter the signal region if the jets are mistakenly identified as leptons. All leptons that do not originate from a $W^{\pm}$ or Z are considered fakes, encompassing those arising from heavy-flavor decays, misidentified jets, light-meson decays, and electrons resulting from photon conversions. Simulated QCD events indicate that fake muons primarily originate from heavy-flavor quarks, while fake electrons predominantly come from light-flavor jets with a substantial electromagnetic component.

The estimation of fake lepton background follows a similar approach to that of fake photon background. A proxy sample of events enriched in fake leptons is selected, and then a scale factor is applied to this sample to estimate the background in the signal region. The proxy sample is chosen to closely resemble the signal candidate selection, requiring one candidate photon, and one fake lepton proxy.

Fake electron proxies

In simulations, fake electrons often stem from light flavor jets, displaying characteristics such as broader cluster shapes in η, a significant energy sum surrounding the objects, and a less consistent alignment between the reconstructed track momentum and cluster energy. Thus, the subsequent criteria are applied to elect electron objects for the proxy sample: electrons with p_T greater than 25 GeV, falling within $|\eta| < 1.442$ or $1.56 < |\eta| < 2.5$ regions, and satisfying the medium identification criteria [110] for H/E, $|\frac{1}{E} - \frac{1}{p}|$, expected

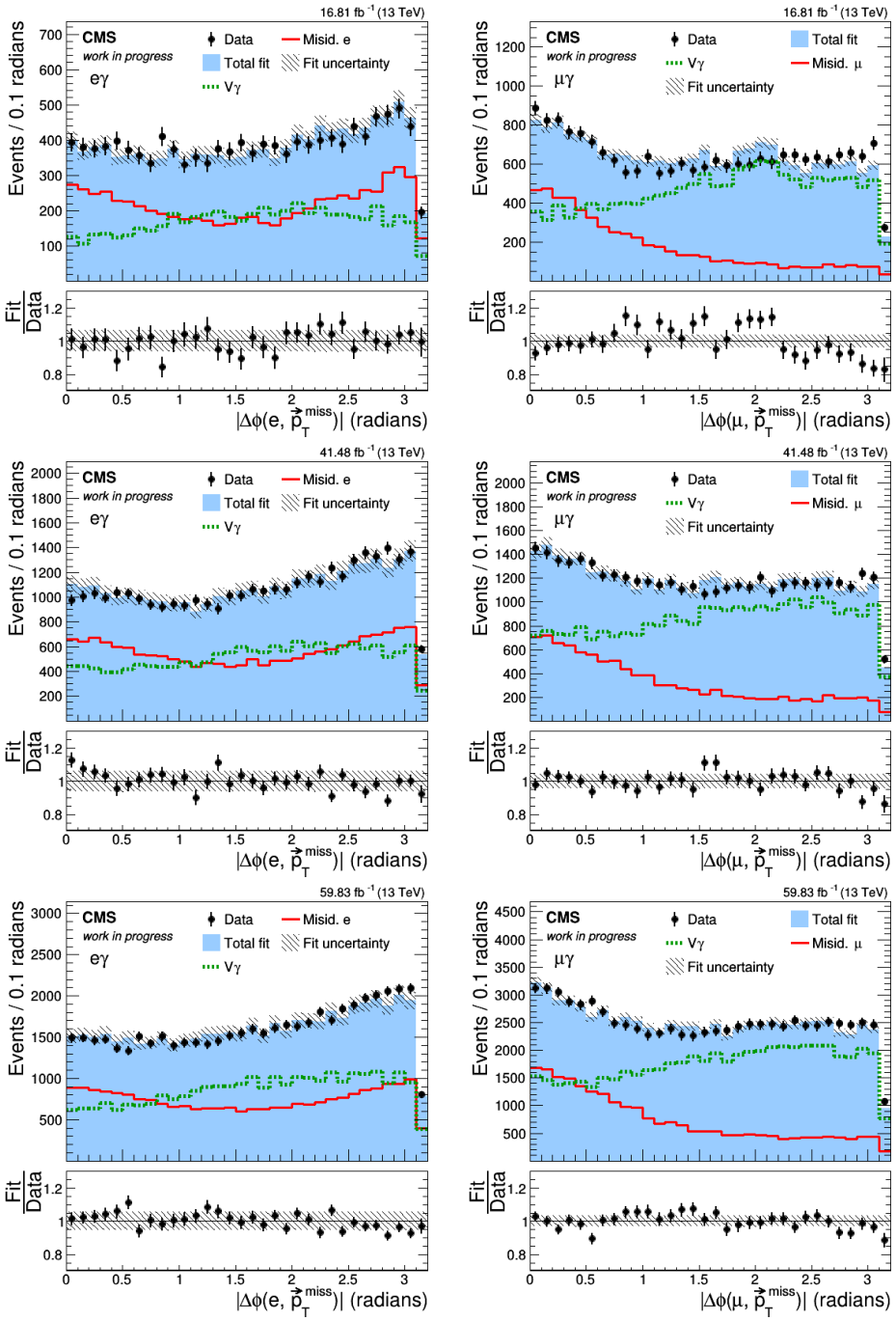

Figure 4.9: In the $e\gamma$ and $\mu\gamma$ channels, distributions of $|\Delta\phi(\ell, p_T^{miss})|$ for the data (black points), along with estimated backgrounds from Vγ (dashed green line) and misidentified leptons (solid red line), are presented for the $40 < p_T^{miss} < 70$ GeV control region. The filled histogram represents the result of the overall fit, and the hatched area indicates the fit uncertainty. The vertical bars on the points depict the statistical uncertainty in the data. The lower panels display the ratio of the fit result to the data [13]. These distributions are showcased for the years 2016 post-VFP era (upper plots), 2017 (middle plots), and 2018 (lower plots).

missing hits in the inner tracker layers and conversion veto. Additionally, they should fail at least one of the criteria for $\sigma_{i\eta i\eta}$, eta width ($|\Delta\eta|$), phi width ($|\Delta\phi|$), and possess a mini-isolation of less than 0.4.

Fake muon proxies

The simulation indicates that fake muons typically originate from the decay of heavy-flavor quarks. These non-prompt muons have primary identification variable distributions similar to those of prompt muons, making them challenging to distinguish based on these variables. Therefore, the key discriminator for identifying fake muons is the mini-isolation variable, which tends to have higher values for muons produced from heavy-flavor quark decays. Consequently, muon proxy candidates are selected based on specific criteria, including muon $p_T > 25$ GeV, muon $|\eta| < 2.4$, passing the cut-based medium identification criteria [133], and having mini-isolation values between 0.2 and 0.4.

The scale factor for the fake lepton proxy sample is determined in a control region with $40 < p_T^{miss} < 70$ GeV, using a template fit to the $\Delta\phi\,(l, p_T^{miss})$ distribution. In this control region, after excluding the contribution of fake photons, the dominant processes are $W\gamma/Z\gamma$ and fake lepton events. The p_T^{miss} in the fake lepton events typically arises from mismeasured objects, resulting in a distinct $\Delta\phi\,(l, p_T^{miss})$ shape compared to that of the $W\gamma/Z\gamma$ processes. The $\Delta\phi\,(l, p_T^{miss})$ distribution in the data is simultaneously fitted with templates for the fake lepton proxy sample and the $W\gamma/Z\gamma$ simulated samples to determine the normalization, as illustrated in Figure 4.9. This normalized fake lepton proxy sample is then used to estimate the background contribution from events with fake leptons in the signal region.

4.4.4 $W\gamma$ and $Z\gamma$ background

The primary background for this search arises from the standard model production of W or Z bosons in association with a photon. To estimate this background, the simulated samples are scaled by a factor determined in the CR through a template fit. The $W\gamma$ sample is constructed by combining the inclusive `WGToLNuG` sample (for $W(\to \ell\nu)\gamma$) with two samples binned by p_T: `WGJets_MonoPhoton_PtG-40to130` and `WGJets_MonoPhoton_PtG-130`. The first sample is truncated at the photon p_T value of 50 GeV, while the high-statistics p_T-binned samples are used for p_T values exceeding 50 GeV. All three $W\gamma$ samples are generated at leading order using MadGraph [114], and a constant NNLO k-factor [127] of 1.34 [128, 129] is applied to account for higher-order corrections. The mixing procedure is designed to obtain a smooth photon p_T distribution, as depicted in Figure 4.10. For the $Z\gamma$ process, an inclusive NLO sample with $p_T > 10$ GeV is used. Given that the $Z\gamma$ sample includes a matrix-element-level cut of $M_{ll} > 30$ GeV, it is complemented with a portion of the Drell-Yan samples to incorporate events with $M_{ll} < 30$ GeV. Finally, all these simulated samples are normalized to the luminosity of collision data and combined to create the $V\gamma$ template.

The choice of using the $\Delta\phi(l, p_T^{miss})$ distribution for the template fit is motivated by the distinct shape of angular distance between the signal lepton and p_T^{miss} between the $V\gamma$ process and misidentified lepton background. In cases of fake lepton events, p_T^{miss} is typically the result of mismeasured objects and aligns with the lepton. Conversely, in $W\gamma$ events, genuine p_T^{miss} arises due to the presence of a neutrino, resulting in a different $\Delta\phi(l, p_T^{miss})$ shape. The fitting of the two $\Delta\phi(l, p_T^{miss})$ templates to the data distributions allows for the simultaneous determination of the normalization factors for both the $V\gamma$ and fake lepton backgrounds. Template fitting is conducted in the CR, defined by 40 GeV $< p_T^{miss} <$ 70 GeV. The application of a 40 GeV p_T^{miss} cutoff enables the selection of a control sample

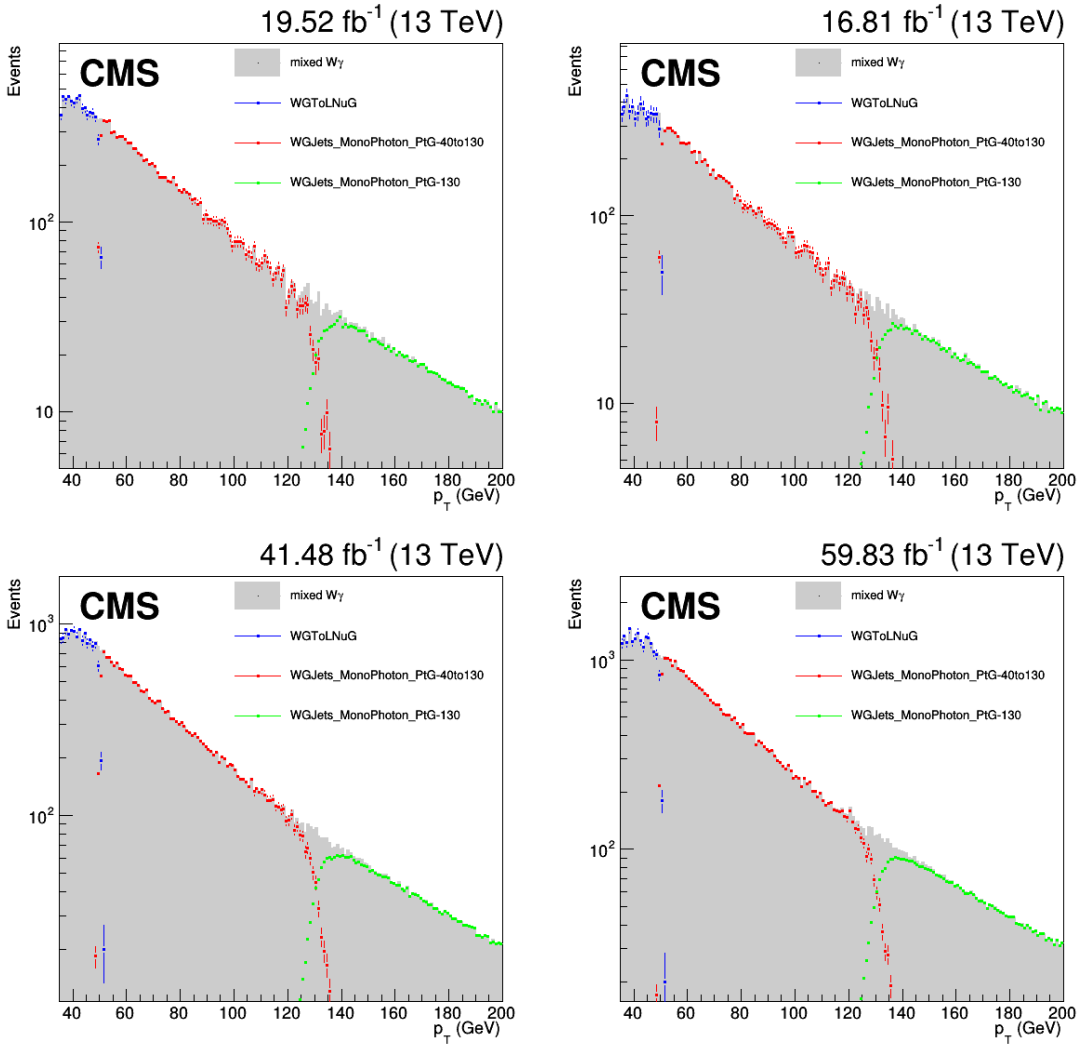

Figure 4.10: The Wγ sample is generated by combining the inclusive `WGToLNuG` sample with two p_T-binned samples: `WGJets_MonoPhoton_PtG-40to130` and `WGJets_MonoPhoton_PtG-130`. The former is truncated at 50 GeV, and the high-statistics p_T-binned samples are utilized for p_T above 50 GeV. Photon p_T distributions in individual $W\gamma$ samples for different p_T ranges are presented, with blue, red, and green points indicating specific samples. The combination of these distributions is represented by the filled histogram for the years 2016 pre-VFP era (upper left), 2016 post-VFP era (upper right), 2017 (lower left), and 2018 (lower right) [13].

primarily composed of $W\gamma$ events. The fitting target of this template fit corresponds to the $\Delta\phi(l, p_T^{miss})$ shape of the data in the CR, after subtracting the contributions from fake photons and rare electroweak backgrounds. This involves utilizing two templates, one derived from the $V\gamma$ sample and the other from the fake lepton samples, and employing the RooFit [135] package for the fit. After determining the fraction of $V\gamma$ events in the CR, the scale factor for the $V\gamma$ sample can be computed as:

$$a_{V\gamma} = \frac{N_{con} \times f_{V\gamma}}{N_{V\gamma}}, \tag{4.2}$$

where N_{con} represents the total count of events in the control sample, $f_{V\gamma}$ is the fraction of $V\gamma$ events obtained from the template fit, and $N_{V\gamma}$ denotes the count of events in the $V\gamma$ template. The remaining events in the control sample, after the removal of $V\gamma$ events, represent the contribution of fake leptons. To study the p_T dependence of the $V\gamma$ scale factors, the template fit is conducted within four lepton p_T bins: (25-50, 50-70, 70-100, $>$=100) GeV. Since no significant dependence on p_T is observed, and due to limited statistics at high p_T values, a template fit is carried out across the entire p_T range, leading to the use of a global $V\gamma$ scale factor.

The main systematic uncertainties for this background estimation arise from the shapes of the fitting target and the data-to-simulation scale factors applied to the Vγ samples. To assess these uncertainties, 1000 iterations of a toy MC fit were performed, revealing a 20% systematic uncertainty in the scale factor.

4.4.5 Rare electroweak backgrounds

The rare electroweak backgrounds, including $t\bar{t}\gamma$, $WW\gamma$, and $WZ\gamma$ standard model processes, are evaluated using NLO MadGraph [114] simulated samples listed in Section 4.2.

Systematic uncertainties

Systematic uncertainties for fake photon backgrounds, as explained in Section 4.4.1 and 4.4.2, are determined through toy MC methods. Similar techniques are applied to assess uncertainties in scale factors for fake lepton and $V\gamma$ backgrounds (Section 4.4.4). Uncertainties in the $V\gamma$ scales, such as cross sections, luminosity, trigger, and object identification efficiencies, are absorbed into the scale factors. For simulation-based backgrounds, uncertainties can arise from cross-sections, luminosity, and jet energy measurements.

4.5 Results

Different standard model backgrounds are estimated in a control region defined by $p_T^{miss} < 70$ GeV, and then the estimates are validated. Figures 4.11, and 4.12 display the comparison between data and estimated background in this control region, revealing a noticeable inconsistency and a clear trend in the data-to-estimated background ratio.

The $M_T(l, p_T^{miss}) < 100$ GeV region is primarily dominated by background events. Studies with TChiWG and T5WG samples reveal that this region has negligible signal contamination. Therefore, the $M_T < 100$ GeV region is used as a validation region for assessing the background prediction.

AN bin	p_T^{miss} $\{120-200, 200-400, >400\}$ $\times HT\{<100, 100-400, >400\}$ $\times$ photon p_T $\{35<200, >200\}$
Plan 1 (9 bins)	p_T^{miss} $\{120-200, 200-400, >400\}$ $\times HT\{<100, 100-400, >400\}$
Plan 2 (18 bins)	p_T^{miss} $\{120-200, 200-400, >400\}$ $\times HT\{<100, 100-400, >400\}$ $\times$ photon p_T $\{35<100, >100\}$
Plan 3 (11 bins)	p_T^{miss} $\{120-200, 200-400, 400-600\}$ $\times HT\{<100, 100-400, >400\}$ + p_T^{miss} $\{>600\}$ $\times HT\{<400, >400\}$
Plan 4 (10 bins)	p_T^{miss} $\{120-200, 200-400, 400-600\}$ $\times HT\{<100, 100-400, >400\}$ + p_T^{miss} $\{>600\}$

Table 4.8: Description of different binning plans. Here, the AN bin corresponds to the binning utilized in a similar analysis previously conducted by CMS. Plans 1, 2, 3, and 4 represent various binning schemes that were evaluated for their impact on the sensitivity of the T5WG model.

This analysis is ongoing with a focus on achieving improved consistency between data and predicted backgrounds in both the control region and validation region. The high p_T^{miss} SR remains blinded until all background estimation procedures are established, ensuring

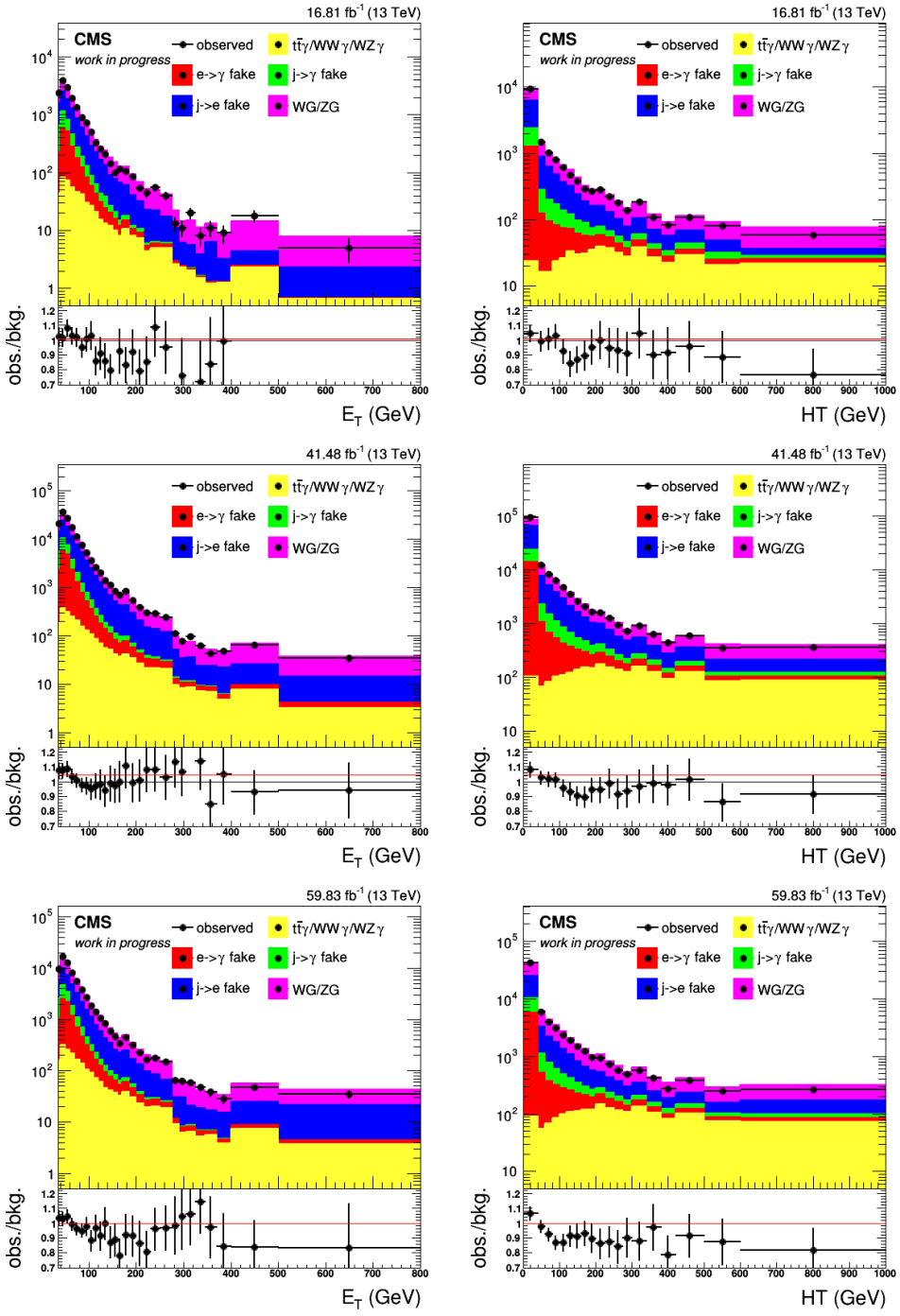

Figure 4.11: Distributions of p_T^{γ} (left plots) and HT (right plots) in data (black points) along with estimated SM predictions (stacked histograms) are shown for the eγ channel. Distributions include events in the $p_T^{miss} < 70$ GeV control region for the years 2016 post-VFP era (upper plots), 2017 (middle plots), and 2018 (lower plots). The vertical bars on the points represent the statistical uncertainty in the data, and the horizontal bars indicate the bin widths. The lower panels display the ratio of the data to the total background prediction [13].

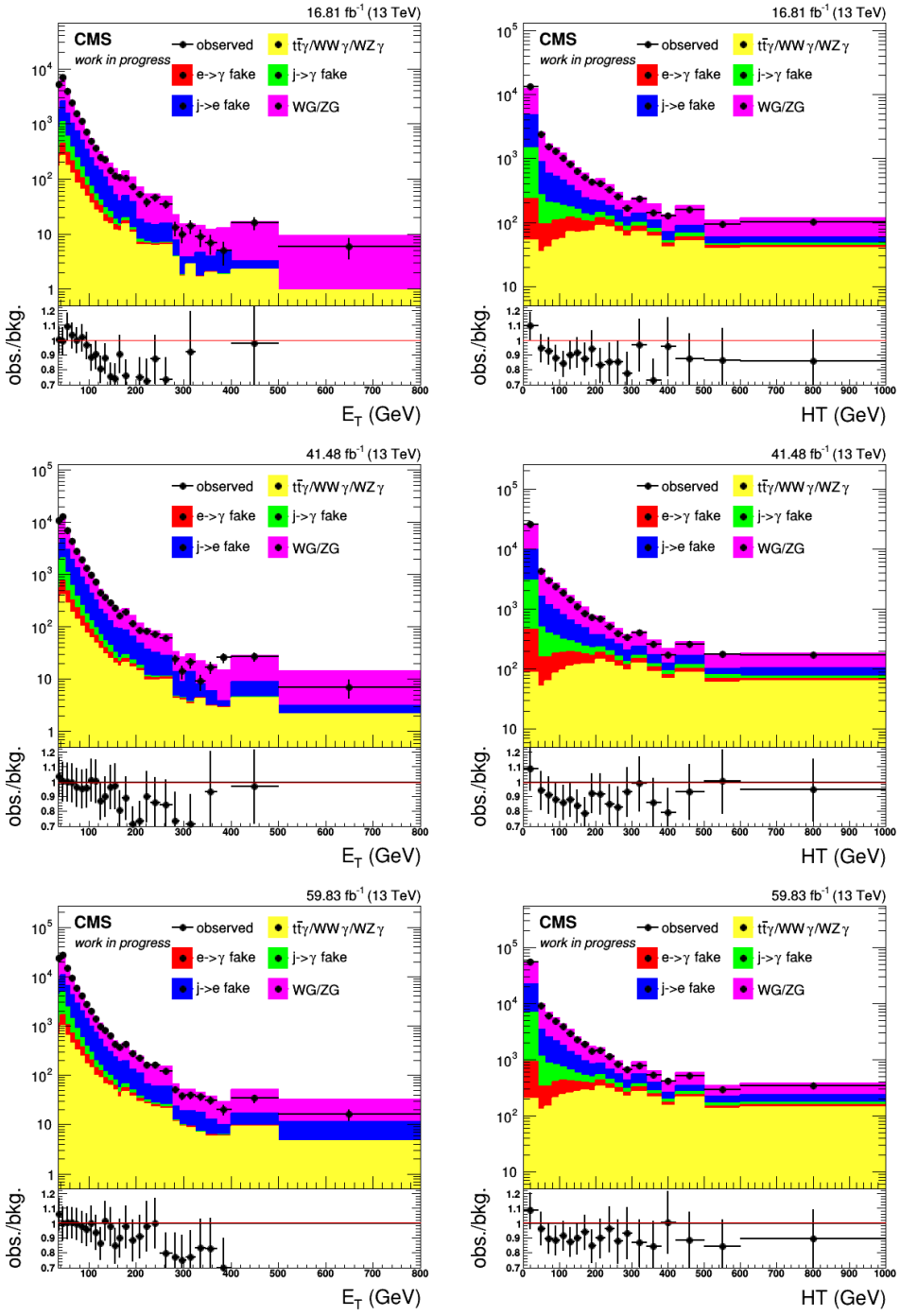

Figure 4.12: Distributions of p_T^{γ} (left plots) and HT (right plots) in data (black points) along with estimated SM predictions (stacked histograms) are shown for the μγ channel. All distributions include events in the $p_T^{miss} < 70$ GeV control region for the years 2016 post-VFP era (upper plots), 2017 (middle plots), and 2018 (lower plots). The vertical bars on the points represent the statistical uncertainty in the data, and the horizontal bars indicate the bin widths. The lower panels display the ratio of the data to the total background prediction [13].

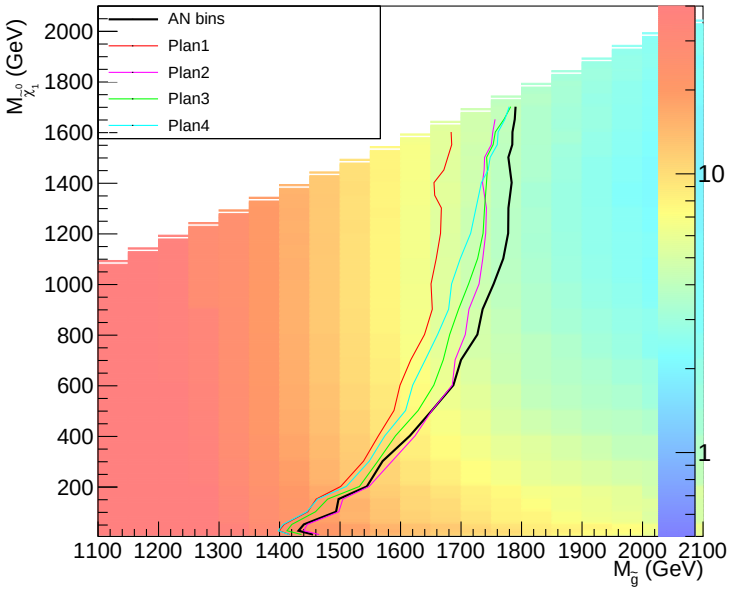

Figure 4.13: The binning in the signal region is optimized based on the variables p_T^{miss}, HT, and photon p_T. Different combinations of binning are considered, as tabulated in Table 4.8. Here, "AN bin" corresponds to the binning utilized in a similar analysis previously conducted by CMS [14]. "Plan1", "Plan2", "Plan3", and "Plan4" represent various binning schemes that were checked for their impact on the sensitivity of the T5WG model. It is observed that the previously used binning ("AN bin") is the most favorable choice, demonstrating the greatest sensitivity for our analysis.

better data and SM background consistency. The SR is defined as $p_T^{miss} > 120$ GeV and $M_T(l, p_T^{miss}) > 100$ GeV. To enhance sensitivity to SUSY signals, the SR is subdivided into bins based on p_T^{miss}, HT, and photon p_T, with binning optimized using T5WG expected limits, as illustrated in Figure 4.13. Each of the $e\gamma$ and $\mu\gamma$ channels utilizes 18 bins, defined as follows: (120 GeV $< p_T^{miss} <$ 200 GeV, 200 GeV $< p_T^{miss} <$ 400 GeV, $p_T^{miss} >$ 400 GeV) $\times$ (0 <HT< 100 GeV, 100 GeV $<$ HT $<$ 400 GeV, HT> 400 GeV) $\times$ (35 GeV $<$ photon $p_T <$ 200 GeV, photon $p_T >$ 200 GeV).

Furthermore, an improvement in expected sensitivity has been observed compared to the previous CMS analysis [14], which solely utilized 2016 data. Specifically, for the T5WG model, the expected exclusion limit using the full Run 2 dataset is 1.57 TeV. This surpasses

the previously established limit of 1.43 TeV using the 2016 dataset. An improvement of approximately 140 GeV is anticipated for the T5WG model.

Chapter 5

Performance of HCAL local reconstruction algorithms

In Chapters 3 and 4, two analyses focusing on the search for SUSY particles are detailed. The collision data utilized for these analyses depends on the performance of various subdetectors within the CMS. The hadron calorimeter (HCAL) is a crucial component in reconstructing events recorded by the CMS detector. Its primary role involves identifying charged and neutral hadrons, measuring their energies, and assisting in identifying leptons and photons. With its hermetic design covering pseudorapidities up to |η| = 5.2 and fine lateral segmentation, the HCAL greatly contributes to estimating missing transverse momentum (p_T^{miss}), which is a crucial variable in the search for new physics such as SUSY. For instance, the analyses previously described target SUSY signals with jets + p_T^{miss} or 1ℓ+ 1γ + p_T^{miss} in the final state. This chapter discusses the performance of four different algorithms used to estimate the energy deposited in the detector elements of the HCAL barrel (HB) and HCAL endcap (HE) during Run 2 of the LHC.

5.1 HB and HE calorimeters

The HB and HE consist of sampling calorimeters employing alternating layers of brass absorbers and plastic scintillator tiles as the active material. The HB region extends from $0 < |\eta| < 1.3$ and extends radially between r = 1.806 and 2.950 m, while the HE has a coverage $1.3 < |\eta| < 3.0$. The HB is a cylindrical structure built by connecting 36 calorimeter wedges covering the full 2π azimuth (ϕ). Each of the wedges is made up of alternating copper alloy absorber plates and plastic scintillators. Two such half wedges

provide the full coverage of HB.

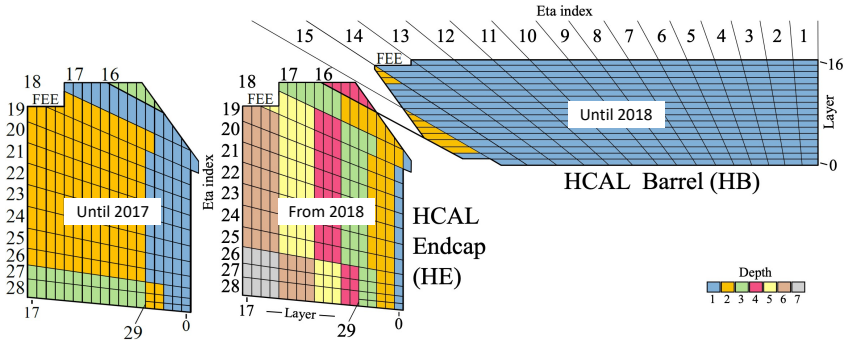

Figure 5.1: A sectional representation of the HB-HE in the r-z plane is displayed. Modules are numbered from 1 to 29 in the η direction, and they are referred to as iη. In the ϕ plane, referred to as iϕ, the range extends from 1 to 72. Different colors are used to represent the depth segments. The depth has been increased prior to the 2018 data collection. The position of the front-end electronics denoted as "FEE", is also indicated [15].

The materials and structure of the endcap are very similar to the barrel system. There are two HE calorimeters on either side of the HB, each of which is an 18-sided polyhedron that encloses one end of the barrel. The HE is constructed with plates separated by staggered spacers, perpendicular to the beam axis. It comprises 19 absorbing layers made of 8 cm wide brass, totaling approximately 10 interaction lengths. HB and HE together cover a length of 7 m along the z direction. Figure 5.1 displays a cross-sectional representation of the HB and HE in the r-z plane. Along the η direction, the modules are spread from 1 to 29 as labeled. These are referred to as iη. In the r-ϕ plane, the modules range from 1 to 72, which are referred to as iϕ. Similarly, the depth segments are shown in different colored shades. The number of depth has been increased before the 2018 data-taking.

During Run 1 from 2010 to 2012, hybrid photodiodes (HPDs) were used as photodetectors in the HB and HE. These were chosen for their tolerance to magnetic fields, high gain, and linear response across a wide dynamic range. However, they suffered from high-amplitude anomalous noise due to electrical discharges and ion feedback. As part of the

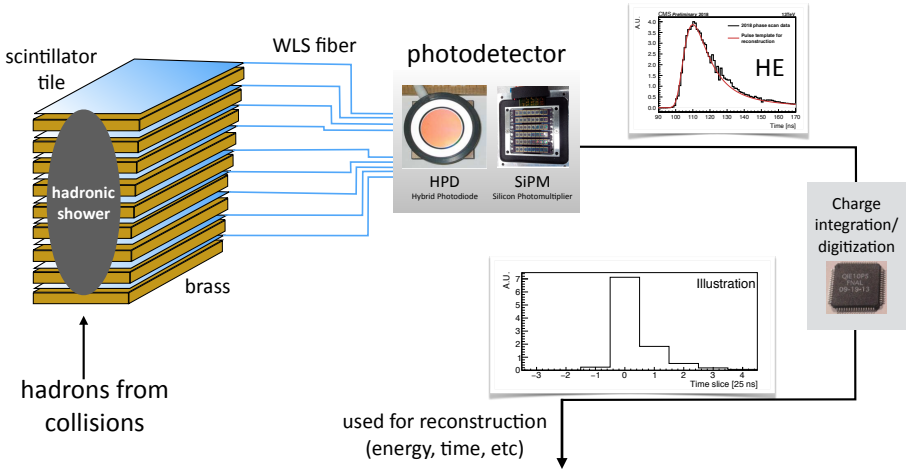

Figure 5.2: HCal readout chain [16].

HCAL Phase-1 upgrade in 2017-2018, the HPDs in the HE were replaced with silicon photomultipliers (SiPMs) [137, 138]. SiPMs offer high gain (between 10^4 and 10^6), good quantum efficiency (20-40%), and function well in high magnetic fields. Their higher gain, smaller size, and lower power consumption allowed for finer depth segmentation. This segmentation improved shower energy resolution, mitigated radiation damage effects, and aided in identifying in-time pileup, where additional interactions within the same bunch crossing deposit energy in shallower depths. The HB underwent a similar upgrade after 2018.

When the energetic hadrons enter the HCAL, a hadronic shower is developed. The scintillation light is produced from the energy deposited by the hadronic shower and propagated through wavelength-shifting (WLS) fibers to the photodetectors and frontend electronics. Here, the optical signal is converted into an analog electric signal for further data processing. The whole HCAL shares a common electronic chain after the photodetectors. The analog signal is digitized by a Charge Integrator and Encoder chip (QIE) which integrates the charge from the photodetector over 25 ns interval, called "time sample" (TS), that corresponds to the LHC bunch spacing. The QIE integrates the charge using an adapted

floating-point concept [139], dividing the input signal into subranges and integrating only a portion of the signal for each subrange. This clever concept has made the uncertainty due to digitization a subdominant factor to the energy resolution. The readout chain is graphically shown in Fig. 5.2. By this method, the HCAL can have a continuous readout, so there is no memory leakage and pipeline issue in the frontend electronics. Instead, the reading from the QIE is transmitted to the backend electronics for each TS. This technique is very useful since all the data processing can be adjusted and new features can be added in the firmware of the backend electronics without introducing any risky modifications in the frontend part.

5.2 Local reconstruction algorithms

The main purpose of the HCAL local reconstruction algorithms is to measure the energy of individual readout channels. From the QIE measurements of eight TSs, an algorithm is run to extract the contribution from the collision of interest. A challenge is that, as shown in Fig. 5.3, the width of the pulses obtained from the scintillator tile through WLS fiber is wider than one TS. So, there is a leakage of the in-time pulse to the next TSs. The fraction of pulses in the following TSs is approximately 30%.

For Run1, where the bunch spacing was 50 ns, a simple sum of charges in the SOI and SOI+1 was used thanks to the absence of out-of-time pileup in the previous TS (Method0). In Run2, however, the bunch spacing became 25 ns rendering Method0 unsuitable due to a large spill-over from the previous bunch crossing. New algorithms (Method2, Method3, and MAHI) based on multiple pulse templates were developed and implemented in both online and offline reconstructions. An algorithm known as Method1 was developed with simplifications such as ignoring time delays, which did not perform well enough for practical use. Table 5.1 lists the algorithms used for online and offline reconstructions in each Run2 year.

Table 5.1: HCAL local reconstruction algorithms used in Run2 for online and offline processing.

Year	Online	Offline
2016	Method3	Method2
2017	Method3	Method2
2018	MAHI	MAHI

5.2.1 Pulse shape of HB and HE

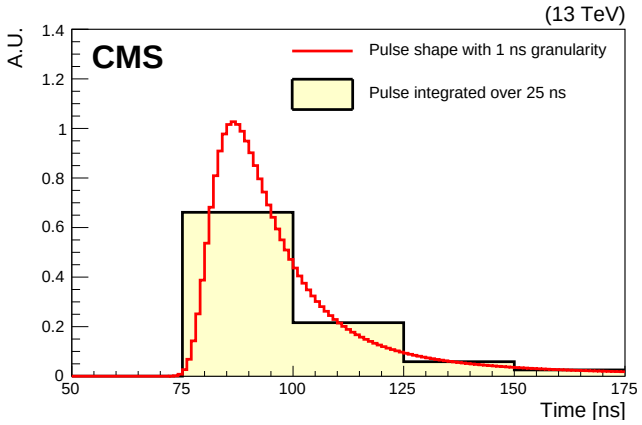

Figure 5.3: The average pulse shape for large energy deposits in the HE is displayed. The reconstruction algorithms employ a pulse shape represented by the solid red line with a granularity of 1 ns. The yellow-filled histogram is derived from the red shape by integrating over each 25 ns TS. The SOI corresponds to the TS from 75 to 100 ns [15].

The shapes of pulses in HB and HE are shaped by factors such as the hadronic shower, the scintillation process within the tiles, optical transmission, wavelength-shifting characteristics, photosensors, and the QIE chips. The hadronic shower development is just intrinsically stochastic, so even with an ideal detector, significant variations in the output pulse shapes would still occur. Also, due to detector geometry, *e.g.*, the difference in time of flight, and cable lengths, the arrival times are varied. The difference is mitigated by adjusting the setting channel by channel such that all channels have uniform arrival time ($\Delta t < 1\,\text{ns}$).

The integration by the QIE chips introduces an amplitude-dependent delay of the pulse arrival time and was studied in test beam data. This effect is parametrized as a function of

the Charge Q through the following formula

$$\Delta_{\text{slew}}[\text{ns}] = 11.98 - 1.56 \log Q[\text{fC}]. \tag{5.1}$$

This is a post-hoc approximation to the real amplifier slew rate, which depends on the instantaneous input current, which cannot be directly reconstructed but is approximated using the total pulse amplitude for the pulse assigned to that TS. The pulse shapes of HPD and SiPM are quite different, and most notably, the SiPM pulse shapes are minimally affected by time slew due to a much higher input operating point for the QIE11.

The pulse shape measurement was performed using a test beam or LHC collisions. In order to account for potential pulse shape distortion by pulse time setting, the pulse shape should be known with much more granularity than 25 ns. This was achieved using a differencing method [140], by measuring the fraction of charges in TSs with different arrival times. For the Phase-0 configuration, the average pulse shape was measured with a 300 GeV pion test beam before the LHC collisions [140]. For the Phase-1 configuration, the measurement was performed in situ using isolated bunch collisions. Data were taken with 25 ns pulse time settings where the adjacent settings are 1 ns apart. With the 25 pulse shapes, the differencing method used 2004-2006 test beams [140] to construct the pulse templates with 1 ns granularity. The first measurement was performed in 2017 using the pilot Phase-1 system of one wedge of one side of HE, and the second measurement was done in 2018 using the fully upgraded HE. Figure shows the extracted pulse shape used in the local reconstruction algorithm in 1 ns and 25 ns granularities.

Reconstruction algorithms use templates based on pulse shapes to find the hit energy from QIE measurements. Both pulse shapes and QIE measurements are affected by various systematic sources, so they should be taken into account. In this section, the list of uncertainties as well as how they are derived is discussed.

In QIE, charge is integrated in capacitors and there is a constant flow of leakage of

charge from them (QIE current). Size of this current is measured using data taken in the absence of proton-proton collisions and is constant throughout the data-taking period. As the SiPMs are irradiated, the damage on the sensor results in liberation of thermal electrons (SiPM leakage current). The number of such electrons becomes significant as the integrated luminosity of LHC increases. The average current is $1.2\,\mu$A and $0.9\,\mu$A in 50 fb^{-1} for the SiPMs with each side 3.3 mm and 2.8 mm, respectively. In order to take into account the effects of QIE current and SiPM leakage current, the size of both currents was measured periodically using data samples recorded in an environment where there are no activities in the detector. The sum of QIE current and SiPM leakage current is hereafter referred to as pedestal, whose average value and standard deviation are measured using data taken when pp collisions are absent. Figure 5.4 shows the growth of pedestal in HB and HE (depth $>$ 1) during 2018.

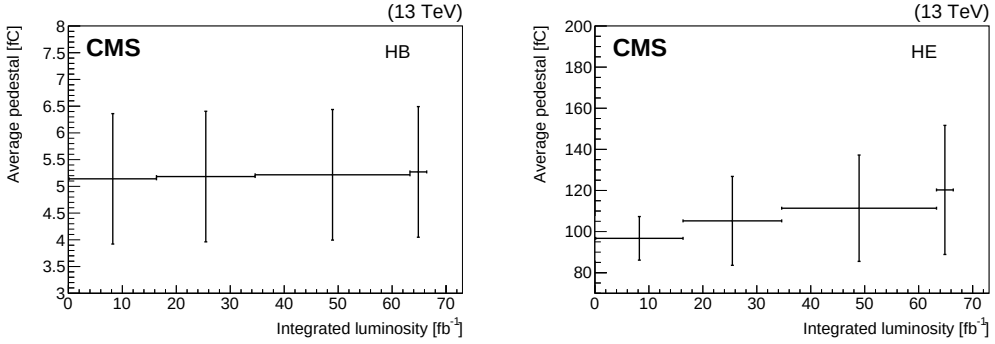

Figure 5.4: The average value of the pedestal increases with time. The evolution of the pedestal with a number of days since the start of 2018 data taking is shown for HB (left plot) and HE when depth $>$ 1 (right plot) [15].

5.2.2 Method0

In Run1 the bunch spacing was 50 ns and the energy of hits was reconstructed by a simple sum of charges in SOI and SOI+1 after the contribution from QIE and SiPM leakage currents is subtracted. Since about 10% of the pulse is not contained within these two TSs, a

correction factor is applied to account for the tail extending beyond them. This procedure is called Method0 (M0).

In Run2, M0 was expected to yield a poor energy resolution as it does not remove the pulses from the previous bunch crossings that may overlap with the pulse from the SOI. Therefore, new algorithms that extract only the energy for SOI were developed.

5.2.3 Method2

Method2 (M2) was developed to provide an accurate energy reconstruction for the SOI pulse in a 25 ns bunch spacing environment. This is achieved by fitting pulse shape templates to the QIE measurements. The pulse templates were derived from the methods described in Section 5.2.1, and the time slew effect is taken into account while constructing the templates. To optimize CPU time, the algorithm runs only when the combined charges in SOI and SOI+1, as well as the total pedestal-subtracted charges, are greater than zero.

M2 extracts the energy and pulse arrival time by minimizing a χ^2 defined as

$$\chi^2 = \sum_{i=0}^{7} \frac{(\mathrm{TS}_i - A_i)^2}{\sigma_{p,i}^2} + \sum_{j=0}^{2} \frac{(t_j - \langle \mathrm{t} \rangle)^2}{\sigma_t^2} + \frac{(\mathrm{ped} - \langle \mathrm{ped} \rangle)^2}{\sigma_{\mathrm{ped}}^2}. \tag{5.2}$$

The free parameters are the arrival time (t_j) of the pulse for the j^{th} TS and amplitude (A_i) of up to three pulse shape templates and the floating baseline component (ped). The TS_i is the QIE measurement in the i^{th} TS, A_i is the amplitude of the fitted pulse shape in that TS and σ_p is the uncertainty due to QIE and SiPM leakage currents, the granularity of the ADC, and the photostatistics. The $\langle \mathrm{t} \rangle$ is the expected pulse time and σ_t is the variation in pulse arrival time. The $\langle \mathrm{ped} \rangle$ is the expected value of the baseline component and σ_{ped} is its variation. The χ^2 is minimized using Minuit2 [141].

In 2016 and 2017 when M2 was used as the main local reconstruction method, it could fit up to three pulse templates for SOI-1, SOI, and SOI+1. As the first step, the fit is performed with the template for the SOI. Since the contribution from the out-of-time collisions for

high-energy hits is not significant, fitting with one template is sufficient. If the χ^2 from the first step is larger than 15 and the extracted energy is less than 100 fC (roughly 20–50 GeV depending on η), the fit is performed again with three pulse templates.

5.2.4 Method3

Due to the long computation time to run the minimization, M2 did not meet the timing requirement of the High-Level Trigger (online) system. Thus, a new algorithm, namely Method3 (M3) was developed which is computationally much faster as well as efficient in rejecting the out-of-time pulses. It assumes a fixed pulse arrival time after the time-slew correction. This simplifies the fitting to solving the linear equations.

M3 also uses three pulses, but instead of using the full 8-time samples, it uses only the QIE measurements and the portion of templates in SOI-1, SOI, and SOI+1. The main difference compared to M2 is that the pulse amplitudes are obtained not by recursive minimization, but rather by solving the following three linear equations:

$$\begin{bmatrix} \mathrm{TS}_{\mathrm{SOI}-1} \\ \mathrm{TS}_{\mathrm{SOI}} \\ \mathrm{TS}_{\mathrm{SOI}+1} \end{bmatrix} = \begin{bmatrix} f_0 & 0 & 0 \\ f_1 & f_0 & 0 \\ f_2 & f_1 & f_0 \end{bmatrix} \begin{bmatrix} A_{\mathrm{SOI}-1} \\ A_{\mathrm{SOI}} \\ A_{\mathrm{SOI}+1} \end{bmatrix} + \begin{bmatrix} B \\ B \\ B \end{bmatrix} \tag{5.3}$$

where $\mathrm{TS}_{\mathrm{SOI}-1}$, $\mathrm{TS}_{\mathrm{SOI}}$, and $\mathrm{TS}_{\mathrm{SOI}+1}$ are the QIE measurements after pedestal subtraction in SOI-1, SOI, and SOI+1, respectively; f_0, f_1, and f_2 denote the premeasured fractions of the pulse template in +0, +1 and +2 TS, respectively. A_i is the amplitude of the pulse for TS_i. The baseline, B, is the average of $\min(\mathrm{TS}_i, 2.7\ \mathrm{fC})$ for all TSs excluding SOI to SOI+2. A maximum value 2.7 fC that corresponds to about 3σ width of the pedestal fluctuations is imposed in order to avoid bias due to the existence of large early or late pulses.

5.2.5 MAHI

Until 2017, M2 and M3 were used for offline and online reconstructions, respectively. Though M3 uses the same pulse templates as M2, the procedure to extract the in-time energy

is different. This led to inconsistency between the quantities in online and offline reconstructions, in particular, in the variables related to electrons. In order to resolve this issue, a new algorithm, called Minimization At HCAL, Iteratively (MAHI), was developed and deployed for data-taking in 2018. The algorithm uses the same templates and uncertainties as M2, but the minimization is done by the fast Non-Negative Least Square (NNLS) algorithm [142] instead of Minuit2 [141]. The main idea is linearization and marginalization of the pulse arrival time and requiring non-negativity allows us to simplify the problem. This algorithm is used for the legacy processing of the CMS Run2 events. The algorithm has been modified for execution on GPUs in the new processor farm, enabling a significant reduction in processing time for future tasks.

The first step of MAHI is to construct a 8×8 covariance matrix based on two sources, noise ($\tilde{\Sigma}^{\text{noise}}$) and pulse shape ($\tilde{\Sigma}^{\text{pulse}}$). The noise term incorporates the ADC granularity, photostatistics, and fluctuation of the pedestal where the pedestal is estimated from the average of four TSs.These uncertainties are added to the diagonal elements of the matrix. The uncertainties in the pulse shape described in Section 5.2.1 are added to the diagonal and off-diagonal elements. They are constructed by shifting the templates forward and backward by their resolution. The shifted templates are subtracted by the nominal template and the average of differences ($+1\sigma$ and -1σ) is taken. A separate covariance matrix is created for each pulse template, resulting in a total of eight covariance matrices. After $\tilde{\Sigma}^{\text{noise}}$ and $\tilde{\Sigma}^{\text{pulse}}$ are formed, the covariance matrix $\tilde{V}$ is constructed by

$$\tilde{V} = \sum_{i=0}^{7} A_i^2 \tilde{\Sigma}_i^{\text{pulse}} + \tilde{\Sigma}^{\text{noise}} \tag{5.4}$$

where A_i is the amplitude of the pulse for TS_i. The fit is an iterative process. In the beginning, the covariance matrix is initialized by the noise terms. Then, the NNLS algorithm is run to find the pulse amplitudes A_i. Physical pulses should have positive amplitudes, so

A_i's are constrained to be positive. Using the extracted A_i's, the algorithm calculates

$$\chi^2 = \left[\tilde{P}\vec{A} - \vec{d}\right]^T \left[\sum_{i=0}^{7} A_i^2 \tilde{\Sigma}_i^{\text{pulse}} + \tilde{\Sigma}^{\text{noise}}\right] \left[\tilde{P}\vec{A} - \vec{d}\right] \tag{5.5}$$

where $\tilde{P}$ is the 8×8 matrix that contains pulse templates and $\vec{d}$ is the vector that contains QIE measurements after pedestal subtraction. Following the initial iteration, the covariance matrix is revised based on the optimal values of A_i that minimize the χ^2 value, marking the commencement of the subsequent iteration. If the difference in χ^2 between two iterations is below 10^{-3} or the number of iterations surpasses 500, the iteration process concludes. Typically, the number of iterations is fewer than 10.

5.3 Consistency between online and offline reconstructions of MET in data

One of the motivations behind the development of MAHI was to use the same algorithm in both online and offline reconstructions. The relative change of online Missing Transverse Momentum (MET) with respect to offline MET is compared when MAHI is used for both offline and online reconstructions with when M3 and M2 are used for online and offline reconstruction, respectively. $\mathcal{O}$ (10^5) events in the 2018 data sample were employed as input. In order to select a sample without bias, events selected by the existence of muons are used. Figure 5.5 demonstrates that better online-offline consistency is achieved when MAHI is used for both online and offline reconstruction.

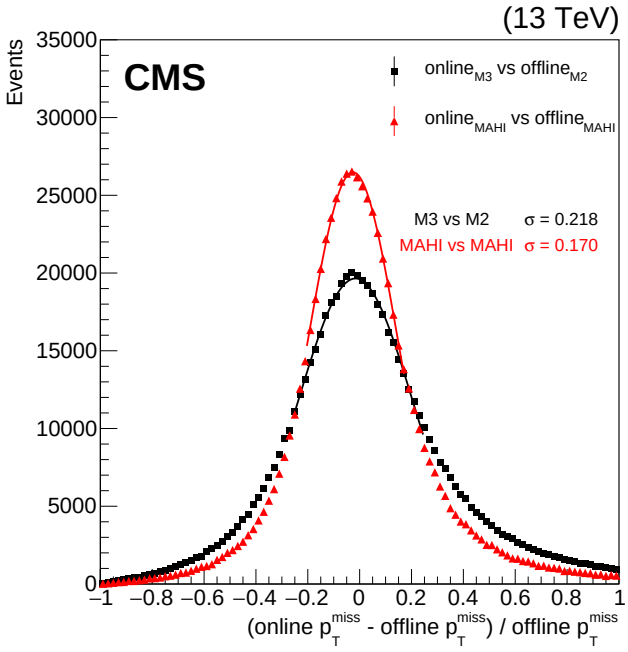

Figure 5.5: Relative change of online MET with respect to offline MET for M3+M2 and MAHI+MAHI [15].

Chapter 6

Summary and Conclusions

The SM of particle physics, while remarkably successful, leaves many fundamental questions unanswered. SUSY has long been considered a leading candidate for physics beyond the SM. SUSY predicts superpartners for each SM particle, potentially explaining open problems and offering dark matter candidates. Despite numerous measurements at the LHC, convincing evidence for BSM theories is still lacking. This thesis comprises three analyses using proton-proton collision data at 13 TeV energy, comprising 137 fb^{-1} integrated luminosity collected by the CMS experiment from 2016 to 2018. Two of these studies specifically focus on investigating the signatures of SUSY. The first analysis, detailed in Chapter 3, focuses on the production of colored SUSY particles, while the subsequent one, extensively discussed in Chapter 4, explores the signature of general gauge-mediated (GGM) SUSY. Despite extensive efforts, the thesis concludes that there is no conclusive evidence supporting SUSY production. As a result, the data were analyzed to establish upper limits on the production cross-section, contributing to the ongoing efforts of the CMS Collaboration to address unresolved questions within the SM. Additionally, the performance of various local reconstruction algorithms employed in the CMS HCAL during Run 2 is discussed in Chapter 5.

The search for SUSY in events involving jets and significant p_T^{miss} final states is motivated by addressing the gauge hierarchy problem and the lack of WIMPs in the SM, which are compelling challenges in theoretical particle physics. This study specifically targets the production of colored SUSY particles like gluinos and squarks, which subsequently decay into jets, and substantial p_T^{miss}. This approach provides orthogonal insights compared

to studies with explicit lepton requirements, enriching the independent set of CMS SUSY searches. This study focused on events containing multiple jets and substantial p_T^{miss}. The primary sources of background were events involving neutrino production or jet mismeasurement. To evaluate the SM backgrounds, control regions in the data were used, supplemented by MC simulations. The results revealed consistency between the observed event yields and the expected background events from SM processes, signifying no significant indication of SUSY. These outcomes were interpreted within simplified models for gluino and squark pair production. The analysis excluded gluinos with masses ranging from 2000 to 2310 GeV at a 95% CL, depending on the specific signal model. Similarly, direct squark production scenarios were examined, revealing exclusion limits up to 1190 GeV for top squarks and 1630 GeV for light-flavored squarks. These findings extended prior mass limits by approximately 200 GeV or more, deepening our understanding of supersymmetric particles.

This thesis explores SUSY search with models utilizing the GGM SUSY mechanism, assuming the conservation of R parity. This analysis is performed using events containing a photon, at least one lepton (electron or muon), along with significant p_T^{miss}. The presence of an extra lepton in events increases the detection sensitivity for the EW production of SUSY particles. Therefore, signatures involving both leptons and photons play a vital role in the SUSY search efforts at the LHC. SM backgrounds are evaluated using control samples and simulation samples are used for electroweak background processes. The techniques for estimating the SM backgrounds in control regions and extrapolating them to the signal region are discussed. This ongoing analysis aims to improve the agreement between observed data and predicted backgrounds in the control regions, which is crucial before proceeding to the signal region where a significant number of supersymmetric signal events are anticipated. In the signal region, the expectation is to either detect SUSY signatures or obtain a null result, which would further constrain SUSY particle masses, potentially surpassing limits

set by previous analyses [96].

The HCAL is a vital component of the CMS detector, identifying and measuring energies of charged and neutral hadrons, aiding in lepton and photon identification, and crucially estimating p_T^{miss}. Starting from August 2015, the LHC began proton-proton collisions with bunch-crossing intervals as short as 25 ns. However, the pulse shapes recorded in HCAL typically extend beyond 25 ns, with 85-90% of the integrated energy concentrated within a 50 ns window. This leads to challenges, such as OOTPU, where energy deposited in HCAL from nearby collisions interferes with accurate energy estimation. To address this, four different local reconstruction algorithms were employed during Run 2 of the LHC. In this thesis, these four local reconstruction algorithms are introduced and their performance is evaluated, considering their ability to suppress OOTPU versus computational complexity, crucial for their deployment in HLT guiding both online and offline reconstructions. Method0 is effective with 50 ns bunch-crossing spacing, but for 25 ns spacing, a pulse-shape fitting algorithm is necessary. Method 2 performs well in high OOUTPU conditions but is too slow for HLT. Although Method 3 could meet online reconstruction time constraints, using different algorithms leads to algorithm mismatch issues. The "Minimization at HCAL, Iteratively" pulse-shape fitting algorithm suppresses OOTPU, offers good energy resolution, and operates quickly in HLT. Consequently, it became the preferred HCAL local energy reconstruction method by the end of Run 2.

The ongoing operations of the LHC hold the promise of unraveling the mysteries of SUSY and pushing the boundaries of particle physics. Despite this thesis not yielding results beyond the SM, the continuous data collection at the LHC creates pathways for future discoveries. The current phase of SUSY searches faces uncertainty, possibly requiring higher-energy collisions. With Run-3 of the LHC delivering significantly more data, particle physics enters an exciting phase, marked by the exploration of alternative final states and previously unexplored scenarios in SUSY searches. The upcoming transition to the

High-Luminosity LHC holds promise, but reaching higher mass scales demands higher collision energies. Advanced techniques like neural networks may boost analysis sensitivity. Collaborative efforts coupled with measurements deviating from the SM, provide crucial constraints for new physics theories. As we step into LHC Run 3 and the subsequent High-Luminosity era, the field anticipates fresh opportunities, new data will unlock doors to further exploration of physics beyond the SM.

References

[1] Pauline Gagnon. The standard model: a beautiful but flawed theory. http://www.quantumdiaries.org/2014/03/14/the-standard-model-a-beautiful-but-flawed-theory, 2014.

[2] Wikimedia. Mexican hat potential polar with details. https://commons.wikimedia.org/wiki.

[3] S. P. Martin. A supersymmetry primer. *Adv. Ser. Direct. High Energy Phys.18*, 1:1–98, 1998. https://arxiv.org/abs/hep-ph/9709356.

[4] Max Maerker. Search for heavy neutral higgs bosons decaying into the fully hadronic di-tau final state with atlas. https://cds.cern.ch/record/2800824/, 2022.

[5] LHC SUSY Cross Section Working Group. Lhc susy cross section. https://twiki.cern.ch/twiki/bin/view/LHCPhysics/SUSYCrossSections.

[6] CMS Collaboration. The cern accelerator complex. https://cds.cern.ch/record/1260465, 2010.

[7] CMS Collaboration. Cms luminosity - public results. https://twiki.cern.ch/twiki/bin/view/CMSPublic/LumiPublicResults.

[8] Tai Sakuma. Cutaway diagrams of cms detector. https://cds.cern.ch/record/2665537, 2019.

[9] D. Barney. Cms detector slice. https://cds.cern.ch/record/2120661, 2016.

[10] Willem Verbeke. Searches for undiscovered processes using the multilepton final state in proton-proton collisions at cms. https://cds.cern.ch/record/2811477, 2022.

[11] CMS Collaboration. Search for supersymmetry in proton-proton collisions at 13 tev in final states with jets and missing transverse momentum. *JHEP*, 10:244, 2019. https://doi.org/10.48550/arXiv.1908.04722.

[12] CMS Collaboration. Search for supersymmetry in proton-proton collisions at 13 tev in final states with missing transverse momentum and jets. https://gitlab.cern.ch/tdr/notes/AN-18-271, 2019.

[13] CMS Collaboration. Search for supersymmetry in proton-proton collisions at 13 tev in final states with a photon, lepton, and missing transverse energy. https://gitlab.cern.ch/tdr/notes/AN-21-007, 2021.

[14] The CMS Collaboration, A.M. Sirunyan, and A. et al. Tumasyan. Search for supersymmetry in events with a photon, a lepton, and missing transverse momentum in proton-proton collisions at tev. *J. High Energ. Phys.*, 2019:154, 2019. https://doi.org/10.1007/JHEP01(2019)154.

[15] CMS Collaboration. Performance of the local reconstruction algorithms for the cms hadron calorimeter with run 2 data. https://doi.org/10.48550/arXiv.2306.10355.

[16] CMS Collaboration. Performance of hcal local reconstruction algorithms in run2. https://gitlab.cern.ch/tdr/notes/AN-21-010, 2021.

[17] M. Tanabashi et al. Review of particle physics. *Physical Review D*, 98:030001, 2018. https://doi.org/10.1103/PhysRevD.98.030001.

[18] P. Higgs. Broken symmetries, massless particles and gauge fields. *Physics Letters*, 12:132, 1964. https://doi.org/10.1016/0031-9163(64)91136-9.

[19] S. Glashow. Partial-symmetries of weak interactions. *Nuclear Physics*, 22:579, 1961. https://doi.org/10.1016/0029-5582(61)90469-2.

[20] S. Weinberg. A model of leptons. *Physical Review Letters*, 19:1264, 1967. https://doi.org/10.1103/PhysRevLett.19.1264.

[21] M. Y. Han and Y. Nambu. Three-triplet model with double SU(3) symmetry. *Phys. Rev.*, 139:B1006, 1965. https://doi.org/10.1103/PhysRev.139.B1006.

[22] Abdus Salam and John Clive Ward. Weak and electromagnetic interactions. *Nuovo Cim.*, 11:568–577, 1959. https://link.springer.com/article/10.1007/BF02726525.

[23] Lyndon Evans and Philip Bryant. Lhc machine. *Journal of Instrumentation*, 3(08):S08001, aug 2008. https://dx.doi.org/10.1088/1748-0221/3/08/S08001.

[24] R. Voss and A. Breskin, editors. *The CERN Large Hadron Collider, Accelerator and Experiments*. CERN, 2009.

[25] J. Wess and B. Zumino. Supergauge invariant extension of quantum electrodynamics. *Nucl. Phys. B*, 78:1, 1974. https://www.sciencedirect.com/science/article/abs/pii/0550321374901685.

[26] A. Salam and J. Strathdee. Super-symmetry and non-abelian gauges. *Physics Letters B*, 51(4):353–355, 1974. http://www.sciencedirect.com/science/article/pii/0370269374902263.

[27] S. Ferrara and B. Zumino. Supergauge invariant yang-mills theories. *Nucl. Phys. B*, 79:413, 1974. https://www.sciencedirect.com/science/article/abs/pii/0550321374902515.

[28] The CMS Collaboration. Observation of a new boson at a mass of 125 gev with the cms experiment at the lhc. *Physics Letters B*, 716(1):30–61, September 2012. http://dx.doi.org/10.1016/j.physletb.2012.08.021.

[29] The ATLAS Collaboration. Observation of a new particle in the search for the standard model higgs boson with the atlas detector at the lhc. *Physics Letters B*, 716(1):1–29, September 2012. http://dx.doi.org/10.1016/j.physletb.2012.08.020.

[30] David Griffiths. *Introduction to Elementary Particles*. Wiley-VCH, 2009.

[31] Raymond Davis, Don S. Harmer, and Kenneth C. Hoffman. Search for neutrinos from the sun. *Phys. Rev. Lett.*, 20(21):1205–1209, 1968. {https://link.aps.org/doi/10.1103/PhysRevLett.20.1205}.

[32] Y. Fukuda and et al. (Super-Kamiokande Collaboration). Evidence for oscillation of atmospheric neutrinos. *Phys. Rev. Lett.*, 81(8):1562–1567, 1998. https://link.aps.org/doi/10.1103/PhysRevLett.81.1562.

[33] Y. Abe and et al. (Double Chooz Collaboration). Indication of reactor ν_e disappearance in the double chooz experiment. *Phys. Rev. Lett.*, 108(13):131801, 2012. https://link.aps.org/doi/10.1103/PhysRevLett.108.131801.

[34] P. A. Zyla and et al. Review of particle physics. *PTEP*, 2020(8):083C01, 2020.

[35] J. Schwinger. On quantum-electrodynamics and the magnetic moment of the electron. *Phys. Rev.*, 73:416, 1948. https://doi.org/10.1103/PhysRev.73.416.

[36] J. Schwinger. Quantum electrodynamics. i. a covariant formulation. *Phys. Rev.*, 74:1439, 1948. https://doi.org/10.1103/PhysRev.74.1439.

[37] S. Tomonaga. On a relativistically invariant formulation of the quantum theory of wave fields. *Prog. Theor. Phys.*, 1:27, 1946. https://doi.org/10.1143/PTP.1.27.

[38] R. P. Feynman. Space-time approach to quantum electrodynamics. *Phys. Rev.*, 76:769, 1949. https://doi.org/10.1103/PhysRev.76.769.

[39] S. L. Glashow. The renormalizability of vector meson interactions. *Nucl. Phys.*, 10:107, 1959. https://doi.org/10.1016/0029-5582(59)90196-8.

[40] A. Salam and J. C. Ward. Weak and electromagnetic interactions. *Nuovo Cim.*, 11:568, 1959. https://doi.org/10.1007/BF02726525.

[41] Christina Agapopoulou. Research of supersymmetry with the atlas detector and development of the high granularity timing detector. https://cds.cern.ch/record/2742146, 2020.

[42] Michael E. Peskin and Daniel V. Schroeder. *An Introduction to Quantum Field Theory*. Westview Press, Boulder, CO, 1995. https://cds.cern.ch/record/257493.

[43] C. S. Wu and et al. Experimental test of parity conservation in beta decay. *Phys. Rev.*, 105:1413, 1957. https://doi.org/10.1103/PhysRev.105.1413.

[44] G. Arnison and et al. Experimental observation of lepton pairs of invariant mass around 95 gev/c^2 at the cern sps collider. *Physics Letters B*, 126(5):398–410, 1983. http://www.sciencedirect.com/science/article/pii/0370269383901880.

[45] M. Banner and et al. Observation of single isolated electrons of high transverse momentum in events with missing transverse energy at the cern pp collider. *Physics Letters B*, 122(5):476–485, 1983. http://www.sciencedirect.com/science/article/pii/0370269383916052.

[46] F. Englert and R. Brout. Broken symmetry and the mass of gauge vector mesons. *Phys. Rev. Lett.*, 13:321–323, 1964. https://journals.aps.org/prl/abstract/10.1103/PhysRevLett.13.321.

[47] E. Noether. Invariante variationsprobleme. *Nachrichten von der Gesellschaft der Wissenschaften zu Göttingen, Mathematisch-Physikalische Klasse*, 1918:235–257, 1918. http://eudml.org/doc/59024.

[48] Emmy Noether. Invariant variation problems. *Transport Theory and Statistical Physics*, 1(3):186–207, January 1971. http://dx.doi.org/10.1080/00411457108231446.

[49] E. Witten. Dynamical breaking of supersymmetry. *Nucl. Phys. B*, 188:513, 1981.

[50] S. Dimopoulos and H. Georgi. Softly broken supersymmetry and su(5). *Nucl. Phys. B*, 193(1):150–162, 1981.

[51] N. Sakai. Naturalness in supersymmetric guts. *Zeitschrift fuer Physik C Particles and Fields*, 11(2):153–157, 1981.

[52] L. Susskind. The gauge hierarchy problem, technicolor, supersymmetry, and all that. *Physics Reports*, 104(2):181–193, 1984.

[53] TE Gonzalo Velasco. *Model Building and Phenomenology in Grand Unified Theories*. PhD thesis, University Coll. London, 2015.

[54] V. C. Rubin and W. Kent J. Ford. Rotation of the andromeda nebula from a spectroscopic survey of emission regions. *Astrophysical Journal*, 159:379, 1970. https://doi.org/10.1086/150317.

[55] E. Corbelli and P. Salucci. The extended rotation curve and the dark matter halo of m33. *Monthly Notices of the Royal Astronomical Society*, 311(2):441–447, January 2000. http://dx.doi.org/10.1046/j.1365-8711.2000.03075.x.

[56] A. Bosma. *The Distribution and Kinematics of Neutral Hydrogen in Spiral Galaxies of Various Morphological Types*. PhD thesis, Unknown, January 1978.

[57] Planck Collaboration. Planck 2013 results. xvi. cosmological parameters. *Astronomy and Astrophysics*, 571, 2014. https://arxiv.org/abs/1303.5076v3.

[58] D. Clowe, M. Bradač, A. H. Gonzalez, M. Markevitch, S. W. Randall, et al. A direct empirical proof of the existence of dark matter. *The Astrophysical Journal*, 648(2):L109–L113, 2006. https://iopscience.iop.org/article/10.1086/508162.

[59] M. Bradač, S. W. Allen, T. Treu, H. Ebeling, R. Massey, R. G. Morris, A. von der Linden, D. Applegate, et al. Revealing the properties of dark matter in the merging cluster macsj0025.4-1222. *The Astrophysical Journal*, 687(2):959–967, 2008. http://dx.doi.org/10.1086/591246.

[60] AMS Collaboration. Search for anti-helium in cosmic rays. *Phys. Lett. B*, 461:387, 1999. https://arxiv.org/abs/hep-ex/0002048.

[61] Andrei D. Sakharov. Violation of cp invariance, c asymmetry, and baryon asymmetry of the universe. *Soviet Physics Uspekhi*, 34(5):392–393, 1991. https://iopscience.iop.org/article/10.1070/PU1991v034n05ABEH002497.

[62] J. H. Christenson and et al. Evidence for the 2π decay of the k_2^0 meson. *Phys. Rev. Lett.*, 13:138, 1964. https://doi.org/10.1103/PhysRevLett.13.138.

[63] KTeV Collaboration. Observation of direct cp violation in $k_s, k_l \to \pi\pi$ decays. *Phys. Rev. Lett.*, 83:22, 1999. https://doi.org/10.1103/PhysRevLett.83.22.

[64] T. Asaka, S. Blanchet, and M. Shaposhnikov. The νmsm, dark matter and neutrino masses. *Phys. Lett. B*, 631:151, 2005. https://arxiv.org/abs/hep-ph/0503065.

[65] Ian Aitchison. Supersymmetry and the mssm: An elementary introduction, 2005. June.

[66] Gerard Jungman, Marc Kamionkowski, and Kim Griest. Supersymmetric dark matter. *Physics Reports*, 267(5-6):195–373, March 1996. http://dx.doi.org/10.1016/0370-1573(95)00058-5.

[67] Rabindra N. Mohapatra. Supersymmetry and r-parity: An overview. *Phys. Scripta*, 90:088004, 2015. https://arxiv.org/abs/1503.06478.

[68] N. S. P. Meade and D. Shih. General gauge mediation. *Prog. Theor. Phys. Suppl.*, 177:143, 2009. https://arxiv.org/abs/0801.3278.

[69] A. M. P. Grajek and D. Redigolo. Phenomenology of general gauge mediation in light of a 125 gev higgs. *JHEP*, 07:109, 2013. https://doi.org/10.1007/JHEP07(2013)109.

[70] G.F. Giudice and R. Rattazzi. Theories with gauge-mediated supersymmetry breaking. *Physics Reports*, 322(6):419–499, 1999. http://www.sciencedirect.com/science/article/pii/S0370157399000423.

[71] I. Jack and D. R. T. Jones. Nonstandard soft supersymmetry breaking. *Phys. Lett. B*, 457, 1999.

[72] L. Girardello and M. T. Grisaru. Soft breaking of supersymmetry. *Nucl. Phys. B*, 194, 1982.

[73] ATLAS Collaboration. Summary of the atlas experiment's sensitivity to supersymmetry after lhc run 1 — interpreted in the phenomenological mssm. *JHEP*, 10:134, 2015. https://arxiv.org/abs/1508.06608.

[74] Johan Alwall, Philip Schuster, and Natalia Toro. Simplified models for a first characterization of new physics at the lhc. *Phys. Rev. D*, 79:075020, 2009. https://arxiv.org/abs/0810.3921.

[75] Daniele Alves and et al. Simplified models for lhc new physics searches. *J. Phys. G*, 39:105005, 2012. https://arxiv.org/abs/1105.2838.

[76] H. P. Nilles. Supersymmetry, supergravity and particle physics. *Phys. Rep.*, 110:1, 1984.

[77] T. Schoerner-Sadenius, editor. *The Large Hadron Collider: Harvest of Run 1*. Springer International Publishing, 2015.

[78] The cms experiment at the cern lhc. *Journal of Instrumentation*, 3(08):S08004, aug 2008. https://dx.doi.org/10.1088/1748-0221/3/08/S08004.

[79] The atlas experiment at the cern large hadron collider. *Journal of Instrumentation*, 3(08):S08003, aug 2008. https://dx.doi.org/10.1088/1748-0221/3/08/S08003.

[80] The alice experiment at the cern lhc. *Journal of Instrumentation*, 3(08):S08002, aug 2008. https://dx.doi.org/10.1088/1748-0221/3/08/S08002.

[81] The lhcb detector at the lhc. *Journal of Instrumentation*, 3(08):S08005, aug 2008. https://dx.doi.org/10.1088/1748-0221/3/08/S08005.

[82] T. Gleisberg and et al. Event generation with sherpa 1.1. *JHEP*, 02:007, 2009. https://arxiv.org/abs/0811.4622.

[83] Torbjörn Sjöstrand and et al. An introduction to pythia 8.2. *Computer Physics Communications*, 191:159–177, June 2015. http://dx.doi.org/10.1016/j.cpc.2015.01.024.

[84] A. Buckley and et al. General-purpose event generators for lhc physics. *Phys. Rept.*, 504:145, 2011. https://arxiv.org/abs/1101.2599.

[85] K. Eskola and et al. Rapidity dependence of particle production in ultrarelativistic nuclear collisions. *Phys. Lett. B*, 543:208, 2002. https://doi.org/10.1016/S0370-2693(02)02457-7.

[86] ALEPH Collaboration. Performance of the aleph detector at lep. *Nucl. Instrum. Meth. A*, 360:481, 1995. https://doi.org/10.1016/0168-9002(95)00138-7.

[87] CMS Collaboration. Precision measurement of the structure of the cms inner tracking system using nuclear interactions. *JINST*, 13:P10034, 2018. https://arxiv.org/abs/1807.03289.

[88] CMS Collaboration. Performance of the cms muon detector and muon reconstruction with proton-proton collisions at $\sqrt{s} = 13$ tev. *JINST*, 13:P06015, 2018. https://arxiv.org/abs/1804.04528.

[89] GEANT4 Collaboration. GEANT4–a Simulation Toolkit. *Nucl. Instrum. Meth. A*, 506:250, 2003. https://doi.org/10.1016/S0168-9002(03)01368-8.

[90] CMS Collaboration. The cms trigger system. *JINST*, 12:P01020, 2017. https://arxiv.org/abs/1609.02366.

[91] CMS Collaboration. Performance of the cms level-1 trigger in proton-proton collisions at $\sqrt{s} = 13$ tev. *JINST*, 15:P10017, 2020. https://arxiv.org/abs/2006.10165.

[92] Cms software. https://cms-opendata-workshop.github.io/workshop-lesson-cmssw/01-introduction/index.html.

[93] G. Petrucciani, A. Rizzi, and C. Vuosalo. Mini-aod: A new analysis data format for cms. *Journal of Physics: Conference Series*, 664:072052, 2015. https://doi.org/10.1088/1742-6596/664/7/072052.

[94] CMS Collaboration. Measurement of the inelastic proton-proton cross section at $\sqrt{s} = 13$ tev. *JHEP*, 07:161, 2018. https://arxiv.org/abs/1802.02613.

[95] Interpretation of searches for supersymmetry with simplified models. *Phys. Rev. D*, 88:052017, 2013. https://doi.org/10.48550/arXiv.1301.2175.

[96] Albert M Sirunyan et al. Search for supersymmetry in multijet events with missing transverse momentum in proton-proton collisions at 13 tev. *Phys. Rev. D*, 96:032003, 2017. https://doi.org/10.48550/arXiv.1704.07781.

[97] Albert M Sirunyan et al. Searches for physics beyond the standard model with the M_{T2} variable in hadronic final states with and without disappearing tracks in proton-proton collisions at $\sqrt{s} = 13$ TeV. *Eur. Phys. J. C*, 80(1):3, 2020.

[98] Georges Aad et al. Search for new phenomena in pp collisions in final states with tau leptons, b-jets, and missing transverse momentum with the ATLAS detector. *Phys. Rev. D*, 104(11):112005, 2021.

[99] Georges Aad et al. Search for squarks and gluinos in final states with jets and missing transverse momentum using 139 fb^{-1} of $\sqrt{s}$ =13 TeV pp collision data with the ATLAS detector. *JHEP*, 02:143, 2021.

[100] CMS Collaboration. The CMS trigger system. *JINST*, 12:P01020, 2017. https://doi.org/10.1088/1748-0221/12/01/P01020.

[101] CMS Collaboration. Performance of the CMS level-1 trigger in proton-proton collisions at $\sqrt{s} = 13$ tev. *JINST*, 15:P10017, 2020. https://doi.org/10.1088/1748-0221/15/10/P10017.

[102] CMS trigger study page. https://twiki.cern.ch/twiki/bin/view/CMS/TriggerStudies.

[103] CMS trigger naming scheme. https://twiki.cern.ch/twiki/bin/view/CMS/TriggerNames.

[104] CMS trigger naming scheme. https://twiki.cern.ch/twiki/bin/view/CMS/EgHLTRunIISummary.

[105] M. Cacciari, G. P. Salam, and G. Soyez. The anti-k_t jet clustering algorithm. *JHEP*, 04:063, 2008. https://arxiv.org/abs/0802.1189.

[106] CMS Muon POG. Reference muon id, isolation, and trigger efficiencies for 2016 legacy re-reco data. https://twiki.cern.ch/twiki/bin/view/CMS/MuonReferenceEffs2016LegacyRereco, 2018.

[107] CMS Muon POG. Reference muon id, isolation, and trigger efficiencies for 2017 data. https://twiki.cern.ch/twiki/bin/view/CMS/MuonReferenceEffs2017, 2018.

[108] Cms scientific results. https://cms.cern/org/cms-scientific-results.

[109] K. Rehermann and B. Tweedie. Efficient identification of boosted semileptonic top quarks at the lhc. *JHEP*, 03:059, 2011. https://arxiv.org/abs/1007.2221.

[110] CMS E/gamma POG. Cut based electron id for run 2 legacy. https://twiki.cern.ch/twiki/bin/view/CMS/CutBasedElectronIdentificationRun2, 2018.

[111] CMS JetMET POG. Reweighting recipe to emulate level 1 ecal prefiring. https://twiki.cern.ch/twiki/bin/view/CMS/L1ECALPrefiringWeightRecipe, 2018.

[112] CMS B-tag POG. Usage of b/c tag objects for 13 tev data in 2016 and 80x mc. https://twiki.cern.ch/twiki/bin/viewauth/CMS/BtagRecommendation80XReReco, 2018.

[113] CMS B-tag POG. Heavy flavour tagging for 13 tev data in 2017 and 94x mc. https://twiki.cern.ch/twiki/bin/viewauth/CMS/BtagRecommendation94X, 2018.

[114] S. Frixione and B. R. Webber. Matching nlo qcd computations and parton shower simulations. *JHEP*, 06:029, 2002. https://arxiv.org/abs/hep-ph/0204244.

[115] J. Alwall and et al. The automated computation of tree-level and next-to-leading order differential cross sections, and their matching to parton shower simulations. *JHEP*, 07:079, 2014. https://arxiv.org/abs/1405.0301.

[116] D. Guest and et al. Jet flavor classification in high-energy physics with deep neural networks. *Phys. Rev. D*, 94:112002, 2016. https://arxiv.org/abs/1607.08633.

[117] Thomas Junk. Confidence level computation for combining searches with small statistics. *Nucl. Instrum. Meth. A*, 434:435, 1999. https://arxiv.org/abs/hep-ex/9902006.

[118] A. L. Read. Presentation of search results: the cl (s) technique. *J. Phys. G*, 28:2693, 2002. https://doi.org/10.1088/0954-3899/28/10/313.

[119] N. Seiberg P. Meade and D. Shih. General gauge mediation. *Prog. Theor. Phys. Suppl.*, 177:143, 2009.

[120] A. Mariotti P. Grajek and D. Redigolo. Phenomenology of general gauge mediation in light of a 125 gev higgs. *JHEP*, 07:109, 2013.

[121] G. F. Giudice and R. Rattazzi. Gauge-mediated supersymmetry breaking. *Perspectives on Supersymmetry*, page p. 355., World Scientific, Singapore, 1998.

[122] ATLAS Collaboration. Search for photonic signatures of gauge-mediated supersymmetry in 8 tev pp collisions with the atlas detector. *Phys. Rev. D*, 92:072001, 2015. https://arxiv.org/abs/1507.05493.

[123] CMS Collaboration. Search for supersymmetry in events with a photon, a lepton, and missing transverse momentum in $\sqrt{s} = 8$ tev pp collisions. *Physics Letters B*, 757, 2016. https://doi.org/10.1016/j.physletb.2016.03.039.

[124] Ram1123. Cms analysis - hip problem 2016, March 19 2020. https://ram1123.github.io/tools/2020/03/19/CMS-Analysis.html#hip-problem-2016.

[125] Marketa Jansova. Search for the supersymmetric partner of top quark and measurement of deposit properties in the silicon track tracker of the cms experiment at run 2, 2018. https://cds.cern.ch/record/2647308/files/CERN-THESIS-2018-242.pdf.

[126] Rules for dataset names. https://cms-pdmv.gitbook.io/project/mccontact/rules-for-dataset-names.

[127] K-factors. https://web.pa.msu.edu/people/huston/Kfactor/Kfactor.pdf.

[128] Search for dark matter in monophoton final state at 13 tev. CMS AN 2016/078.

[129] G. Bozzi et al. Production of drell-yan lepton pairs in hadron collisions transverse-momentum resummation at next-to-next-to-leading logarithmic accuracy. *Phys. Lett. B*, 696:207–213, 2011. https://doi.org/10.1016/j.physletb.2010.12.024.

[130] CMS shower shape variables. https://twiki.cern.ch/twiki/bin/view/CMSPublic/SWGuideEgammaShowerShape.

[131] CMS Collaboration. Cut based photon identification run2. https://twiki.cern.ch/twiki/bin/viewauth/CMS/CutBasedPhotonIdentificationRun2, 2018.

[132] Electron and photon reconstruction and identification with the cms experiment at the cern lhc. *Journal of Instrumentation*, 16(05):P05014, may 2021. https://dx.doi.org/10.1088/1748-0221/16/05/P05014.

[133] Baseline muon selections for run-ii. https://twiki.cern.ch/twiki/bin/view/CMS/SWGuideMuonIdRun2#Muon_Identification.

[134] Tag and probe method. https://cms-opendata-workshop.github.io/workshop-lesson-tagandprobe/aio/index.html.

[135] Wouter Verkerke and Daniel P. Kirkby. The RooFit toolkit for data modeling. *eConf*, C0303241:MOLT007, 2003. https://arxiv.org/abs/physics/0306116.

[136] CMS work book. https://twiki.cern.ch/twiki/bin/view/CMSPublic/WorkBookPhotonAnalysis.

[137] S. Gundacker and A. Heering. The silicon photomultiplier: Fundamentals and applications of a modern solid-state photon detector. *Phys. Med. Biol.*, 65:17TR01, 2020. https://doi.org/10.1088/1361-6560/ab7b2d.

[138] CMS Collaboration. Technical proposal for the upgrade of the cms detector through 2020. Technical Report CERN-LHCC-2011-006, LHCC-P-004, CERN, 2011.

[139] Tom Zimmerman and J. Hoff. The design of a charge-integrating modified floating-point adc chip. *IEEE Journal of Solid-State Circuits*, 39:895–905, 2004. http://dx.doi.org/10.1109/JSSC.2004.827808.

[140] CMS Collaboration. Performance of CMS hadron calorimeter timing and synchronization using test beam, cosmic ray, and LHC beam data. *Journal of Instrumentation*, 5(03):T03013–T03013, mar 2010. https://doi.org/10.1088%2F1748-0221%2F5%2F03%2Ft03013.

[141] F. James and M. Roos. Minuit: A System for Function Minimization and Analysis of the Parameter Errors and Correlations. *Comput. Phys. Commun.*, 10:343–367, 1975. https://doi.org/10.1016/0010-4655(75)90039-9.

[142] Donghui Chen and Robert J. Plemmons. *Nonnegativity constraints in numerical analysis*, pages 109–139. https://www.worldscientific.com/doi/abs/10.1142/9789812836267_0008.